THEORY BASED DESIGN AND OPTIMIZATION OF MATERIALS FOR SPINTRONICS APPLICATIONS

by

TIANYI XU

WILLIAM. H. BUTLER, COMMITTEE CHAIR
SUBHADRA GUPTA
OLEG. M. MRYASOV
CLAUDIA. K. A. MEWES
TIM MEWES

A DISSERTAION

Submitted in partial fulfillment of the requirements
for the degree of Doctor of Philosophy
in the Department of Physics and Astronomy
in the Graduate School of
The University of Alabama

TUSCALOOSA, ALABAMA

2012

ABSTRACT

The Spintronics industry has developed rapidly in the past decade. Finding the right material is very important for Spintronics applications, which requires good understanding of the physics behind specific phenomena. In this dissertation, we will focus on two types of perpendicular transport phenomena, the current-perpendicular-to-plane giant-magneto-resistance (CPP-GMR) phenomenon and the tunneling phenomenon in the magnetic tunnel junctions.

The Valet-Fert model is a very useful semi-classical approach for understanding the transport and spin-flip process in CPP-GMR. We will present a finite element based implementation for the Valet-Fert model which enables a practical way to calculate the electron transport in real CPP-GMR spin valves. It is very important to find high spin polarized materials for CPP-GMR spin valves. The half-metal, due to its full spin polarization, is of interest. We will propose a rational way to find half-metals based on the gap theorem.

Then we will focus on the high-MR TMR phenomenon. The tunneling theory of electron transport in mesoscopic systems will be covered. Then we will calculate the transport properties of certain junctions with the help of Green's function under the Landauer-Büttiker formalism, also known as the scattering formalism. The damping constant determines the switching rate of a device. We can calculate it using a method based on the Extended Hückel Tight-Binding theory (EHTB). The symmetry filtering effect is very helpful for finding materials for TMR junctions. Based upon which, we find a good candidate material, MnAl, for TMR applications.

DEDICATION

To my parents and my husband

LIST OF ABBREVIATIONS

AO	atomic orbital
API	application interface
BC	boundary condition
bcc	body centered cubic
CIP	current in the plane
CPP	current perpendicular to the plane
CPU	center processing unit
DOS	density of states
DRAM	dynamic random access memory
EHTB	extended Hückel tight binding
FBZ	first Brillouin zone
fcc	face centered cubic
FEM	finite element method
FM	ferromagnetic
FP	first principle
GMR	giant magnetoresistance
HSM	hierarchical storage management

LCAO	linear combination of atomic orbitals
LL	Landau-Lifshitz
LLG	Landau-Lifshitz-Gilbert
MFP	mean free path
MRAM	magnetic random access memory
MTJ	magnetic tunnel junction
NAND	not AND (a binary operation in logic)
NM	non-magnetic
NOR	not or (a binary operation in logic)
PDE	partial differential equation
PL	principle layer
SDL	spin diffusion length
SK	Slater-Koster method
SO	spin-orbit coupling
SRAM	static random access memory
STT	spin transfer torque
STT-MRAM	spin transfer torque magnetic random access memory
TB	tight biding
TMR	tunnel magnetoresistance
VASP	Vienna Ab-initio Simulation Package
XIP	execution in place

ACKNOWLEDGMENTS

Many people have been of great help to me over the course of this Ph.D. project, and I feel very much indebted to them all.

Thank you to my advisor, Dr. William. H. Butler for his patience, ready willingness to assist, and constant support through my Ph.D study period, and for his constructive criticism and careful review during the preparation of the manuscript.

I am deeply grateful to Dr. Claudia. K. A. Mewes for her constant and patient help. Her help is essentialfor me to finish the projects in this dissertation. It is a privilege and pleasure to work with her.

I would like to thank Dr. Su Gupta, Dr. Tim Mewes, and Dr. Oleg Mryasov for being the members of my dissertation committee.

A special thank you goes to Dr. Chunsheng Liu, for his previous work on the EHTB theory and code development.

I am also indebted to the faculty members of Department of Physics and Astronomy for the education and guidance I received.

During my graduate study at the University of Alabama I was supported financially by the teaching assistantship from the Department of Physics and Astronomy, the research assistantship from Dr. Su Gupta's sensors group, and the research assistantship from the DARPA STT-MRAM project. I would like to express my gratefulness here.

TABLE OF CONTENTS

LIST OF TABLES

LIST OF FIGURES

CHAPTER 1 INTRODUCTION

1.1 Motivation

The Information Age has changed human life completely and profoundly. The demand for faster data transfer rate and higher data storage density keeps increasing. In the past half century, the data storage density of all types of storage system has increased exponentially similarly to Moore's law for the semiconductor industry [1, 2], from the cheapest andslowest secondary memories (tapes, hard disk drives, etc) to the most expensive and fastest CPU cache.

Nowadays, the size of bits on hard disk drives (HDD) is approachingthe nanometer scale, or from another point of view, the areal density is reaching a terabit per square inch. As the size of the recording bit scales down, the sensitivity of the HDD heads must escalate in order to detect the tinier and tinier magnetization of the bits. The CPP-GMR effect, due to its high MR ratio, is of interest to magnetic sensor developers under such circumstances.

One would wish to have everything stored on a single memory. But it is not feasible because of cost concerns both in fabrication and in energy consumption. The traditional hierarchical storage management (HSM)is a compromise solution that consists of CPU cache, main memories, secondary memories, tertiary memories and off-line memories. The computer system can be built at an affordable level without too much tradeoff in the speed by putting the fastest and dearest SRAM closest to the CPU as the cache, using the relatively cheaper but slower DRAM as the main memory, storing the frequently-used program files and user data on

the even more cheaper but much slower HDDs and backing up everything to the cheapest and slowest tapes or optic disks. When one needs to carry data around, he/she can always choose the light-weight and small size Flash jump drives.

The complicated HSM of computer architecture could be changed entirely if there is a universal memory that can achieve the fast read/write speed comparable to SRAMs and DRAMs ata low energy consumption level, with high capacity to store the information, yet still remain relatively cheap to fabricate. Spin transfer torque magnetic random access memory (STT-MRAM) potentially has those advantages and is an emerging hot spot for the Spintronics industry[3].

1.2 Dissertation outline

This dissertation is organized as follows.

InChapter 2, we will focus on the theory of CPP-GMR effect. After a short introduction in2.1, the physical models of CPP-GMR will be explained in 2.2. The simple two-current model will be discussed first, followed by a semi-classical approach, the Valet-Fert model. Then we will demonstrate finite element method (FEM) based numerical calculations using the Valet-Fert model in 2.3.

In Chapter 3, we will present a rational approach for finding high spin polarization materials such as half metals. First, we will explain the need for finding those materials in 3.1. This will be followed by an explanation of the numerical and theoretical tools we used for understanding the material properties in 3.2. The gap theorem-based rational approach will be described in 3.3; we will then show examples in the last section,3.4

In Chapter 4, we will continue with a discussion of tunnel magnetoresistance (TMR), another perpendicular transport phenomenon. After a short introduction in 4.1, we will explain the quantum theory of the TMR effect based on Landauer-Büttiker formalism in 4.2.1 , also known as the scattering formalism. For calculation of transmission probability and conductance, the Green's function is a very powerful tool; which we will coverin 4.2.2 and 4.3.1 . Then, the calculated results of our transport program will be described in section4.3.

In Chapter 5, we will focus on magnetic damping, which plays an important role in the magnetic switching of magnetic tunnel junctions (MTJ). We will cover the basics of magnetic dynamics in 5.1, and then describe an analytical model for the calculation of the damping constant in 5.2. The calculatedresults will be shown in 5.3

In Chapter 6we will focus on how to find materials for STT-MRAMs. We will cover the basics as well as the material requirements in 6.1, and then in 6.2we will explain the symmetry filtering effect which is useful for searching for materials for the electrode and barrier in the MTJ of STT-MRAMs. In the final section of Chapter 2 in 6.3 we will focus on MnAl, a material which we think is of great potential and can serve as the electrode material in tunnel junctions with MgO as the barrier material for Spintronics applications.

CHAPTER 2 CURRENT-PERPENDICULAR-TO-PLANE GIANT MAGNETO-RESISTANCE EFFECT

2.1 Introduction

2.1.1 Short history of the CPP-GMR

Magnetoresistance is a change in the resistivity of a material due to a change in the applied magnetic field. It was discovered in 1856 byWilliam Thomson (Lord Kelvin)[4]. Anisotropic magnetoresistance (AMR) which occurs in a homogeneous magnetic material and arises from spin orbit coupling was used to make magnetic sensors for disk drives in the 1990s. However, AMR is a relatively small effect. In the late 1980s, Peter Grünberg's group from Forschungszentrum Jülich of Germany [5]discovered the Giant MagnetoResistance effect (GMR effect) in a Fe/Cr/Fe tri-layer system, meanwhile another group, Albert Fert's team from the Université Paris-Sudof France[6], also discovered this effect independently in the Fe/Cr multilayer system. This work opened the door to numerous new applicationsof the magnetoresistance phenomenon.

In both Fert and Grünberg'sGMR experiments, the current flows parallel to the multi-layer plane. This geometry is called "current in the plane" or CIP-GMR. In 1991, William Pratt et al[7, 8]performed measurements for the case in which the current flow direction is perpendicular to the multi-layer plane. This situation is called Current-Perpendicular-to-

PlaneGMR (CPP-GMR) which is oftenseveral times higher than the CIP-GMR effect for the same multi-layer configuration (see Figure 2.1).

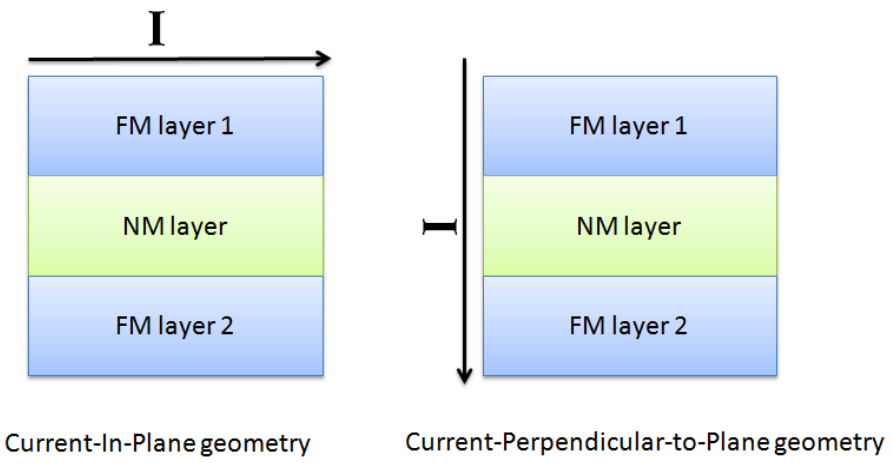

Figure 2.1.CIP and CPP geometry.In the *left* panel,the current flows parallel to the planes. In the *right*, the current is flowing perpendicular to the planes. For the CIP geometry the lateral dimensions (in the plane of the layers) are much greater than the perpendicular dimension (determined by the thickness of the layers). FM indicates a ferromagnetic layer. NM indicates a non-magnetic layer.

Both CIP-GMR and CPP-GMR originate in spin-dependent scattering of the electrons traveling between ferromagnetic layers separated by non-magnetic layers, but the detailed mechanisms that lead to magnetoresistance are different. CIP-GMR requires non-local electron conduction while CPP-GMR can be qualitatively understood via a simple picture of local conduction. For CIP-GMR, the electrons must travel between more than one magnetic layer in the direction perpendicular to the layers. This means that the mean free path (MFP) of the electrons must exceed the multilayer period for significant GMR to be measured [9, 10]. For CPP-GMR, measurements areoften more difficult because of the tiny total resistance across the thickness of a thin film in the perpendicular direction. Superconducting leads are sometimes used to reduce the base resistance therefore enhances the MR ratio $\Delta R/\Sigma R$ [8, 11].

2.1.2 Applications of the GMR effect

Due to the higher magnetoresistance comparing to traditionally used Anisotropic Magnetoresistance effects, the GMR effect is useful to the information storage industry because it allows the fabrication of nanometer scale magnetic field sensors which makes higher capacity storage devices like hard drives possible. CPP-GMR becomes more attractive as the size of the devices approaches the scale of a few tens of nanometers.

2.2 Model to explain the CPP-GMR effect

2.2.1 The Circuit model

As Sir Neville Mottproposed in his 1936 paper[12]; if the temperature is below the Curie point and if weneglect spin orbit couplingand non-collinear spins, we can treat the electron current in the conductor as a combination of two parallel currents, i.e. currents in two parallel spin channels. Mott denoted the electrons whose spins align with the local magnetic moment as belonging to the majority spin channel while those whose spins anti-align with the local magnetic moment belong to the minority spin channel. The majority spin channel sometimes is also called the up-spin channel while the minority spin channel may be called the down-spin channel. We will continue the usage of these terms to denote the two channels in the following text.

If wecan treat the two spin channels as completely independent, the CPP-GMR model can be understood by a simple picture of a circuit of resistors and the value of the magnetoresistance can be calculated by Ohm's law. Taking a simple tri-layer Ferromagnetic layer/Non-magnetic layer/Ferromagnetic layer (FM/NM/FM) system as an example, we can consider the current to be carried independently by two channels, the up spin electrons and down spin electrons. Therefore the whole system can be considered as two setsof three resistors in series (the three layers) with each set connected in parallel (the two spin channels) as shown in Figure 2.2.

The conductance of the trilayer will change if there is a change in the relative direction of the magnetization of the two layers.We usually arrange for the magnetization of one or both of the layers to be bi-stable in such a way that the relative orientation of the magnetization of the

two ferromagnetic layers is either parallel or anti-parallel. There will be five types of resistors for this trilayer system;one representing the resistance experienced by an up-spin electron passing through the magnetic layer with a left aligned magnetization ($R_{\uparrow L}$);the corresponding resistance experienced by the down spin electron passing through the magnetic layer with a left aligned magnetization ($R_{\downarrow L}$); the corresponding resistances experienced by up- and down- spin electrons passing through the magnetic layerswith a right aligned magnetization ($R_{\uparrow R}$ and $R_{\downarrow R}$ respectively). Finally, there is the resistance of the non-magnetic layer which would be the same for both up and down spins ($R_{\uparrow NM}$ and $R_{\downarrow NM}$).

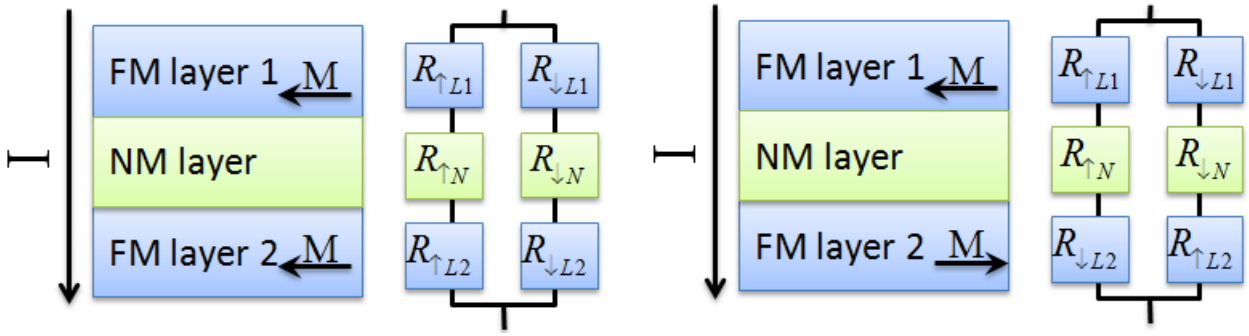

Figure 2.2. The circuit model for CPP-GMR. The current flowsvertically on the page. The *left* part of the figure shows the state in which the moments of two FM layers are aligned. The *right* half shows the state with the moments of the two FM layersanti-aligned.

The calculation of the magnetoresistance in this case is simple. For a typical FM/NM/FM tri-layer system, the total resistance when the two FM layers are aligned parallel will be,

$$R_{\Sigma P} = \frac{\left(R_{\uparrow L1} + R_{\uparrow N} + R_{\uparrow L2}\right)\left(R_{\downarrow L1} + R_{\downarrow N} + R_{\downarrow L2}\right)}{\left(R_{\uparrow L1} + R_{\uparrow N} + R_{\uparrow L2}\right) + \left(R_{\downarrow L1} + R_{\downarrow N} + R_{\downarrow L2}\right)}. \tag{1.1}$$

When the two FM layers are anti-aligned, the total resistance will be

$$R_{\Sigma AP} = \frac{\left(R_{\uparrow L1} + R_{\uparrow N} + R_{\downarrow R2}\right)\left(R_{\downarrow L1} + R_{\downarrow N} + R_{\uparrow R2}\right)}{\left(R_{\uparrow L1} + R_{\uparrow N} + R_{\downarrow R2}\right) + \left(R_{\downarrow L1} + R_{\downarrow N} + R_{\uparrow R2}\right)}. \tag{1.2}$$

Using

$$R_{\uparrow N} = R_{\downarrow N} = 2R_N = 2R_N = \frac{2\rho_N t_N}{A}, \tag{1.3}$$

where$\rho_N$is the resistivity of the non-magnetic layer, t_N, its thickness and, A, its area (which we will assume to be the same for all layers. Introducing the bulk spin asymmetry coefficient, β ,of the ferromagnets defined by,

$$\beta = \frac{\rho_\downarrow - \rho_\uparrow}{\rho_\downarrow + \rho_\uparrow}, \tag{1.4}$$

wecan write the resistance of a ferromagnetic layer as,

$$R_{\uparrow(\downarrow)} = \frac{\rho_{\uparrow(\downarrow)} t}{A} = \frac{2\rho t}{A\left[1 + (-)\beta\right]} = \frac{2\rho^* t}{A}\left[1 - (+)\beta\right]. \tag{1.5}$$

Use of the quantity, ρ^*, related to the resistivity of a ferromagnetic layer by $\rho^* = \rho / (1 - \beta^2)$ allows the GMR expression to be written in a simpler form.

We shall also assume here that the current is evenly distributed in the cross-sectional plane, i.e. the current density vector, $\vec{j}(x, y, z) = \vec{j}(z)$,where z is the perpendicular direction. The individual resistances are then,

$$
\begin{aligned}
R_{\uparrow L1} = R_{\downarrow R1} &= \frac{2\rho_1^* t_1}{A}\left(1-\beta_1\right), \\
R_{\uparrow R1} = R_{\downarrow L1} &= \frac{2\rho_1^* t_1}{A}\left(1+\beta_1\right), \\
R_{\uparrow L2} = R_{\downarrow R2} &= \frac{2\rho_2^* t_2}{A}\left(1-\beta_2\right), \\
R_{\uparrow R2} = R_{\downarrow L2} &= \frac{2\rho_2^* t_2}{A}\left(1+\beta_2\right).
\end{aligned}
\tag{1.6}
$$

The resistances considered above have been tacitly assumed to arise from the bulk resistivity that arises from the scattering of electrons by the atoms and defects within the conducting layers. However, since the current is flowing perpendicular to the interface planes, the contributionto the resistance from reflections at the interfaces between adjacent layers must also be taken into account. These contributionscan be expressed asinterface resistances that are generally different in the spin two channels[13-16]. For convenience, the spin-dependent interface resistance per unit area is often represented by the introduction of the interfacial spin asymmetry coefficient γ,

$$
r_{\uparrow(\downarrow)} = 2r_b^*\left[1-(+)\gamma\right],
\tag{1.7}
$$

where r_b^* is introduced similarly (and for the same purpose) as ρ^* in (2.5). It is related to the interfacial resistance-area product,r_b, by $r_b^* = r_b / (1-\gamma^2)$.

The interface resistance will add two additional resistances to the three layer model. Inserting the resistances in (2.6) and (2.7) into the circuit model, we obtain

$$
\begin{aligned}
\sqrt{\left(r_{\Sigma AP} - r_{\Sigma P}\right) r_{\Sigma AP}} &= \beta_1\rho_1^* t_1 + \beta_2\rho_2^* t_2 + 2\gamma r_b^*, \\
r_{\Sigma AP} &= \rho_1^* t_1 + \rho_2^* t_2 + 2r_b^*,
\end{aligned}
\tag{1.8}
$$

where $r_{\Sigma AP} = AR_{\Sigma AP}$ and $r_{\Sigma P} = AR_{\Sigma P}$ are the total resistance-area products of the anti-parallel and parallel configuration. So the MR ratio will be expressed as[8, 11],

$$MR = \frac{r_{\Sigma AP} - r_{\Sigma P}}{r_{\Sigma P}} = \left(\frac{\beta_1 \rho_1^* t_1 + \beta_2 \rho_2^* t_2 + 2\gamma r_b^*}{\rho_1^* t_1 + \rho_2^* t_2 + 2r_b^*} \right)^2 . \tag{1.9}$$

In principle, multiple electron reflections from the interfaces in an ideal GMR device should lead to constructive and destructive interference and pronounced maxima and minima in the resistance as a function of layer thickness and the electron Fermi energy wavelength. These effects (although often seen in calculations[17]) are not included in the present classical approach nor even in the semi-classical approach used in the next section. Neither, to our knowledge, have they been observed experimentally; perhaps due to imperfect interfaces between the layers.

The simple circuit model described above is incomplete in another way that is more critical, because it neglects effects that are important for describing experiments.It oversimplifies the conduction mechanism by assuming that the conductances of the two spin channels arecompletely independent and additive.A morecomplete model which includes the probability of electrons scattering between the two spin-channelsis needed. For their earliest CPP-GMR experiments the Pratt group used the Mott two current model[8]. Then the interfacial resistance was also calculated and measured for various types of interfaces and different rough nesses[14-16].In addition, the spin accumulation effects generated by the perpendicular spin current to the interface should also be considered. Johnson et al.[18], introduced the idea of spin accumulation at the interface between a ferromagnetic and nonmagnetic layer. Spin accumulation can give rise to an additional potential drop (in addition to that due to electrons reflected at the boundaries) which is proportional to the current density.

$$\Delta V = J \cdot r_{\pm\text{interface}} \tag{1.10}$$

In which, J is the current density, ΔV is the potential drop and $r_{\pm\text{interface}}$ is the spin-dependent interface resistance-area product.

2.2.2 The Valet-Fert Model

The Mott two-current model does not consider the relativistic effect of spin-orbit coupling nor non-collinear spins. It assumes that the resistances in different layers and at different interfaces are additive in the multilayer system, i.e.it assumes that the spin of an electron will not change no matter how it propagates and scatters in the material. Valet and Fert began from the Boltzmann equation and developed a more accurate macroscopic model for the case that the SDL is much longer than the MFP. The requirement of $SDL \gg MFP$ can be met by most commonly used nonmagnetic materials (Cu, Ag, etc.)and by most ferromagnets well below their Curie temperatures. At room temperature and below spin-flip scattering will arise from spin-orbit scattering, from non-collinear or "loose" spins that may arise, for example if a magnetic atom diffuses into a nonmagnetic layer, and from electron-magnon scattering[19]. In their treatment of CPP-GMR, Valet and Fert[20]assume a single parabolic conduction bandwith the same effective mass, m , and Fermi velocity, v_F , for all layers. Although it is slightly a strong condition at the surface that the conduction bands of Fe and Co are those of free electrons and identical to Cu or Ag, this assumption greatly simplifies the derivation. It should be noted that their final result does not contain these band structure parameters, and that the model has been very successful in describing the results of experiments.

The Valet-Fert model is derived from the semi-classical Boltzmann equation which introduces the electron distribution function $f_s^t\left(\vec{r},\vec{v}\right)$ to represent thenumber of s-spin electrons at position $\vec{r}$ with velocity $\vec{v}$ at time t. In steady state, therate of change of the distribution function (which is the sum of terms resulting from drift, field and scattering) should vanish. Valet and Fert also distinguish between "momentum scattering" which conserves spin and "spin-flip scattering" which does not,

$$\frac{df}{dt}=0=\left.\frac{\partial f}{\partial t}\right|_{\text{drift}}+\left.\frac{\partial f}{\partial t}\right|_{field}+\left.\frac{\partial f}{\partial t}\right|_{\text{momentum scattering}}+\left.\frac{\partial f}{\partial t}\right|_{\text{spin-flip scattering}}. \tag{1.11}$$

In this equation, the drift term describes the rate of change of the distribution function due to the movement of electrons caused by their velocity; the field term describes the rate of change of the distribution function due to the acceleration of the electrons causedby the applied external field; the momentum scattering term describes the change in the distribution function due to the scattering of electrons by the imperfections in the lattice which change their momentum, but not their spin; and the spin-flip scattering term describesthe change in the distribution function due to scattering processes which change spin. From the definition of each term, we have the following,

$$\left.\frac{\partial f}{\partial t}\right|_{\text{drift}}=-\vec{v}\left(\vec{k}\right)\cdot\nabla_{\vec{r}}f_s^t\left(\vec{r},\vec{v}\right), \tag{1.12}$$

$$\left.\frac{\partial f}{\partial t}\right|_{\text{field}}=-\frac{\partial f_s^t\left(\vec{r},\vec{v}\right)}{\partial\vec{v}}\frac{\partial\vec{v}}{\partial t}=\frac{e}{\hbar}\vec{E}\cdot\nabla_{\vec{v}}f_s^t\left(\vec{r},\vec{v}\right), \tag{1.13}$$

$$\begin{aligned}\left.\frac{\partial f}{\partial t}\right|_{\text{momentum scattering}}&=\sum_{\vec{v}'}P_{\vec{v}\vec{v}'}\left\{f_s^t\left(\vec{r},\vec{v}'\right)\left[1-f_s^t\left(\vec{r},\vec{v}\right)\right]-f_s^t\left(\vec{r},\vec{v}\right)\left[1-f_s^t\left(\vec{r},\vec{v}'\right)\right]\right\}\\&=\sum_{\vec{v}'}P_{\vec{v}\vec{v}'}\left[f_s^t\left(\vec{r},\vec{v}'\right)-f_s^t\left(\vec{r},\vec{v}\right)\right],\end{aligned} \tag{1.14}$$

$$\left.\frac{\partial f}{\partial t}\right|_{\text{spin-flip scattering}} = \sum_{\vec{v}'} P^{sf}_{\vec{v}\vec{v}'}\left\{f^t_{-s}(\vec{r},\vec{v}')\left[1-f^t_s(\vec{r},\vec{v})\right]-f^t_s(\vec{r},\vec{v})\left[1-f^t_{-s}(\vec{r},\vec{v}')\right]\right\}$$
$$= \sum_{\vec{v}'} P^{sf}_{\vec{v}\vec{v}'}\left[f^t_{-s}(\vec{r},\vec{v}')-f^t_s(\vec{r},\vec{v})\right]. \quad (1.15)$$

In equation(2.14), $P_{\vec{v}\vec{v}'}f^t_s(\vec{r},\vec{v})$ is the probability for an electron to be scattered from its initial state $\vec{v}$ to another state $\vec{v}'$. This is the momentum "scattering out" term. The other term on the right-hand side of this equation, $-P_{\vec{v}\vec{v}'}f^t_s(\vec{r},\vec{v}')$ is the probability for an electron in state $\vec{v}'$ to scatter into state $\vec{v}$. This is the momentum "scattering-in" term. In equation(2.15),the term $P^{sf}_{\vec{v}\vec{v}'}f^t_s(\vec{r},\vec{v})$ is the probability for an electron initially in state (s,v) to scatter out of that state and into state $(-s,\vec{v}')$ via spin-flip scattering. This is the spin-flip "scattering-out" term. The other term $P^{sf}_{\vec{v}\vec{v}'}f^t_{-s}(\vec{r},\vec{v}')$, is the spin-flip "scattering-in" term.

Therefore, the steady state Boltzmann equation can be obtained by substituting each term described above into equation(2.11),

$$-\vec{v}\cdot\nabla_{\vec{r}}f_s(\vec{r},\vec{v})+\frac{e}{\hbar}\vec{E}\cdot\nabla_{\vec{v}}f_s(\vec{r},\vec{v})+\sum_{\vec{v}'}P_{\vec{v}\vec{v}'}\left[f_s(\vec{r},\vec{v}')-f_s(\vec{r},\vec{v})\right]$$
$$+\sum_{\vec{v}'}P^{sf}_{\vec{v}\vec{v}'}\left[f_{-s}(\vec{r},\vec{v}')-f_s(\vec{r},\vec{v})\right]=0. \quad (1.16)$$

This is the same as the Boltzmann equation given by Valet and Fert in their 1993 paper [20]except they treat the Boltzmann equation witha continuous integral over the velocity instead of the discrete summation that we use here. It should be understood that the summation over velocity shown here should actually indicate a sum over k-points and energy bands. Valet and Fert tacitly assume that all layers, non-magnetic and magnetic, up-spin and down-spin have the same free electron dispersion relation so that velocity has a one to one relationship to momentum.

For the steady state distribution $f_s(\vec{r},\vec{v})$, we can introduce the anisotropic deviation function, $g_s(\vec{r},\vec{v})$, through,

$$f_s(\vec{r},\vec{v}) = f_0 + \frac{\partial f_s^0(\varepsilon_{\vec{v}}-\mu_0)}{\partial \varepsilon_{\vec{v}}}\left\{\mu^0 - \mu_s(\vec{r}) + g_s(\vec{r},\vec{v})\right\}, \tag{1.17}$$

which recognizes that the deviation of the distribution function from its equilibrium value, f_0, is confined to the vicinity of the Fermi energy. The deviation of the distribution function is further divided into a part which is isotropic (independent of $\vec{v}$), $\frac{\partial f_s^0(\varepsilon_{\vec{v}}-\mu_0)}{\partial \varepsilon_{\vec{v}}}\left\{\mu^0 - \mu_s(\vec{r})\right\}$ and a part which averages to zero over the Fermi surface, $\frac{\partial f_s^0(\varepsilon_{\vec{v}}-\mu_0)}{\partial \varepsilon_{\vec{v}}} g_s(\vec{r},\vec{v})$. We can simplify the field term by retaining only the equilibrium part of the distribution function in that term under the assumption that the electric field is small so that $(f-f_0)\vec{E}$ is higher order than $(f-f_0)$. Additional simplification of the field term can be obtained by using,

$$\nabla_{\vec{v}} f_s^0(\varepsilon_{\vec{v}}-\mu_0) = \frac{\partial f_s^0(\varepsilon_{\vec{v}}-\mu_0)}{\partial \varepsilon_{\vec{v}}}\nabla_{\vec{v}}\varepsilon_{\vec{v}} = \frac{\partial f_s^0(\varepsilon_{\vec{v}}-\mu_0)}{\partial \varepsilon_{\vec{v}}}\hbar\vec{v}. \tag{1.18}$$

With these substitutions, the four terms in equation(2.16)can be written as,

$$\begin{aligned}
\frac{e}{\hbar}\vec{E}\cdot\nabla_{\vec{v}} f_s^0(\varepsilon_{\vec{v}}-\mu_0) &= e\frac{\partial f_s^0(\varepsilon_{\vec{v}}-\mu_0)}{\partial \varepsilon_{\vec{v}}}\vec{E}\cdot\vec{v}, \\
-\vec{v}\cdot\nabla_{\vec{r}} f_s(\vec{r},\vec{v}) &= -\frac{\partial f_s^0(\varepsilon_{\vec{v}}-\mu_0)}{\partial \varepsilon_{\vec{v}}}\vec{v}(\vec{k})\cdot\nabla_{\vec{r}}\left[-\mu_s(\vec{r}) + g_s(\vec{r},\vec{v})\right], \\
\sum_{\vec{v}'} P_{\vec{v}\vec{v}'}\left[f_s(\vec{r},\vec{v}') - f_s(\vec{r},\vec{v})\right] &= -\frac{\partial f_s^0(\varepsilon_{\vec{v}}-\mu_0)}{\partial \varepsilon_{\vec{v}}}\frac{g_s(\vec{r},\vec{v})}{\tau_s}, \\
\sum_{\vec{v}'} P_{\vec{v}\vec{v}'}^{sf}\left[f_{-s}(\vec{r},\vec{v}') - f_s(\vec{r},\vec{v})\right] &= \frac{\partial f_s^0(\varepsilon_{\vec{v}}-\mu_0)}{\partial \varepsilon_{\vec{v}}}\left[-\mu_{-s}(\vec{r}) + \mu_s(\vec{r}) - g_s(\vec{r},\vec{v})\right]\frac{1}{\tau_{sf}}.
\end{aligned} \tag{1.19}$$

The third and fourth terms depend on the approximations,

$$\sum_{\vec{v}'} P_{\vec{v}\vec{v}'} \frac{\partial f_s^0\left(\varepsilon_{\vec{v}'} - \mu_0\right)}{\partial \varepsilon_{\vec{v}'}} g_s\left(\vec{r}, \vec{v}'\right) = 0, \tag{1.20}$$

and,

$$\sum_{\vec{v}'} P_{\vec{v}\vec{v}'}^{sf} \left[\frac{\partial f_{-s}^0\left(\varepsilon_{\vec{v}'-s} - \mu_0\right)}{\partial \varepsilon_{\vec{v}'-s}} g_{-s}\left(\vec{r}, \vec{v}'\right) \right] = 0. \tag{1.21}$$

These are equivalent respectively to the assumptions that the momentum and spin-flip scattering probabilities are isotropic since, by construction,

$$\sum_{\vec{v}'} \frac{\partial f^0\left(\varepsilon_{\vec{v}'} - \mu_0\right)}{\partial \varepsilon_{\vec{v}'}} g_{\pm s}\left(\vec{r}, \vec{v}'\right) = 0. \tag{1.22}$$

It should be remembered that Valet and Fert assume that all bands in all layers for both spins are those of free electrons with the same dispersion relation.

Use of (2.19), (2.20), and (2.21) in (2.16) yields,

$$-\frac{\partial f_s^0\left(\varepsilon_{\vec{v}} - \mu_0\right)}{\partial \varepsilon_{\vec{v}}} \left[\vec{v} \cdot \nabla_{\vec{r}} \left[-\mu_s\left(\vec{r}\right) + g_s\left(\vec{r}, \vec{v}\right) \right] - e\vec{E} \cdot \vec{v} + g_s\left(\vec{r}, \vec{v}\right) \left(\frac{1}{\tau_s} + \frac{1}{\tau_{sf}} \right) + \frac{\mu_{-s}\left(\vec{r}\right) - \mu_s\left(\vec{r}\right)}{\tau_{sf}} \right] = 0. \tag{1.23}$$

The spatial gradient of the chemical potential can be included in the field term by defining an electrochemical potential, $\bar{\mu}_s\left(\vec{r}\right) = \mu_s\left(\vec{r}\right) - e\vec{V}\left(\vec{r}\right)$ which allows us to write (2.23) as,

$$\frac{\partial f^0\left(\varepsilon_{\vec{v}} - \mu_0\right)}{\partial \varepsilon_{\vec{v}}} \left[\vec{v} \cdot \nabla_{\vec{r}} g_s\left(\vec{r}, \vec{v}\right) + \left(\frac{1}{\tau_s} + \frac{1}{\tau_{sf}} \right) g_s\left(\vec{r}, \vec{v}\right) - \vec{v} \cdot \nabla_{\vec{r}} \bar{\mu}_s\left(\vec{r}\right) - \frac{\mu_s\left(\vec{r}\right) - \mu_{-s}\left(\vec{r}\right)}{\tau_{sf}} \right] = 0. \tag{1.24}$$

If we average equation (2.24) over the Fermi surface by applying $\sum_{\vec{v}}$ to all terms, we can see that the second and third terms vanish leaving,

$$\sum_{\vec{v}} \frac{\partial f^0\left(\varepsilon_{\vec{v}} - \mu_0\right)}{\partial \varepsilon_{\vec{v}}} \left[\vec{v} \cdot \nabla_{\vec{r}} g_s\left(\vec{r}, \vec{v}\right) - \frac{\mu_s\left(\vec{r}\right) - \mu_{-s}\left(\vec{r}\right)}{\tau_{sf}} \right] = 0. \tag{1.25}$$

Similarly, if we multiply (2.24) by v_x and integrate over the Fermi surface, we have,

$$\sum_{\vec{v}} \frac{\partial f^0\left(\varepsilon_{\vec{v}} - \mu_0\right)}{\partial \varepsilon_{\vec{v}}} \left[\left(\frac{1}{\tau_s} + \frac{1}{\tau_{sf}} \right) v_x g_s\left(\vec{r}, \vec{v}\right) - v_x^2 \frac{\partial \overline{\mu}_s\left(\vec{r}\right)}{\partial x} \right] = 0. \tag{1.26}$$

In writing (2.26), we assumed that $\nabla_{\vec{r}} g_s\left(\vec{r}, \vec{v}\right)$ has odd parity in $\vec{v}$. This equation can be recognized as the expression for the local current density in the free electron approximation,

$$J_{sx} = \frac{e}{V} \sum_{\vec{v}} \frac{\partial f^0\left(\varepsilon_{\vec{v}} - \mu_0\right)}{\partial \varepsilon_{\vec{v}}} v_x g_s\left(\vec{r}, \vec{v}\right) = \frac{e}{V} \sum_{\vec{v}} \frac{\partial f^0\left(\varepsilon_{\vec{v}} - \mu_0\right)}{\partial \varepsilon_{\vec{v}}} \left[v_x^2 \frac{\partial \overline{\mu}_s\left(\vec{r}\right)}{\partial x} \right] \left(\frac{1}{\tau_s} + \frac{1}{\tau_{sf}} \right)^{-1}, \tag{1.27}$$

or, more generally,

$$\vec{J}_s = \frac{e}{V} \sum_{\vec{v}} \frac{\partial f^0\left(\varepsilon_{\vec{v}} - \mu_0\right)}{\partial \varepsilon_{\vec{v}}} \vec{v} g_s\left(\vec{r}, \vec{v}\right) = \frac{e}{3V} \sum_{\vec{v}} \frac{\partial f^0\left(\varepsilon_{\vec{v}} - \mu_0\right)}{\partial \varepsilon_{\vec{v}}} v^2 \nabla_{\vec{r}} \overline{\mu}_s \left(\frac{1}{\tau_s} + \frac{1}{\tau_{sf}} \right)^{-1} = \frac{\sigma_s}{e} \nabla_{\vec{r}} \overline{\mu}_s, \tag{1.28}$$

where V is the volume and σ_s is the free electron conductivity,

$$\sigma_s = \frac{e^2 v_F^2}{3V} N\left(E_F\right) \left(\frac{1}{\tau_s} + \frac{1}{\tau_{sf}} \right)^{-1}, \tag{1.29}$$

where $N(E_F)$, is the Fermi energy density of states.

The meaning of (2.25)now also becomes apparent,

$$\nabla \cdot \vec{J}_s = \frac{e}{V} \sum_{\vec{v}} \frac{\partial f^0\left(\varepsilon_{\vec{v}} - \mu_0\right)}{\partial \varepsilon_{\vec{v}}} \left[\vec{v} \cdot \nabla_{\vec{r}} g_s\left(\vec{r}, \vec{v}\right) \right] = \frac{e}{V} N\left(E_F\right) \frac{\mu_s\left(\vec{r}\right) - \mu_{-s}\left(\vec{r}\right)}{\tau_{sf}}, \tag{1.30}$$

so that the term involving the difference of the chemical potentials serves asa source or sink term for the spin-channel current densities.Using (2.29), the right-hand side of (2.30) can be written in terms of the spin-channel conductivity as

$$\nabla \cdot \vec{J}_s = \frac{\sigma_s}{e}\frac{\left(\mu_s(\vec{r}) - \mu_{-s}(\vec{r})\right)}{l_{sf}^2}, \text{ where } l_{sf}^2 = \frac{v_F^2 \tau_{sf}}{3}\left(\frac{1}{\tau_s} + \frac{1}{\tau_{sf}}\right)^{-1}. \tag{1.31}$$

The quantity denoted l_{sf} is called the spin-diffusion length. Its physical meaning can be explained in terms of an electron with spin s traveling a distance,

$$\lambda_s = v_F\left(\frac{1}{\tau_s} + \frac{1}{\tau_{sf}}\right)^{-1} \tag{1.32}$$

between scattering events. A very small fraction of these events will cause the spin to flip $\left(\tau_{sf} >> \tau_s\right)$. Since we are assuming that the scattering is isotropic, the electron will perform a three dimensional random walk between events that flip the spin. The number of steps in this random walk will be $n = \tau_{sf} / \tau_s$. The mean square displacement of the electron during these *n* steps will be $n\lambda_{sf}^2 / 3 = l_{sf}^2$.

Equations (2.28) and (2.31) can be written as,

$$\vec{J}_s = \frac{\sigma_s}{e}\nabla_{\vec{r}}\overline{\mu}_s; \quad \text{and} \quad \frac{e}{\sigma_s}\nabla_{\vec{r}} \cdot \vec{J}_s = \frac{\overline{\mu}_s - \overline{\mu}_{-s}}{l_s^{\,2}}. \tag{1.33}$$

Then, by introducing the spin dependent chemical potential $\overline{\mu}_{\pm} = \overline{\mu} \pm \Delta\mu$ from the spin accumulation term $\Delta\mu$, the two equations can be transformed into two partial differential equations.

$$\nabla_{\vec{r}}^{\,2}\Delta\mu = \frac{\Delta\mu}{l_{sf}^{\,2}} \tag{1.34}$$

$$\nabla_{\vec{r}}^{\,2}\left(\sigma_+\overline{\mu}_+ + \sigma_-\overline{\mu}_-\right) = 0 \tag{1.35}$$

The current should be continuous across the interface neglecting the spin relaxation at the interface.

$$J_s\big|_{\text{LHS of the interface}} - J_s\big|_{\text{RHS of the interface}} = 0 \tag{1.36}$$

For the electrochemical potential, it should be continuous too if the interface scattering is also neglected. However, if wedo take the interface scattering into account, then the potential should have a drop at the interface, i.e.

$$\bar{\mu}_s\big|_{\text{LHS of the interface}} - \bar{\mu}_s\big|_{\text{RHS of the interface}} = r_s\left[\vec{J}_s\big|_{\text{at the interface}} / e\right] \tag{1.37}$$

Now wehave built the partial differential equation (PDE) system on two unknowns $\bar{\mu}_+$ and $\bar{\mu}_-$. There is a Dirichlet boundary condition(BC)(2.36), aNeumann BC(2.37), and two combined PDEs (2.34)and (2.35).This equation system can be solved analytically and straight forwardly for ideal cases such as the cross-section remains the same in all the three layers of the tri-layer CPP device, current flows perpendicularly without any drift in the parallel-to-plane direction.

However, in actually devices, the assumption of same cross-section in every layeris not true. We may have mixed BCs on the same geometrical plane. Hence the analytical solution would not be obtained anymore. Effects such as unevenly distributed current are also concerns for typical CPP spin valves, especially for those with pinholes in the non-magnetic center layer in which the current distribution will be far from homogenous. An example of actual current distribution in a tri-layer CPP spin valve with a pin-hole type non-magnetic center layer is shown in the figure below. Therefore, a numerical implementation based on the finite element method is quite convenient.

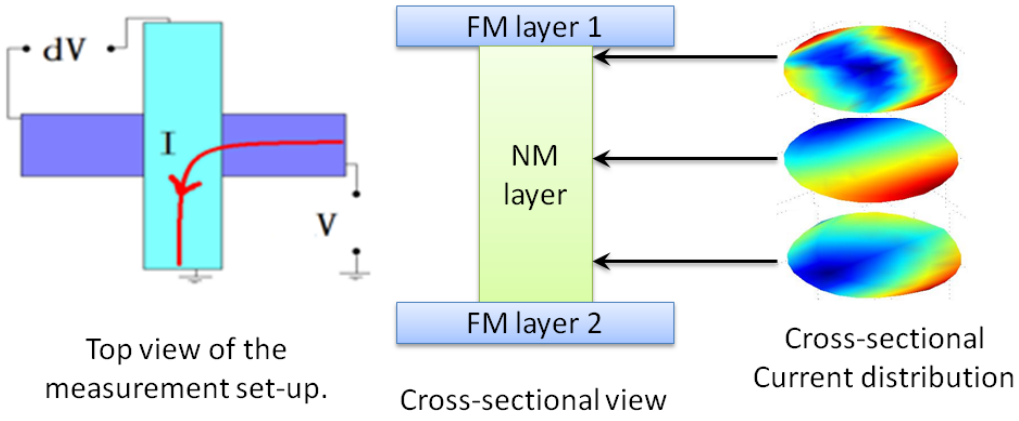

Figure 2.3.Actual current distribution of a CPP-GMR spin valve with a pin-hole type center non-magnetic layer. In the *left* it shows how the measurement is set up. In the *right,* there are three cross-sectional current distribution figures taken at three different heights across one of the many conducting pin-holes in the center non-magnetic layer. The current distribution is calculated by numerical simulation with COMSOL 3D AC/DC module.We can see that current distribution is not uniform.

2.3 FEM based calculations of CPP-GMR using the Valet-Fert Model

2.3.1 COMSOL PDE module

Several partial differential equation (PDE) solver software tools are available. Bothgeneral solvers like FlexPDE and MATLAB as well as pre-defined solvers such as COMSOL Multiphysics and SpinFlow 3Dare available. Implementation of the Valet-Fert model will be demonstrated usingthe PDE module of COMSOL Multiphysics 3.5; however the principles used in the implementation can be transferred to other PDE solvers.

COMSOLMultiphysics, formerly known as FEMLAB, is a commercial PDE solver with cross-platform capabilities as well as computer-aided design (CAD) and a MATLABapplication interface (API). It is specially optimized for coupled phenomena and has a numerous pre-defined modules such as AC/DC (alternating current/direct current) module, heat transfer module, RF (radio frequency) module, etc. Only the basic PDE module is required for the Valet-Fert model implementation, although coupled analysis using one or more of the pre-defined modules (e.g. the heat transfer analysis in conjunction with current transport analysis)may potentially be of interest.

We can use the general PDE form or the coefficient PDE form of COMSOL Multiphysics. The coefficient form is for linear or quasi-linear PDEs while the general form can go further to implement nonlinear PDEs. Either is sufficient for basic Valet-Fert model.

In the general formin COMSOL, the PDE, the Neumann Boundary Condition (BC)and the Dirichlet BC are written as shown in(2.38)respectively,

$$
\begin{aligned}
&\nabla \cdot \Gamma = F && \text{in subdomain } \Omega \\
&-\vec{n} \cdot \Gamma = G + \left(\frac{\partial R}{\partial u} \right)^T \mu && \text{on boundary } \partial\Omega \\
&0 = R && \text{on boundary } \partial\Omega
\end{aligned}, \tag{1.38}
$$

in which the terms Γ, F, G, and R are coefficients thus can be expressed as functions of the spatial coordinates, the variable-to-solve μ or even the space derivatives of μ. F, Γ is a flux vector while G, and R are scalars. The $\left(\frac{\partial R}{\partial u} \right)^T$ is the transpose of $\frac{\partial R}{\partial u}$. The μ is the variable that user are solving for. In the Valet Fert Model, it can be chosen to be the electrochemicalpotemtial.

The first equation in (2.38) can be recognized as the continuity equation. The flux vector Γ can be chosen to be the currentdefined by, $\vec{J}_s = \sigma_s \cdot \nabla \overline{\mu}_s$, which in the most general case is a 6-dimensional vector field (three spatial coordinates and two spin coordinates) and the source term, F is a two dimensional vector field given by, $\frac{\sigma_{-s}}{l_{sf}^2 \left(\sigma_s + \sigma_{-s} \right)} \left(\mu_s - \mu_{-s} \right)$. The second equation in(2.38),also known as the generalized Neumann BC,can be called as a Robin BC. The third equation in (2.38) is the Dirichlet BC. In finite element terminology, the Dirichlet BC is also called the essential BC while the Neumann BC is called the natural BC.

The BC can be of the Neumann type (also called type II), the Dirichlet type (also called type I) or the Robin type (also called type III) which is a linear combination of types I and II. The boundary condition can also be mixed meaning that it is, for example, type I over part of the boundary and type II over the remainder.

Returning to equations (2.34)and(2.35),we need to transform the Valet-Fert equations into the format of (2.38),

$$\nabla_{\vec{r}} \cdot \vec{J}_+ = \frac{\sigma_-}{l_{sf}^2\left(\sigma_+ + \sigma_-\right)}\left(\mu_+ - \mu_-\right)$$
$$\nabla_{\vec{r}} \cdot \vec{J}_- = \frac{-\sigma_+}{l_{sf}^2\left(\sigma_+ + \sigma_-\right)}\left(\mu_+ - \mu_-\right) \quad (1.39)$$

.

Hence, the coefficient F for the two variables will be $\frac{\sigma_-}{l_{sf}^2\left(\sigma_+ + \sigma_-\right)}\left(\mu_+ - \mu_-\right)$ and $\frac{-\sigma_+}{l_{sf}^2\left(\sigma_+ + \sigma_-\right)}\left(\mu_+ - \mu_-\right)$ respectively. Similarly the BCscan be transformed to,

$$\begin{aligned} -\vec{n} \cdot \vec{J}_s &= 0 \\ 0 &= \overline{\mu}_s\big|_{\text{LHS of the interface}} - \overline{\mu}_s\big|_{\text{RHS of the interface}} - \frac{r_s}{e}\vec{J}_s\big|_{\text{at the interface}} \\ V_s &= \overline{\mu}_s\big|_{\text{at the interface}}, \end{aligned} \quad (1.40)$$

in which the first one can be applied to the lateral boundaries that has no current inflow and outflow, the second one needs to be applied tothe center interface where the spin accumulation occurs, and the third one applies to the boundaries where the voltage is applied to introduce the electric current.

In the coefficient form of COMSOL, the PDE, the Neumann Boundary Condition (BC) and the Dirichlet BC are written as shown in(2.41)respectively, which is mathematically equivalent to (2.38) (e.g. $\Gamma = c\nabla u + \alpha u - \gamma$),

$$\begin{aligned} &e_a \frac{\partial^2 \mu}{\partial t^2} + d_a \frac{\partial \mu}{\partial t} + \nabla \cdot \left(-c\nabla u - \alpha u + \gamma\right) + \beta \cdot \nabla u + au = f && \text{in subdomain } \Omega \\ &n \cdot \left(c\nabla u + \alpha u - \gamma\right) + qu = g - h^T u && \text{on boundary } \partial\Omega \\ &hu = r && \text{on boundary } \partial\Omega, \end{aligned} \quad (1.41)$$

in which c , α , β , γ , a , q , h , f , g , and r are all user-defined coefficients. Unlike the general PDE form, they can only be functions of the spatial coordinates, not the variable-to-solve μ .

Similar to what we've done in the general form. The general form of the flux vector is, $\Gamma = c\nabla u + \alpha u - \gamma$. In our case, it will be a vector composed of the up and down spin currents. We can rewrite the Valet-Fert equation system, (2.34), as

$$\begin{aligned} &\Delta\mu_+ - \Delta\mu_- - \frac{1}{l_{sf}^2}\left(\mu_+ - \mu_-\right) = 0 \\ &\sigma_+\Delta\mu_+ + \sigma_-\Delta\mu_- = 0 \end{aligned} \quad . \tag{1.42}$$

Comparing to the first equation in(2.41), the coefficients α, β, γ and f will all vanish.The surviving coefficients c and a will be

$$\begin{aligned} c &= \begin{pmatrix} 1 & -1 \\ \sigma_+ & \sigma_- \end{pmatrix} \\ a &= \begin{pmatrix} -\frac{1}{l_{sf}^2} & \frac{1}{l_{sf}^2} \\ 0 & 0 \end{pmatrix}. \end{aligned} \tag{1.43}$$

The BCswill be,

$$\begin{aligned} -\vec{n}\cdot\sigma_s\nabla\overline{\mu}_s\big|_s &= 0 \\ 0 &= \overline{\mu}_s\big|_{\text{LHS of the interface}} - \overline{\mu}_s\big|_{\text{RHS of the interface}} - \frac{r_s\sigma_s}{e^2}\nabla\overline{\mu}_s\big|_{\text{at the interface}} \\ V_s &= \overline{\mu}_s\big|_{\text{at the interface}}, \end{aligned} \tag{1.44}$$

which is the same as the BCs in (2.40).

The PDE system can be setup described above in either form, general or coefficient. They are fundamentally equivalent. Since the general PDE form has more flexibility and is more difficult to implement, the implementation below will be shown in this way. Easier coefficient PDE form implementation can be achieved similarly. The actual implementation of general PDE implementation is tricky, especially for the BCs. We can choose to use more variables similar to

the method described in 2.2.1 or take advantage of COMSOL's multi-physics feature and use multiple modulesinstead of one PDE module.

2.3.2 Direct implementation.

Using the example A in the Section III of Ref. [20], the method of direct implementation will be shown below. As Valet and Fert described, the example will be "at the interface located at z=0, assumed to have zero resistance, separating two semi-infinite ferromagnetic metals having opposite magnetizations". Therefore we can setup the geometry and choose the variables in COMSOL like what is shown in Figure 2.4 for 2D cases (1D and 3D cases can be implemented similarly).

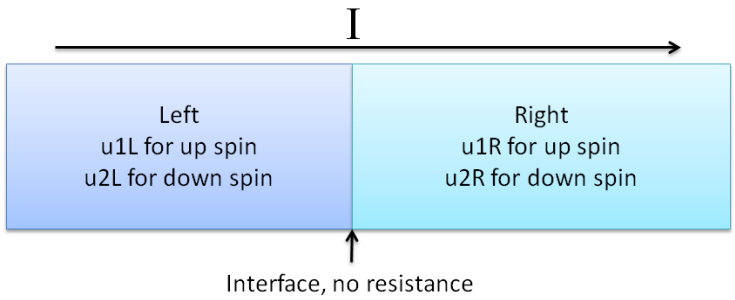

Figure 2.4. COMSOL setup for Valet-Fert III.A example

Therefore the setup of coefficient functions F and Γ can be setup as described in the following table. Constants C_1 and C_2 corresponds to the coefficients $\frac{\sigma_-}{l_{sf}^2(\sigma_+ + \sigma_-)}$ and $\frac{-\sigma_+}{l_{sf}^2(\sigma_+ + \sigma_-)}$ in equation (2.39) respectively. Here the notation $u1Lx$ is actually $\frac{\partial u1L}{\partial x}$ in COMSOL language. Special letters x, y, z at the end of the variable-to-be-solved will be interpreted by COMSOL compiler as the first order derivative of on that direction automatically

while double letters xx, xy, yy means second order derivative. The detailed implementation is shown in Table 1.

Table 1.Coefficients direct setup in the COMSOL-based 2D Valet-Fert model

	Subdomain settings	
	Left sub-domain	Right sub-domain
Flux vector Γ	$\sigma_+ \cdot \mu 1Lx$ $\sigma_- \cdot \mu 2Ly$	$\sigma_- \cdot \mu 1Rx$ $\sigma_+ \cdot \mu 2Ry$
Source term F	$\frac{\sigma_-}{l_{sf}^2(\sigma_+ + \sigma_-)}(u1L - u2L)$ $\frac{-\sigma_+}{l_{sf}^2(\sigma_+ + \sigma_-)}(u1L - u2L)$	$\frac{\sigma_+}{l_{sf}^2(\sigma_+ + \sigma_-)}(u1R - u2R)$ $\frac{-\sigma_-}{l_{sf}^2(\sigma_+ + \sigma_-)}(u1R - u2R)$
	Boundary settings	
Left (Dirichlet BC)	Center (Dirichlet BC)	Right (Dirichlet BC)
$G = \begin{bmatrix} j_0 \cdot \frac{1-\beta}{2} \\ j_0 \cdot \frac{1+\beta}{2} \end{bmatrix}$ $R = \begin{bmatrix} u1L - V_L \\ u2L - V_L \end{bmatrix}$	$G = \begin{bmatrix} \sigma_+ \cdot \mu 1Lx + \sigma_- \cdot \mu 1Rx \\ \sigma_- \cdot \mu 2Lx + \sigma_+ \cdot \mu 2Rx \end{bmatrix}$ $R = \begin{bmatrix} -u1L + u1R \\ -u2L + u2R \end{bmatrix}$	$G = \begin{bmatrix} j_0 \cdot \frac{1+\beta}{2} \\ j_0 \cdot \frac{1-\beta}{2} \end{bmatrix}$ $R = \begin{bmatrix} u1R - V_R \\ u2R - V_R \end{bmatrix}$

All other BCs are setup as Neumann BC to make sure there is no current inflow and outflow on those irrelevant interfaces. The total current is j_0. The voltage applied on either ends are V_L and V_R respectively. Note that they are not independent.

Therefore, the III A example is well established. The2D calculation results are shown in Figure 2.5comparing to the 1D result given in Valet and Fert's paper. We can setup 1D and 3D Valet-Fert model in the similar way. And the method can be extended to the systems with more layers, e.g. the examples described in III B of Valet and Fert's original paper.

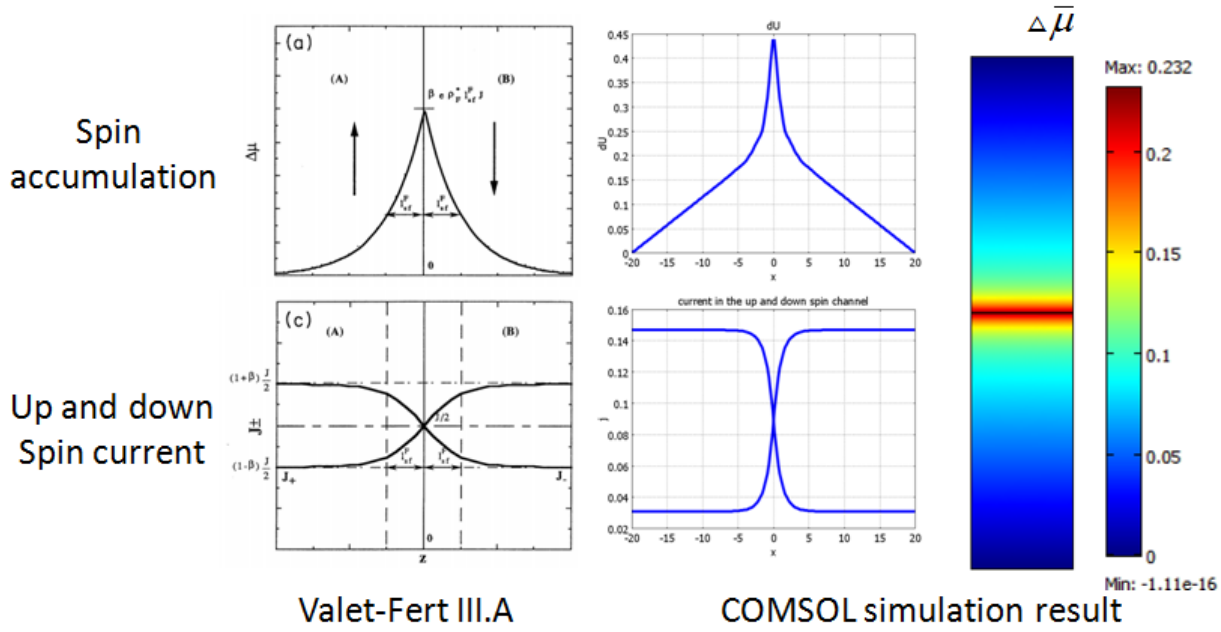

Figure 2.5. Comparison between original graphs and COMSOL 2D simulation results for Valet-Fert IIIA using direct implementation.

2.3.3 Multiphysics implementation

Though the Valet Fert model can be implemented directly as described in the previous chapter, we can see that the number of variables is in fact twice the total number of layers in the system. CPP-GMR devices usually have several layers, which will leads to dealing with dozens of variables in the same module at the same time. Therefore the direct implementation is tedious anderror-prone for actual device simulations. Moreover, COMSOL has limited number of boundary conditions that one can implement in a module which is inconvenient for introducing the interface resistances into the simulation.

COMSOL Multiphysics has a feature that can dealwith different variables in different modules and coupling them via global functions. Taking advantage of this ability, we can implementa simpler procedure for solving the Valet-Fert equations. In this approach, we

usemultiple PDE modules at the same time, one for the each layer. In each module, there will be two variables; one is for the up spin electrochemical potential, the other for the down spin one.The variables will be confined to their own layers, i.e. their own modules. This approach simplifies the specification of the PDEs and theirBCs.

To illustrate this approach, we again use Valet-Fert III.A as an example. But this time we treat the problem in three dimensions. At the beginning of the model setup, one should enable Multiphysics and add two modules, as shown in Figure 2.6.

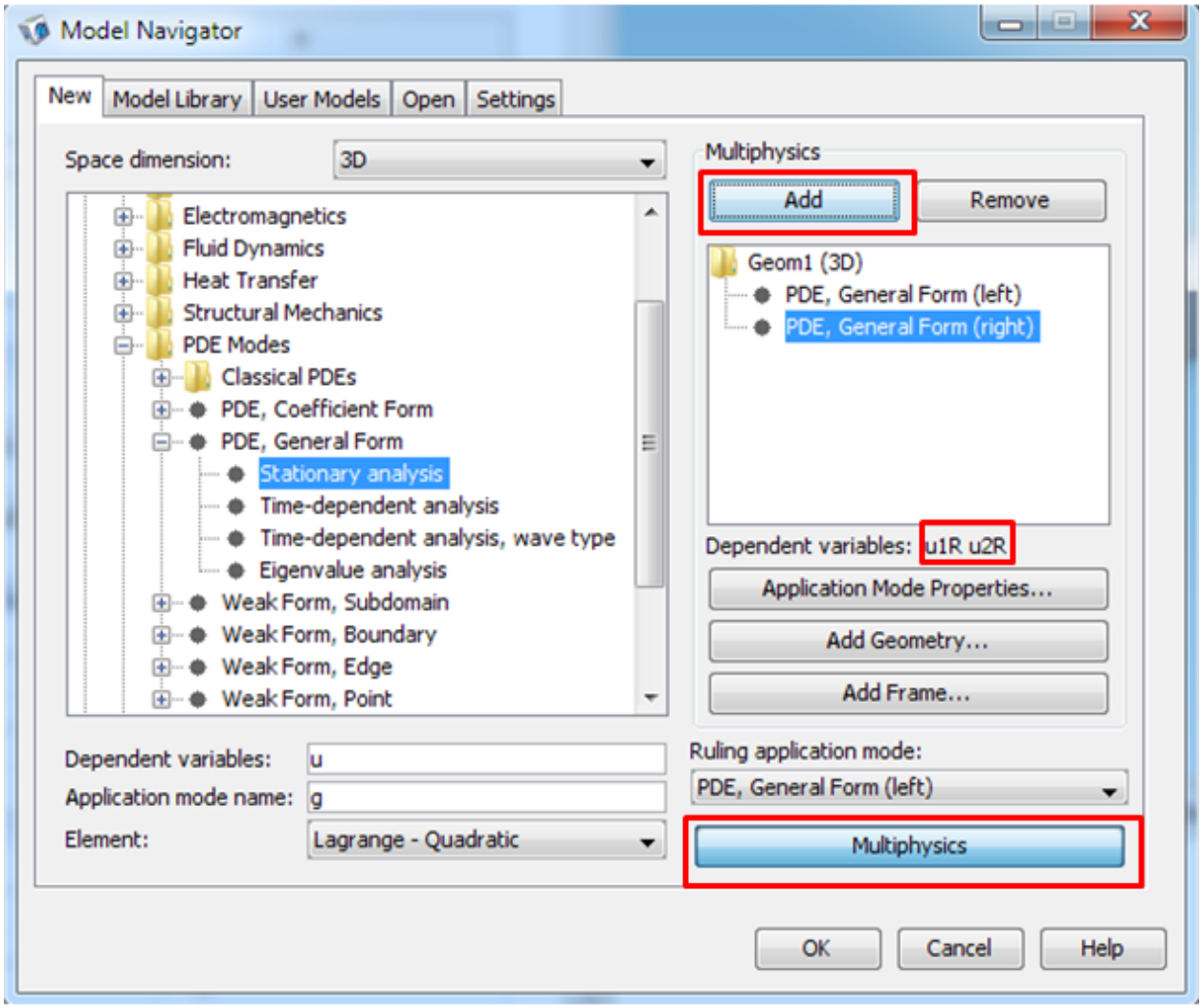

Figure 2.6. Enabling of Multiphysics and adding two modules with the proper choice of variables in each module.

We choose the variables as Figure 2.4, $u1L$ and $u2L$ for the left module, $u1R$ and $u2R$ for the right module. But it is actually not necessary. One can choose $u1$ and $u2$ for the left module and still use $u1$ and $u2$ for the right module. Since they are in different modules now, the same name here is permitted.

The PDEs and BCs on the left and right are the same as described in Table 1. But the BC at the center interface will now differ. Since we have two modules here, we are actually having two BCs for the center interface, one in each module. Instead of using Dirichlet BC, we implement a Neumann type. In one module, we setup the boundary flux term as,

$$G = M \cdot \left(u1L - u2R \right) \tag{1.45}$$

Then in the other module, on the same interface, we setup the boundary flux term as,

$$G = -M \cdot \left(u1L - u2R \right) \tag{1.46}$$

Choosing M to be a big positive number, e.g. 10000, the BC here is actually requiring the terms inside the parenthesis of (2.46) to be zero[21]. The continuity BC is implemented.

We defined an global expression dU (i.e. $\Delta\mu$) for the spin accumulation, make sure $dU = u1L - u2L$ in the left module and $dU = u1R - u2R$ in the right module. The global expressions are also calculated during the simulation.

The simulated results are shown inFigure 2.7. We can compare them to Valet and Fert's 1D results in Figure 2.5. It shows that the Multiphysics approach also gives us good results. Furthermore, the Multiphysics approach can enable us to include interface resistance into the

model, which has not been calculated by Valet and Fert in their original paper. If there is an interface resistance, there would be an additional term $\frac{r_s\sigma_s^2}{e^2}\cdot\frac{\partial\mu_s}{\partial x}$ inside the parenthesis of (2.45) and(2.46).

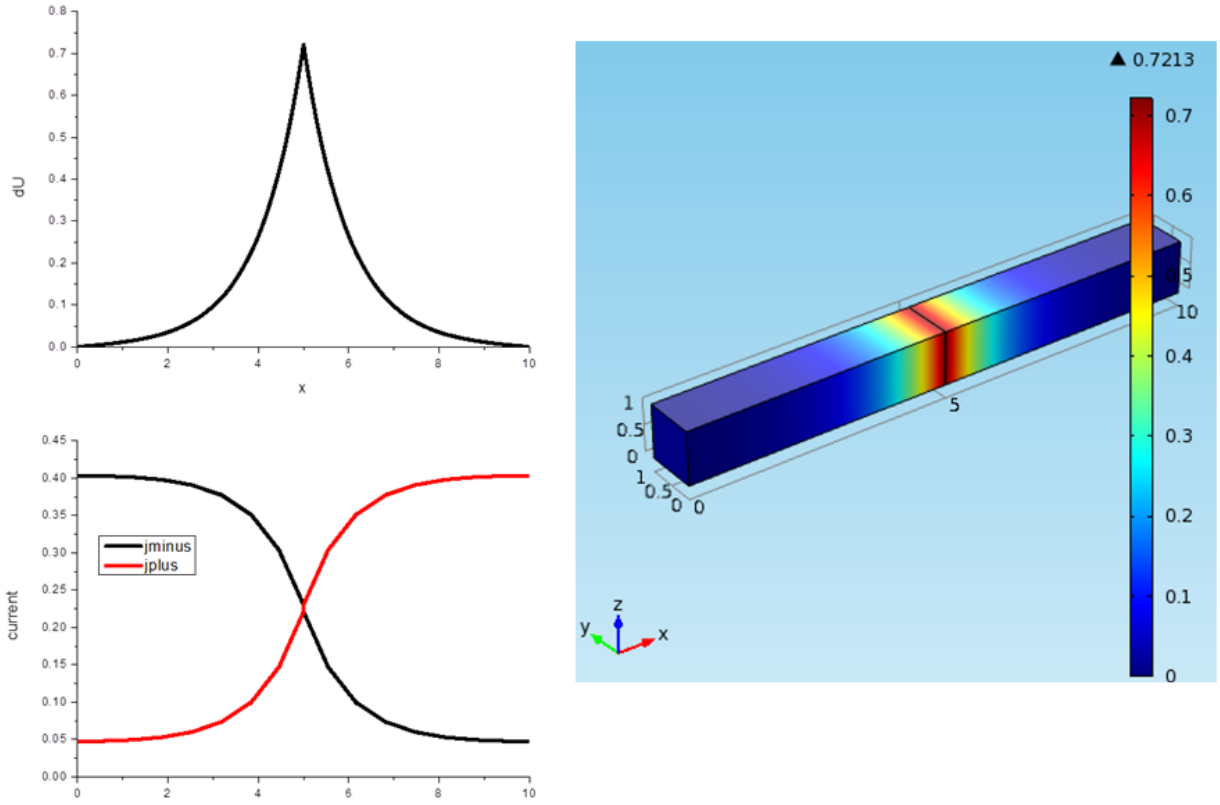

Figure 2.7. Multiphysics implementation of Valet-Fert model in 3D mode, *top left* shows the spin accumulation $\Delta\mu$;*bottom left* shows the current in majority (red) and minority (black) channel respectively; *right* is the 3D model in which the color shows the spin accumulation.

CHAPTER 3 DESIGNING MATERIAL FOR CURRENT-PERPENDICULAR-TO-PLANE GIANT MAGNETO-RESISTANCE APPLICATIONS

3.1 Materials needed for CPP-GMR

Much higher magnetoresistance (MR) ratios are needed for CPP GMR devices so that the signal from a CPP GMR read sensor will be easier to measure. Moreover, if we could make CPP GMR devices with very large MR, this might open the door for very low voltage spintronic logic circuits. There is, therefore, strong incentive to develop a material that shows as much difference in the conduction of two channels at the Fermi level as possible. The ideal case would be that the material has conduction band crossing at the Fermi level in one spin channeland has a band gap at the Fermi level in the other spin channel. This type of material is called a "half-metal" because it is a conductor in one spin channel and an insulator in the other[22].

Thus the search for half metals is of great importance in the Spintronics industry[23]. Although a large number of half metals have been discovered through first-principlescalculations [24-28], those discoveries appear to be by serendipity. There is, however, a rational approach to

the design of half-metallic hetero-structures through which one can not only design but also optimize the magnetization, the magnetic damping and the magnetic anisotropy of the material without sacrificing its half-metallic feature.

3.2 Extended Hückel Tight-Binding Theory

Before describing the method of finding half metals rationally, we need to elaborate on how to describe the interactions between atoms and electrons inside the crystals. There are many ways to represent the electron wave functions in a solid. We may represent them, for example, as an expansion in plane waves. This approach is most straightforward in the atomic potentials are relatively weak, but it has been extended to strongly interacting atomic potentials using the Projector Augmented Wave approach[29]. At the other extreme, we can expand the wave function as a linear combination of atomic orbitals (LCAO). When the latter approach is used with a minimal basis, it is often called the called the tight-binding (TB) method. Thus, the TB method is most useful for dealing with cases in which only the bands below and near the Fermi level are of interest.

Consider a lattice consisting of a periodic array of identical cells each having a number of atoms. Suppose the lattice vector of a certain unitcell is $\vec{R}$ and the position of a certain atom i within the unitcell is $\vec{b}_i$, in which i denotes the atom. Then the position of every atom in the crystal can be represented by the linear combination of $\vec{R}$ and $\vec{b}_i$. If the symmetry of the orbital is denoted by α, then we can define the atomic like orbital as

$$\phi_\alpha\left(\vec{r}-\vec{R}-\vec{b}_i\right) \text{ or } \left\langle \vec{r}\middle| i,\vec{R},\alpha \right\rangle \tag{2.1}$$

We can take advantage of the periodicity of the lattice by constructing linear combinations of the atomic orbitals (3.1)that satisfy Bloch's condition,

$$\psi_{i\alpha}\left(\vec{r},\vec{k}\right)=\frac{1}{\sqrt{N}}\sum_{\vec{R}} e^{i\vec{k}\cdot\vec{R}}\phi_\alpha\left(\vec{r}-\vec{R}-\vec{b}_i\right) \text{ or } \left|i,\alpha,\vec{k}\right\rangle=\frac{1}{\sqrt{N}}\sum_{\vec{R}} e^{i\vec{k}\cdot\vec{R}}\left|i,\vec{R},\alpha\right\rangle \tag{2.2}$$

Here $\vec{k}$ is a Bloch wave vector in the reciprocal space of the first Brillouin Zone. N is the total number of unit cells. Therefore, the Hamiltonian matrix element for the interaction between atom i's orbital α and atom j's orbital β can be written as

$$\begin{aligned} H_{i\alpha,j\beta}\left(\vec{k}\right) &= \frac{1}{N}\sum_{\vec{R}_m,\vec{R}_n} e^{i\vec{k}\left(\vec{R}_n-\vec{R}_m\right)} \int d\vec{r}^{\,3}\phi_{i\alpha}{}^{*}\left(\vec{r}-\vec{R}_m-\vec{b}_i\right) H\phi_{j\beta}\left(\vec{r}-\vec{R}_n-\vec{b}_i\right) \\ &= \sum_{\vec{R}} e^{i\vec{k}\cdot\vec{R}} \int d\vec{r}^{\,3}\phi_{i\alpha}{}^{*}\left(\vec{r}-\vec{b}_i\right) H\phi_{j\beta}\left(\vec{r}-\vec{R}-\vec{b}_i\right) \end{aligned} \tag{2.3}$$

Or in a simpler way using Dirac's notation by

$$H_{i\alpha,j\beta}\left(\vec{k}\right) = \left\langle i,\alpha,\vec{k}\left|H\right|j,\beta,\vec{k}\right\rangle = \sum_{\vec{R}} e^{i\vec{k}\cdot\vec{R}}\left\langle i,0,\alpha\left|H\right|j,\vec{R},\beta\right\rangle \tag{2.4}$$

In actual calculations, we use the Extended Hückel Tight Binding method (EHTB) instead of the traditional Slater-Koster method (SK)[30] because it can provide similar accurate and transferable approach with fewer number of parameters[31]. In EHTB,the basis set here is a linear combination of Slater type orbitals, typically of the double zeta Slater type orbital given for a single orbital by,

$$C_1 r^{n-1} e^{-\zeta_1 r} Y_{lm}\left(\theta,\varphi\right) + C_2 r^{n-1} e^{-\zeta_2 r} Y_{lm}\left(\theta,\varphi\right) \tag{2.5}$$

Here, $Y_{lm}\left(\theta,\varphi\right)$ is aspherical harmonic, and C_1 and C_2 as well as ζ_1 and ζ_2 are coefficients. Only one of C_1 and C_2 is independent because of the normalization condition.The overlap between two orbitals at different sites may not be zero, i.e. the basis set formed from those orbitals are non-orthogonal.

Similarly to the SK approach, we construct the basis vectors with Bloch sum as,

$$\left|i,\alpha,\vec{k}\right\rangle = \frac{1}{\sqrt{N}}\sum_{\vec{R}} e^{i\vec{k}\cdot\vec{R}}\left|i,\vec{R},\alpha,\right\rangle \tag{2.6}$$

The overlap matrix is not a unit matrix anymore because of the non-orthogonal basis set. For the overlap between atom i's orbital α and atom j's orbital β, i.e. the matrix element $S_{i\alpha,j\beta} = \left\langle i,\alpha,\vec{k} \middle| j,\beta,\vec{k} \right\rangle$ can be calculated using the same method as we did to the Hamiltonian matrix element.

$$\begin{aligned} S_{i\alpha,j\beta} &= \frac{1}{N}\sum_{\vec{R}_m,\vec{R}_n} e^{i\vec{k}\left(\vec{R}_n-\vec{R}_m\right)} \int d\vec{r}^3 \phi_{i\alpha}{}^* \left(\vec{r}-\vec{R}_m-\vec{b}_i\right)\ \phi_{j\beta}\left(\vec{r}-\vec{R}_n-\vec{b}_i\right) \\ &= \sum_{\vec{R}} e^{i\vec{k}\cdot\vec{R}} \int d\vec{r}^3 \phi_{i\alpha}{}^* \left(\vec{r}-\vec{b}_i\right)\ \phi_{j\beta}\left(\vec{r}-\vec{R}-\vec{b}_i\right) \end{aligned} \tag{2.7}$$

or

$$S_{i\alpha,j\beta}\left(\vec{k}\right) = \left\langle i,\alpha,\vec{k} \middle| j,\beta,\vec{k} \right\rangle = \sum_{\vec{R}} e^{i\vec{k}\cdot\vec{R}} \left\langle i,0,\alpha \middle| j,\vec{R},\beta \right\rangle = \sum_{\vec{R}} e^{i\vec{k}\cdot\vec{R}} s_{i\alpha,j\beta}\left(\vec{R}\right) \tag{2.8}$$

in which we used $s_{i\alpha,j\beta}\left(\vec{R}\right) = \left\langle i,0,\alpha \middle| j,\vec{R},\beta \right\rangle$ for further simplification. With a similar notation $h_{i\alpha,j\beta}\left(\vec{R}\right) = \left\langle i,0,\alpha \middle| H \middle| j,\vec{R},\beta \right\rangle$, we can also get a simpler form of Hamiltonian

$$H_{i\alpha,j\beta}\left(\vec{k}\right) = \sum_{\vec{R}} e^{i\vec{k}\cdot\vec{R}} h_{i\alpha,j\beta}\left(\vec{R}\right) \tag{2.9}$$

Since the basis set of the $\vec{k}$ vector space $\left\{\left| i,\alpha,\vec{k} \right\rangle\right\}$ is orthogonal, the Hamiltonian and overlap matrix is now block-diagonalized in the $\vec{k}$ vector space, hence we can study the two matrices for given $\vec{k}$ first and then generalize to any other $\vec{k}$ point. Furthermore the two matrices are in fact counter-dependent following the relation below in the EHTB paradigm[32].

$$H_{i\alpha,j\beta}\left(\vec{k}\right) = \frac{1}{2} K \left(h^0_{i\alpha} + h^0_{j\beta}\right) S_{i\alpha,j\beta}\left(\vec{k}\right) \tag{2.10}$$

where K is a constant that may depends on the actual atom type, $h^0_{i\alpha}$ and $h^0_{j\beta}$ are the onsite energies. The Schrodinger equation will have non-trivial solution only if the determinant

$|H - ES|$ is zero. Therefore one can obtain a series of the eigenvalues for any given $\vec{k}$ which will compose the energy bandsby calculating the generalized eigenvalues for the Hamiltonian and overlap matrices.

In fact, the calculation of generalized eigenvalues is essential because actually we fit the calculated bands to 'real' bands which may be either from first principle calculation or from experimental measurements. The accuracy of an EHTB description is evaluated by how well it restores the bands structure. There are four independent fitting parameters for any given double zeta orbital, the onsite energies ($h_{i\alpha}^0$ and $h_{j\beta}^0$), theradical decay factor (ζ_1 and ζ_2) as well as one of the two coefficients C_1 and C_2 in the orbital function (3.5).

The fitted parameters such as the onsite energies and the radical decay factors provide us with chemical and physical insight. Upon which the rational approach is based.

3.3 The Gap Theorem

In the following we consider a 1D atomic system with two sub lattices, A and B, as shown in Figure 3.1.We assume the orbitals for each site share the same onsite energy and theonsite energies of the orbitals for A sites and B sites are E_A and E_B respectively. If the A orbitals only interact with the B orbitals and vice versa, the 1D atomic chain can be represented by the tight-binding Hamiltonian,

$$\hat{H} = \sum_{\text{n odd}} E_A \hat{c}_n^{\dagger} \hat{c}_n + \sum_{\text{n even}} E_B \hat{c}_n^{\dagger} \hat{c}_n + \sum_{\text{n}} \omega \left(\hat{c}_n^{\dagger} \hat{c}_{n+1} + \hat{c}_n \hat{c}_{n+1}^{\dagger} \right) \tag{2.11}$$

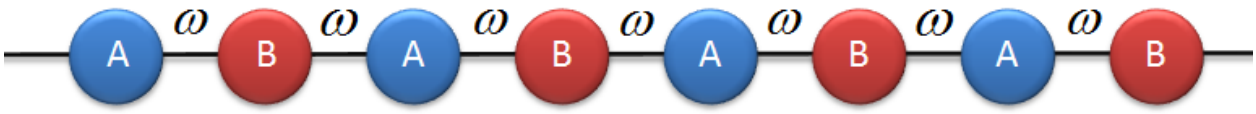

Figure 3.1.1D atomic system with two sub lattices.type A atom sits on one sub-lattice and type B atom sits on the other. There is only nearest neighbor interaction and the interaction is represented by the hopping parameter ω.

In the equation(3.11) the hopping parameter ω describes the interactions between neighboring atoms A and B. The density of states $n(E)$ can be easily calculated and is shown in equation(3.12) in which $x_A = (E - E_A)/\omega$ and $x_B = (E - E_B)/\omega$.

$$n(E) = \frac{1}{\omega\pi} \operatorname{Im}\left[\frac{x_A + x_B}{\sqrt{x_A^{\,2} x_B^{\,2} - 4 x_A^{\,2} x_B}} \right] \tag{2.12}$$

When $(E - E_A)\cdot(E - E_B) < 0$, $n(E)$ vanishes because the term $\dfrac{x_A + x_B}{\sqrt{x_A^{\,2} x_B^{\,2} - 4 x_A^{\,2} x_B}}$ becomes real. In other words, a gap is created extending from E_A to E_B.The gap theorem can be

extended to three dimensional cases if the requirementthat type A atoms only interact with type B atomsremains satisfied. If one assume nearest neighbor interaction only, the gap theorem will still be valid.

3.4 Half-Heusler Alloys

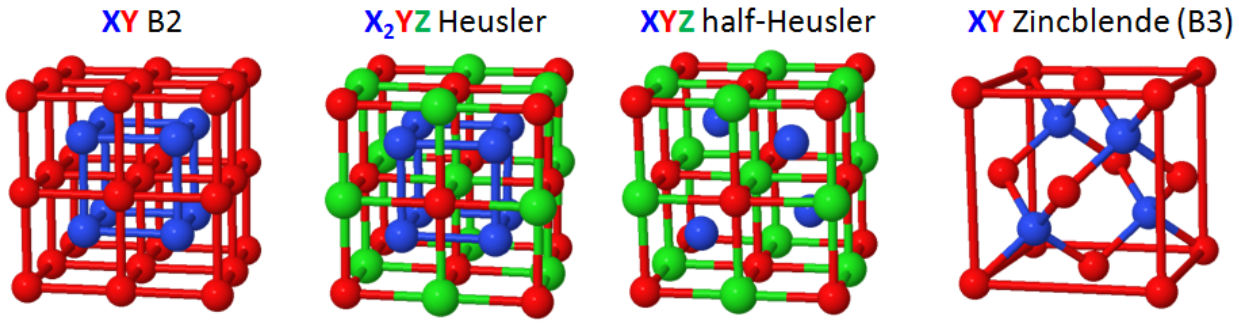

Figure 3.2.Illustrations of B2, Heusler, Half-Heusler and Zincblende crystal structure, *Left* is the B2 structure; *followed by* the Heusler structure and the half-Heusler structure *in the middle*;*right* is the Zincblende structure, also known as the B3 structure.

The structure of B2 and B3 (see Figure 3.2) are of interest on the application of gap theorem.Because the periodic arraying of atoms in them shows a behavior of alternating atoms, the gap theorem predicts that there will be gaps created from the onsite energy of X atom to the onsite energy of B atom if only nearest neighbor interaction existed. Another thing we need to bear in mind is that there is usually more than one orbital contributing to the DOS around Fermi level.

The half metalicity of NiMnSb was discovered by de Groot et al. [22] in 1983 through first principle calculations and proved experimentally byHanssen et al. in 1990 [33, 34]. We will use this material as example to explain the physics behind the half metalicityand propose the rational way of designing new half-metals in the following. By performing EHTB fitting to the first principle calculations, we obtain the TB description of NiMnSb with the half-Heusler structure. Interactions up to next-next-nearest neighbor are included. Fitting is done for one band

above the Fermi level (0 eV) and all the bands below Fermi level. We can see that the fitting is good in that energy range (see Figure 3.3).

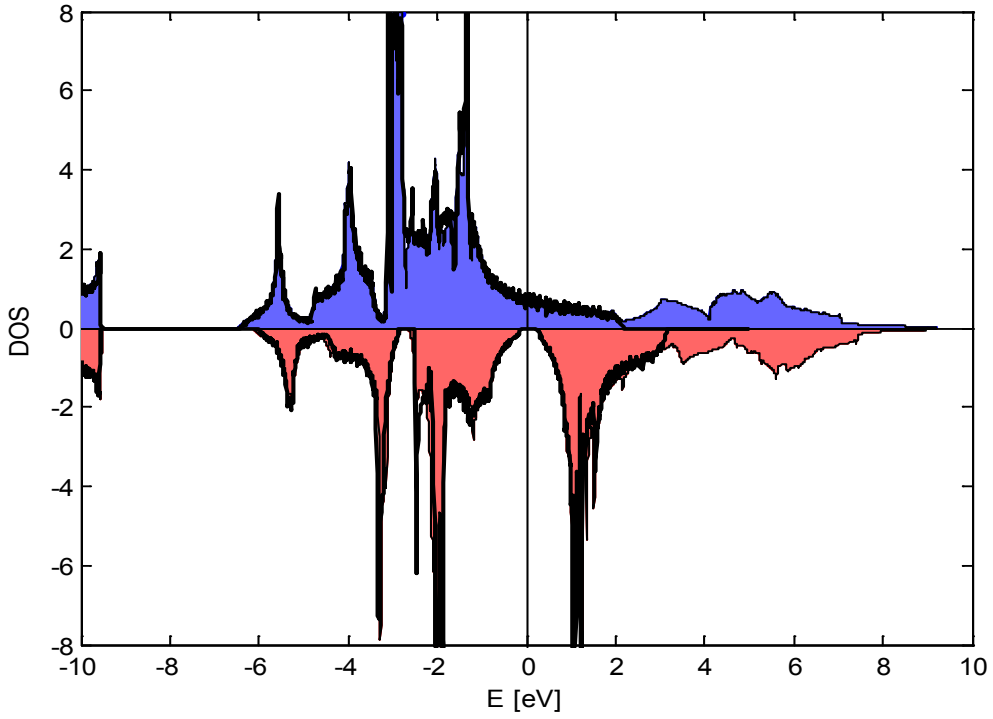

Figure 3.3. Density of states (DOS) of NiMnSb with the half-Heusler structure. The filled color area shows the DOS calculated by first principle approach (VASP). The black profile line shows the DOS calculated by the TB parameters obtained by fitting. Blue color is for majority spin channel and red is for minority.

We did another first principle calculation by removing the Sb atoms and creating an arbitrary Zinc-blend structure NiMn. We found that the magnetic moments are almost unaffected by the "removal" of Sb. Then we did the density of states (DOS) calculation for Zinc-blend NiMn with different interaction radius using the same EHTB parameter set obtained before for half-Heusler NiMnSb. The DOS with nearest neighbor interactions and next-nearest neighbor interactions are shown in Figure 3.4.

Table 2.Magnetic moments of half Heulser NiMnSb and Zinc-blend NiMn.

	half-Heulser NiMnSb			Zinc-blendNiMn	
	Ni	Mn	Sb	Ni	Mn
Majority electron	5.1	5.4	1.5	5.2	5.6
Minority electron	4.9	1.6	1.5	4.8	1.4

Values obtained from VASP calculation.

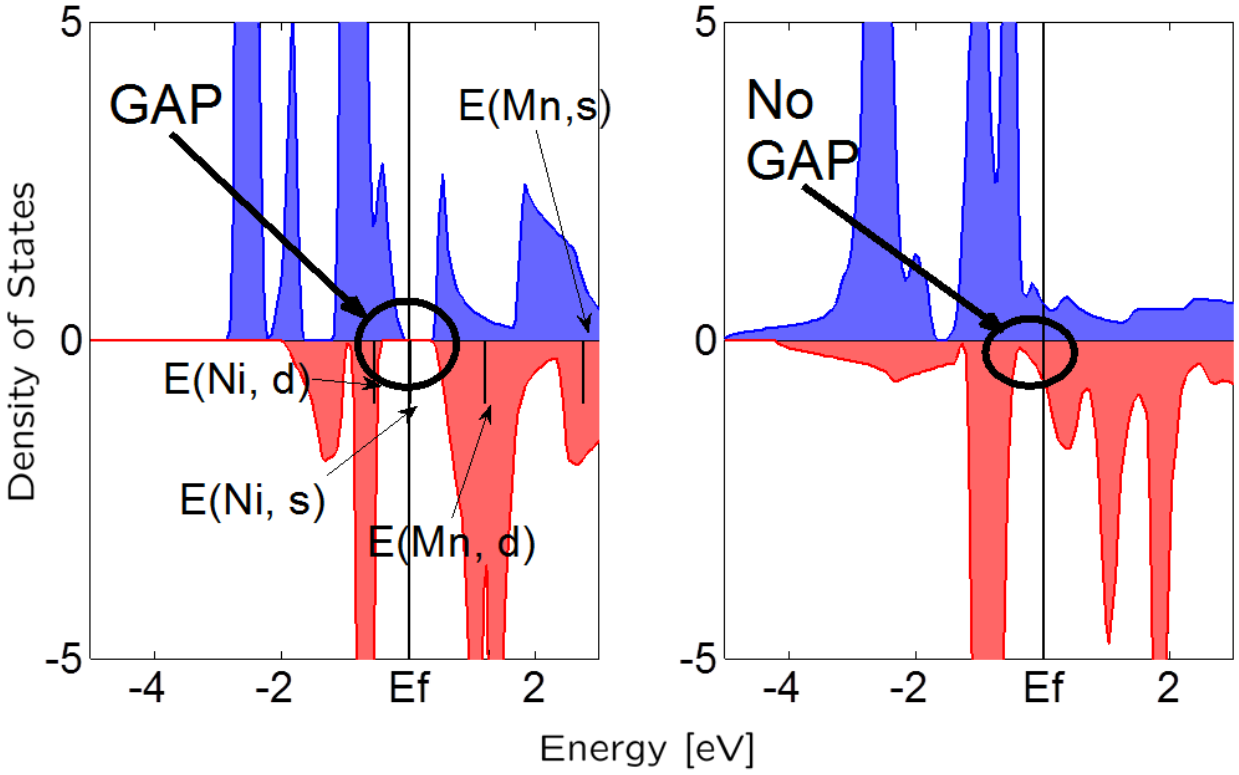

Figure 3.4. DOS of Zinc-blend NiMn with nearest neighbor interactions (*left*) and next-nearest neighbor interactions (*right*)

From the DOS, we can see that the gaps are created around Fermi level in both spin channels for the case with nearest neighbor interactions, which is predicted by the gap theorem. However both of the two gaps are filled by next-nearest neighbor interactions. For comparison we did DOS calculation for half-Heusler NiMnSb with nearest neighbor interactions and next-

nearest neighbor interactions (see Figure 3.5). We can see that the gap is still there even when the gap-destructive next-nearest neighbor interactions are included. So we can conclude that the non magneticSb atom act like a “screener ” here that can screen the unwanted gap-destructive interactions hence create the half-metalicity of NiMnSb.

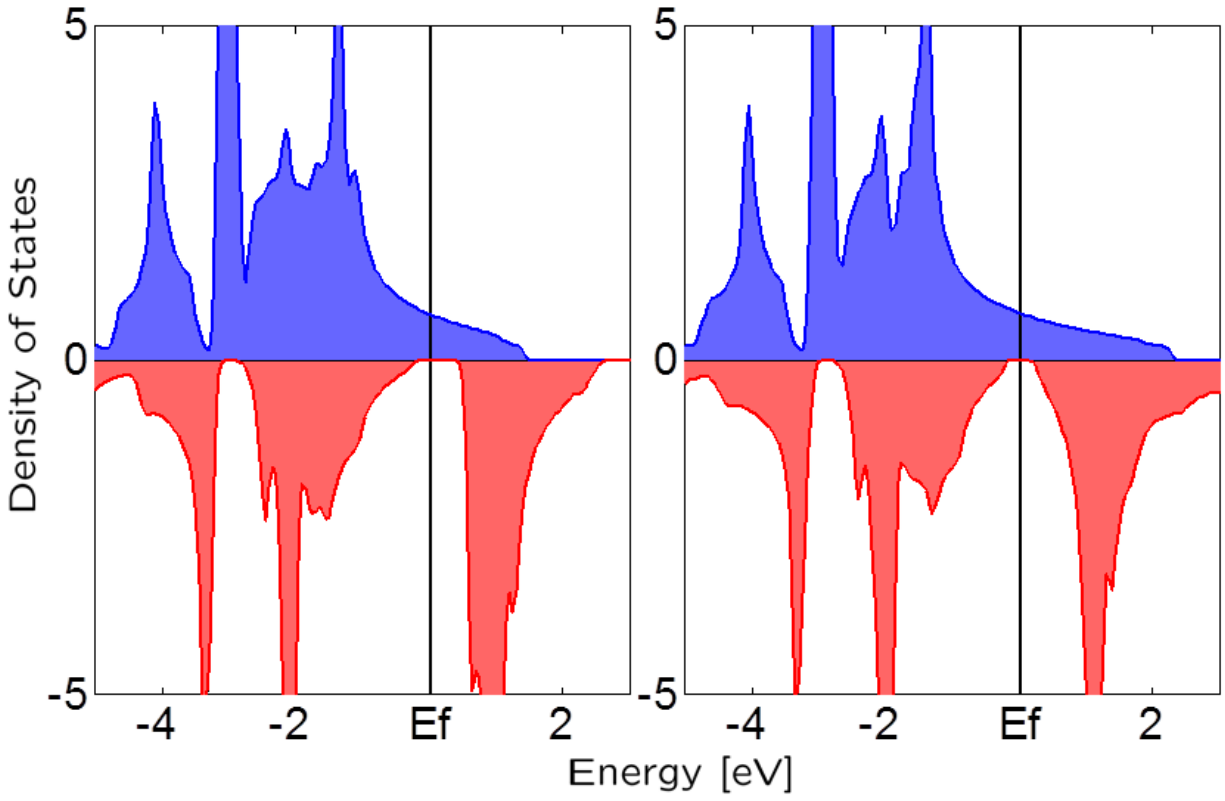

Figure 3.5.DOS of half-Heusler NiMnSb with nearest neighbor interactions (*left*) and next-nearest neighbor interactions (*right*). We can see that the next-nearest neighbor interactions shrink the size of the gap near the Fermi level in the minority spin channel. There is not much difference between the DOS with next-nearest neighbor interactions and with long range interactions (next-next-nearest neighbor interactions)

We found some other half metals such as Co_2MnSi, Fe_2TiSi, and $Co_2MnSiFe_2TiSi$

using the same physics explained above. The DOS obtained from first principle calculations of these materials and relevant materials are shown in Figure 3.6[35].

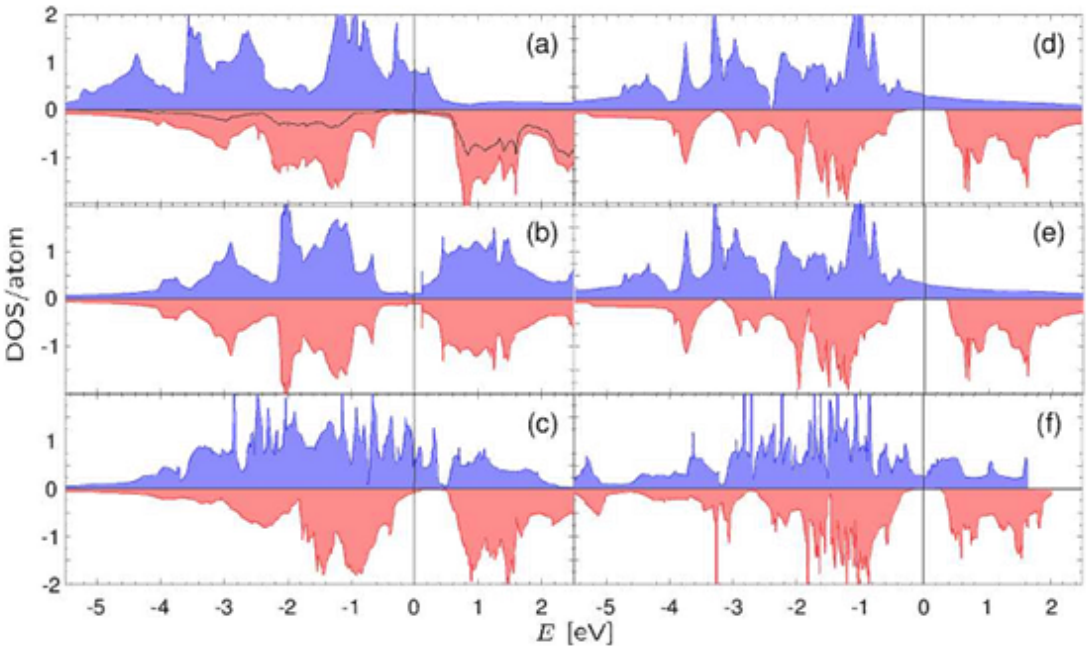

Figure 3.6. DOS for (*a*) CoMn, (*b*) FeTi, (*c*) CoMnFeTi, (*d*) Co_2MnSi, (*e*) Fe_2TiSi and (*f*) $Co_2MnSiFe_2TiSi$. The blue color is for the majority spin channel and the red color is for the minority spin channel. The additional black line in subfigure (a) shows the Mn DOS.

CHAPTER 4 TUNNELING IN THE MAGNETIC TUNNEL JUNCTIONS

4.1 Introduction

Magnetic tunnel junctions (MTJ) consist of two ferromagnetic materials separated by an insulating layer that is sufficiently thin that electrons can pass through it by quantum tunneling. The conductance of the junction depends on the relative orientation of magnetizations of the two magnetic layers which can be altered by an external magnetic field. Therefore MTJs can serve as magnetic field detectors in a manner similar to CPP-GMR spin valves.

Tunneling Magnetoresistance (TMR) was first discovered by MichelJullièrein a Fe/Ge/Co-junction. He observed a 14% magnetoresistance (MR) at 4.2K[36]. TMR did not gain much attention until significant MR was observed at room temperature in the mid-1990s [37, 38]. In 2001, WilliamButleret al.predicted thata large MRratio (several hundred percent)that increases with barrier thickness should be observed in well crystallized Fe(001)/MgO(001)/Fe(001) junctionsbased on the symmetry filtering effect[39]. Since then, MTJs with large room temperature MR ratio based on these principles have been fabricatedby many experimental groups [40-43].The large MR has made this type of MTJ popular in the spintronic industry.

4.2 Tunneling Theory

The semi-classical approach that we used to describe CPP-GMR is not adequate to describe the conductance in the quantum tunneling process. We use instead a formalism developed by Landauer and Büttiker [44-46]. This approach, which calculates the conductance from the probability for an electron to be transmitted by the insulating "barrier" has been used widely [47-49].

4.2.1 Landauer-Büttiker formalism

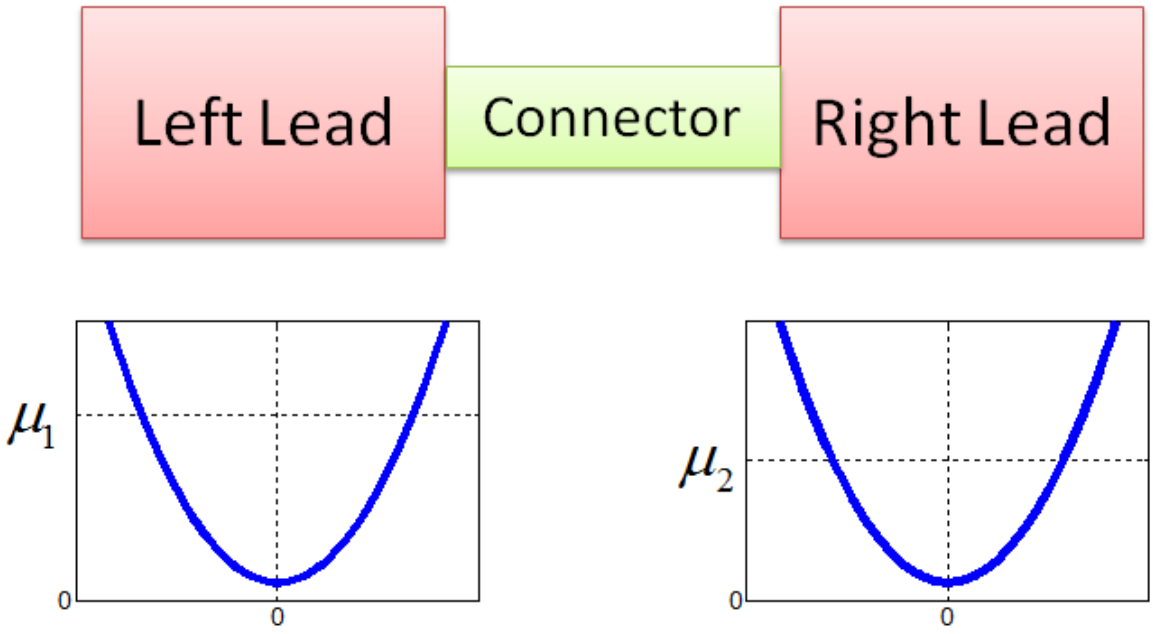

Figure 4.1.Two semi-infinite leads connected by a center connector. The band diagrams for each lead are shown schematically using free electron bands. μ_1 and μ_2 are the electrochemical potential for the left and right lead respectively. In general the leads may have arbitrary band structures.

To describe quantum transport in mesoscopic systems, one may start from an idealized system of two semi-infinite leads connected by a center connector (see

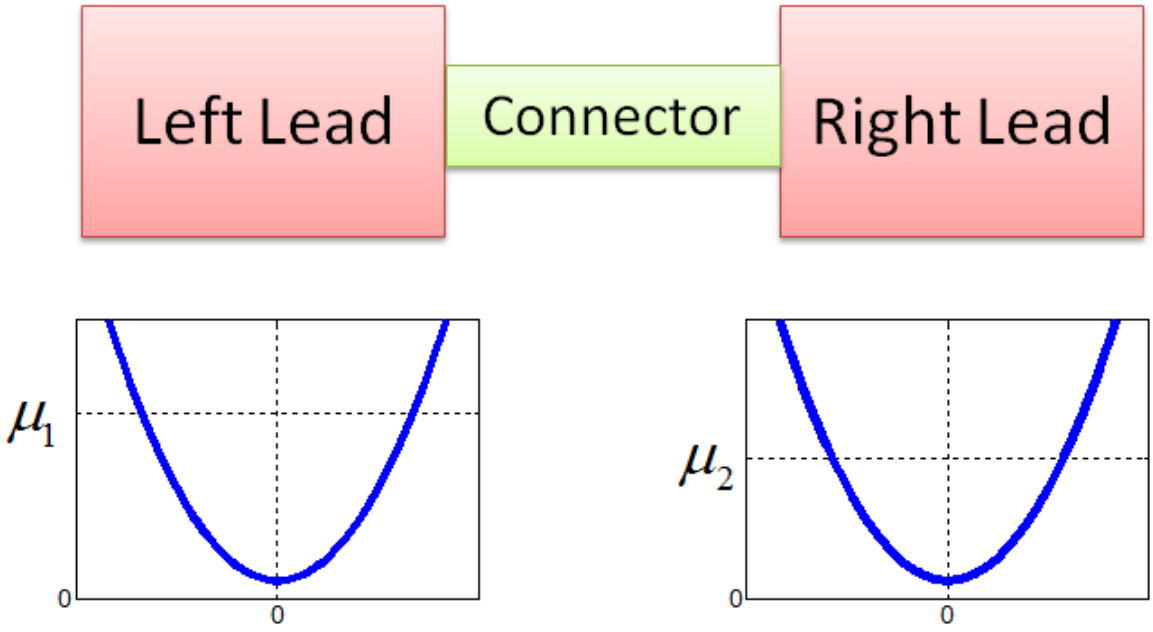

Figure4.1).The total current flowing through the leads is given below in the Landauer-Büttiker formalism

$$I_l = \frac{-e}{h}\int dE\overline{T}_{lr}(E)\left[f_l(E) - f_r(E)\right] \tag{3.1}$$

where l and r denotes the left and right lead, $f_l(E)$ is the Fermi-Dirac distribution for the left lead which is assumed to be a reservoir at thermal equilibrium, $f_r(E)$ is the Fermi-Dirac distribution for lead q, $\overline{T}_{lr}(E)$ is the transmission for an electron at energy E to propagate from leftto the right. It can be further linearized if the transmission function $\overline{T}_{lr}(E)$ is approximately constant in the transmission energy window (from μ_l to μ_r).

$$I_l = \frac{e}{h}\overline{T}_{lr}\left(E_f\right)\left(\mu_l - \mu_r\right) \tag{3.2}$$

where E_f is the energy at Fermi level[46, 50-54].

For the center connector, we label the wave amplitude for the i^{th} incoming and outgoing wave mode to be a_i and b_i respectively. So we can define the S matrix as,

$$\begin{Bmatrix} b_1 \\ \vdots \\ b_n \end{Bmatrix} = \begin{pmatrix} s_{11} & \cdots & s_{1n} \\ \vdots & \ddots & \vdots \\ s_{n1} & \cdots & s_{nn} \end{pmatrix} \begin{Bmatrix} a_1 \\ \vdots \\ a_n \end{Bmatrix}, \tag{3.3}$$

where n is the total number of transverse modes in the leads. The transmissionconsists of the ingress of a certain incoming wave into the center connector and the egress of another outgoing wave from the center connector. Therefore the transmission probability is obtained by taking the squared magnitude of the corresponding element of the S matrix. Now the transmission function $\overline{T}_{lr}\left(E\right)$ from left to right can be expressed as the sum of all possible transmission probabilities[54],

$$\overline{T}_{lr} = \sum_{\{m \text{ mode in the left lead}\}} \sum_{\{n \text{ mode in the right lead}\}} T_{nm} \tag{3.4}$$

The transmission probability can be solveddirectly from the Schrödinger equation for simple cases such as a1D potential barrier[55], however the easier approach of Green's function formalism is used more frequently in the study of MTJs[56].

4.2.2 Green's function

The Green's function, a useful tool for dealing with an inhomogeneous system, is defined by

$$\hat{L}G(\vec{r},\vec{r}') = \delta(\vec{r}-\vec{r}') \tag{3.5}$$

where $\hat{L}$ is an arbitrary linear operator, $\vec{r}$ is a vector in a Euclidean space Ω, δ is the Dirac delta function. Therefore the solution to equation $\hat{L}\phi = f$ is $\phi(\vec{r}) = \int G(\vec{r},\vec{r}')f(\vec{r}')d\Omega$.

For quantum physics, the Schrödinger equation is

$$\left[E - \hat{H}\right]\psi = 0 \tag{3.6}$$

The corresponding equation that defines the Green's function is given by

$$\left[E - \hat{H}(\vec{x})\right]G(\vec{x},\vec{x}',E) = \delta(\vec{x}-\vec{x}') \tag{3.7}$$

We use a notation in which the vector $\vec{x}'$ represents both the position $\vec{r}$ and spin, *s*. The Green's function is singular at the eigenvalues of the Schrödinger equation. The singularities can be treated by adding a small imaginary part to the energy. If this small imaginary part is positive, the Green's function is a causal retarded Green's function meaning that temporally effect follows the perturbation that causes it. If the small imaginary part is negative, the Green's function is an advanced Green function meaning that response temporally precedes the cause. For the case of a particle moving in a constant potential, one can see that the retarded Green's function, corresponds to an outgoing wave from position $\vec{r}'$ while the advanced Green's function, corresponds to an incoming wave to position $\vec{r}'$. Formally the retarded and advanced Green's functions are given by.

$$\begin{aligned} G^R &= \left[E - H + i\eta\right]^{-1} \qquad \eta \to 0^+ \\ G^A &= \left[E - H - i\eta\right]^{-1} \end{aligned} \tag{3.8}$$

4.3 Implementation and results

4.3.1 One dimensional model

A one dimensional infinite atomic chain is the simplest model one can think of for an infinite transport system. Though it is highly simplified, it allows for clear illustration of the concepts and is not difficult to extend to the more complicated heterostructures that comprise real MTJs. Any three dimensional crystal can be divided into a series of principle layers (PL), defined as the smallest group of atomic layers such that each PL only interacts with its nearest neighbor. Then the chain of PLs can be transformed into a one dimensional chain by Fourier transformation based on the periodicity in the plane perpendicular to the transport direction[57].

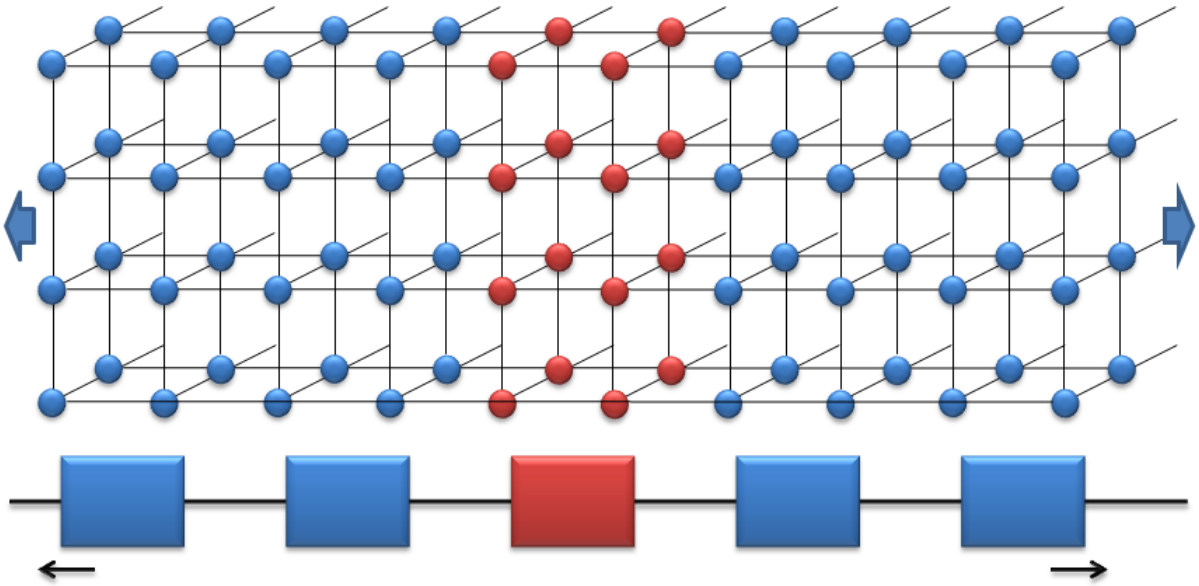

Figure 4.2. From 3D to 1D by choosing principle layers (2 atomic layers per principle layer in the figure) and Fourier transform.

In the Figure 4.2, the red atoms form the center connector and the blue atoms comprise the semi-infinite leads on both sides of the center connector. Assuming nearest and next-nearest neighbor interaction, each PL would contain only two parallel atomic layers for most common crystalline heterostructures.

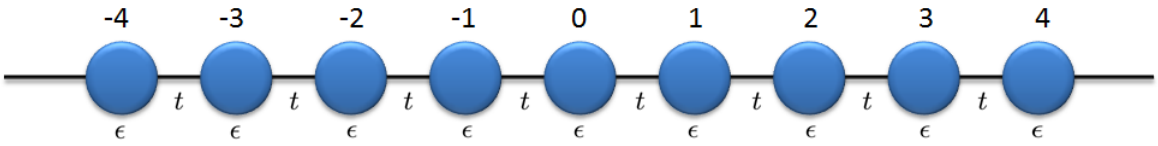

Figure 4.3.1D infinite atomic chain. Onsite energy for each atom is ε while the interaction between nearest atoms is t. Only nearest-neighbor interaction is included.

Consider the one dimensional atomic chain illustrated in Figure 4.3. We label the atoms for convenience. (The labels do not have special significance here. Any atom site can be chosenas"site 0"). The right lead corresponds to a semi-infinite chain of atoms with positive index, and the left lead corresponds to the ones with negative index. All of the atoms are equivalent by assumption. We begin by calculating the retarded Green's function of a semi-infinite chain, starting from the definition(4.8). Let $\omega = E + i\eta$, then, using the explicit form of our (effectively) one dimensional Hamiltonian, we write (4.8) as

$$\begin{bmatrix} \omega - H_{00} & H_{01} & 0 & 0 & \cdots \\ H_{01}^{+} & \omega - H_{00} & H_{01} & 0 & \cdots \\ 0 & H_{01}^{+} & \omega - H_{00} & H_{01} & \cdots \\ 0 & 0 & H_{01}^{+} & \omega - H_{00} & \cdots \\ \vdots & \vdots & \vdots & \vdots & \ddots \end{bmatrix} \begin{bmatrix} G_{00} & G_{01} & G_{02} & G_{03} & \cdots \\ G_{10} & G_{11} & G_{12} & G_{13} & \cdots \\ G_{20} & G_{21} & G_{22} & G_{23} & \cdots \\ G_{30} & G_{31} & G_{32} & G_{33} & \cdots \\ \vdots & \vdots & \vdots & \vdots & \ddots \end{bmatrix} = I \quad . \qquad (3.9)$$

Note that each element in the matrix (4.9) may itself represent a finite matrix.

Multiplying successive rows of $[\omega - H]$ times the first column of *G*, we have,

$$\begin{aligned}
(\omega - H_{00})G_{00} &= I + H_{01}G_{10} \\
(\omega - H_{00})G_{10} &= H_{01}^{+}G_{00} + H_{01}G_{20} \\
&\vdots \\
(\omega - H_{00})G_{n0} &= H_{01}^{+}G_{(n-1)0} + H_{01}G_{(n+1)0}
\end{aligned} \tag{3.10}$$

from which we have

$$G_{n0} = (\omega - H_{00})^{-1}\left(H_{01}^{+}G_{(n-1)0} + H_{01}G_{(n+1)0}\right) \qquad \text{n} \geq 1 \tag{3.11}$$

Inserting(4.11) back into (4.10), we have

$$\begin{aligned}
&\left[\omega - H_{00} - H_{01}(\omega - H_{00})^{-1}H_{01}^{+}\right]G_{00} = I + H_{01}(\omega - H_{00})^{-1}H_{01}G_{20} \\
&\left[\omega - H_{00} - H_{01}(\omega - H_{00})^{-1}H_{01}^{+} - H_{01}^{+}(\omega - H_{00})^{-1}H_{01}\right]G_{n0} \\
&\qquad = H_{01}^{+}(\omega - H_{00})^{-1}H_{01}^{+}G_{(n-2)0} + H_{01}(\omega - H_{00})^{-1}H_{01}G_{(n+2)0} \qquad (n \geq 2)
\end{aligned} \tag{3.12}$$

Following this procedure, we can see that G_{n0} terms for all odd *n* can be made to disappear. Equations(4.12) can be rewritten as,

$$\begin{aligned}
(\omega - \varepsilon_{1s})G_{00} &= I + \alpha_1 G_{20} \\
(\omega - \varepsilon_1)G_{n0} &= \beta_1 G_{(n-2)0} + \alpha_1 G_{(n+2)0} \qquad\qquad n = 2N,\ N \geq 1 \\
(\omega - \varepsilon_1)G_{nn} &= I + \beta_1 G_{(n-2)n} + \alpha_1 G_{(n+2)n}
\end{aligned} \tag{3.13}$$

where

$$\begin{aligned}
\alpha_1 &= H_{01}(\omega - H_{00})^{-1}H_{01} \\
\beta_1 &= H_{01}^{+}(\omega - H_{00})^{-1}H_{01}^{+} \\
\varepsilon_{1s} &= H_{00} + H_{01}(\omega - H_{00})^{-1}H_{01}^{+} \\
\varepsilon_1 &= H_{00} + H_{01}(\omega - H_{00})^{-1}H_{01}^{+} + H_{01}^{+}(\omega - H_{00})^{-1}H_{01}.
\end{aligned} \tag{3.14}$$

Comparing equation (4.13)to equation(4.10), we can see that (4.14)actually define an effective Hamiltonian for a chain of effective atoms with twice the lattice constant of the original one. Each effective atom contains the nearest neighbor interactions inside itself. Thus we can treat the "effective" atomic chain as we did to the original atomic chain and get a new effective atomic chain with four times the original lattice constant. Repeating the procedure i times, we have the iterative sequence below which defines an effective Hamiltonian for a chain of lattice constant 2^i times with the nearest neighbor interactions α_i and β_i .The zeroth-order Hamiltonian matrix elements are ε_i and ε_i' [58].

$$\begin{aligned}
\alpha_i &= \alpha_{i-1}\left(\omega-\varepsilon_{i-1}\right)^{-1}\alpha_{i-1}\\
\beta_i &= \beta_{i-1}\left(\omega-\varepsilon_{i-1}\right)^{-1}\beta_{i-1}\\
\varepsilon_i &= \varepsilon_{i-1}+\alpha_{i-1}\left(\omega-\varepsilon_{i-1}\right)^{-1}\beta_{i-1}+\beta_{i-1}\left(\omega-\varepsilon_{i-1}\right)^{-1}\alpha_{i-1}\\
\varepsilon_i' &= \varepsilon_{i-1}'+\alpha_{i-1}\left(\omega-\varepsilon_{i-1}\right)^{-1}\beta_{i-1}
\end{aligned} \tag{3.15}$$

and the Green's function becomes

$$\begin{aligned}
\left(\omega-\varepsilon_i'\right)G_{00} &= I+\alpha_i G_{\left(2^i n\right)0}\\
\left(\omega-\varepsilon_i\right)G_{\left(2^i n\right)0} &= \beta_i G_{2^i(n-2),0}+\alpha_i G_{2^i(n+2),0} \qquad n\geq 1
\end{aligned} \tag{3.16}$$

The interaction terms, α_i and β_i, decay rapidly because the distance increases exponentially with the number of iterations. Therefore we can approximate (4.16) to

$$\begin{aligned}
\left(\omega-\varepsilon_i'\right)G_{00} &\simeq I\\
\left(\omega-\varepsilon_i\right)G_{\left(2^i n\right)\left(2^i n\right)} &\simeq I \qquad n\geq 1
\end{aligned} \tag{3.17}$$

The Green's function for the surface of lead (G_{00}), the Green's function for the bulk layer ($G_b = \lim_{n\to\infty} G_{nn}$), the Green's function for the dual surface, i.e. the center connector or the atom at site 0 , can now be given below respectively,

$$\begin{aligned} G_{00} &= \left(\omega - \varepsilon_i'\right)^{-1} \\ G_b &= \left(\omega - \varepsilon_i\right)^{-1} \\ \bar{G}_{00} &= \left(\omega - \bar{\varepsilon}_i'\right)^{-1} \end{aligned} \tag{3.18}$$

where $\bar{\varepsilon}_{i+1}' = \bar{\varepsilon}_i' + \beta_i \left(\omega - \varepsilon_i\right)^{-1} \alpha_i$. The iteration process is illustrated in the program flow chart below for a programmer's convenience[59].

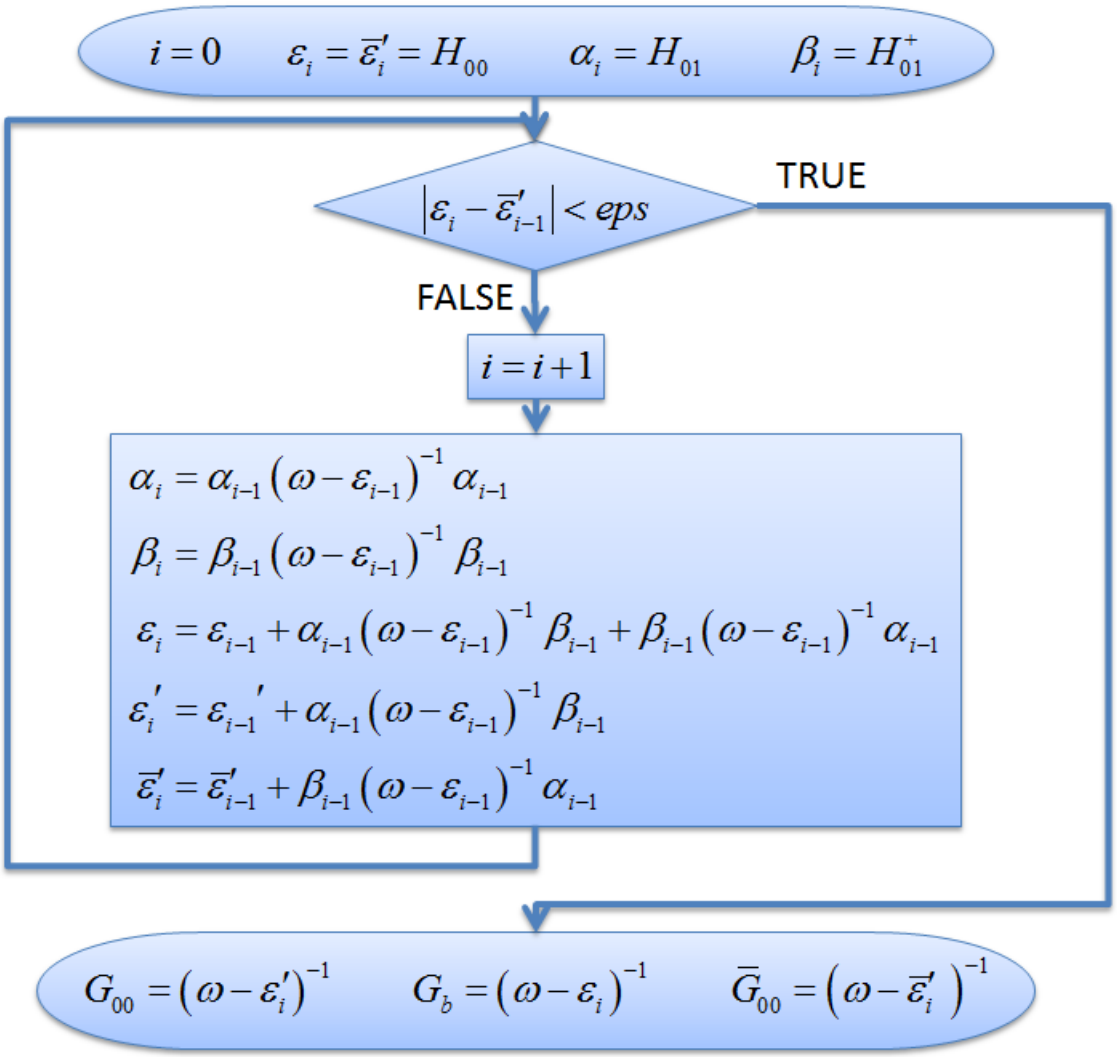

Figure 4.4.A highly convergent scheme for the calculation of Green's function.The number eps is a very small positive one chosen by the programmer.

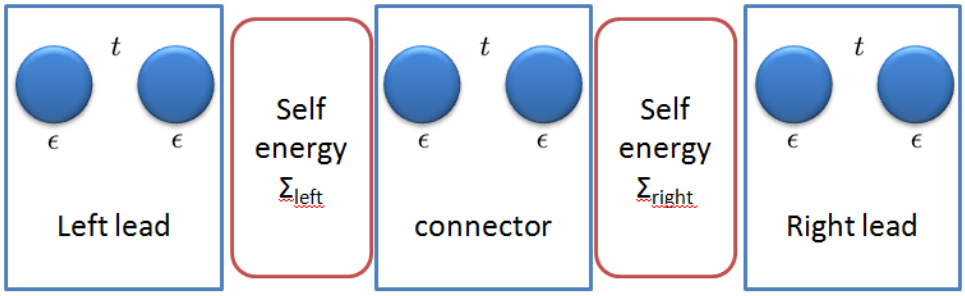

Figure 4.5.The equivalent six-atomsystem for the infinite 1D atomic chain with nearest neighbor interaction.

The infinite 1D atomic chain in Figure 4.3 can be transformed to a chain with only six atoms by the introduction of self energy terms, as shown inFigure 4.5. The Hamiltonian and overlap matrices with the orthogonal basiswill be two 6×6 matrices shown in (4.19).

$$H=\begin{pmatrix} \varepsilon & t & 0 & 0 & 0 & 0 \\ t & \varepsilon & t & 0 & 0 & 0 \\ 0 & t & \varepsilon & t & 0 & 0 \\ 0 & 0 & t & \varepsilon & t & 0 \\ 0 & 0 & 0 & t & \varepsilon & t \\ 0 & 0 & 0 & 0 & t & \varepsilon \end{pmatrix} \qquad S=\begin{pmatrix} 1 & 0 & 0 & 0 & 0 & 0 \\ 0 & 1 & 0 & 0 & 0 & 0 \\ 0 & 0 & 1 & 0 & 0 & 0 \\ 0 & 0 & 0 & 1 & 0 & 0 \\ 0 & 0 & 0 & 0 & 1 & 0 \\ 0 & 0 & 0 & 0 & 0 & 1 \end{pmatrix} \tag{3.19}$$

The Hamiltonian can be break into blocks accordingly, we have the matrix for the left lead $H_L=\begin{pmatrix} \varepsilon & t \\ t & \varepsilon \end{pmatrix}$, the effectfor left lead on the center connector $w_{LC}=\begin{pmatrix} 0 & 0 \\ t & 0 \end{pmatrix}$, the center connector $H_C=\begin{pmatrix} \varepsilon & t \\ t & \varepsilon \end{pmatrix}$, the effect for the center connector on the right lead $w_{CR}=\begin{pmatrix} 0 & t \\ 0 & 0 \end{pmatrix}$ and the right lead $H_R=\begin{pmatrix} \varepsilon & t \\ t & \varepsilon \end{pmatrix}$. Same dividing rules will be applied to the overlap matrix too.

Following the recursive scheme described in Figure 4.4, the Green's function for the left lead, for the right lead and for the center connector can be obtained accordingly. The self

energyfor the left lead exert on the center connecter and for the right lead exert on the center connecter will be[54],

$$\begin{aligned}\Sigma_L &= \left[\left(E+i\eta\right)S_L^{\dagger} - w_{LC}^{\dagger}\right]\times \bar{G}_{00L}\times\left[\left(E+i\eta\right)S_L - w_{LC}\right]\\ \Sigma_R &= \left[\left(E+i\eta\right)S_R - w_{RC}\right]\times G_{00R}\times\left[\left(E+i\eta\right)S_R^{\dagger} - w_{RC}^{\dagger}\right]\end{aligned} \tag{3.20}$$

where the dagger means complex conjugate. Use the Fisher-Lee relationwe can get the transmission function as

$$\bar{T} = \mathrm{Trace}\left[\Gamma_L G_C \Gamma_R G_C^{\dagger}\right] \tag{3.21}$$

where

$$\begin{aligned}\Gamma_L &= i\left[\Sigma_L - \Sigma_L^{\dagger}\right]\\ \Gamma_R &= i\left[\Sigma_R - \Sigma_R^{\dagger}\right]\\ G_C &= \left[\left(E+i\eta\right)S_C - H_C - \Sigma_L - \Sigma_R\right]^{-1}\end{aligned} \tag{3.22}$$

Therefore the calculated surface Green's function and the transmission spectrum are shown below in Figure 4.6 and Figure 4.7 respectively.As we can see, within the transmission window ($-2t < \left(E-2\varepsilon\right) < 2t$), the transmission is 1.

Suppose a slightly different case, suppose the atomic chain is no longer uniform. For example if the center two atoms have different onsite energy and interactions (seeFigure 4.8), what would the Green's function and transmission be? The case can be considered as the center two atoms bonded in an extra potential well. Therefore we would expect a transmission spectrum of Breit-Wigner like resonances[60]. The calculated transmission in Figure 4.10 does agree with this expectation.

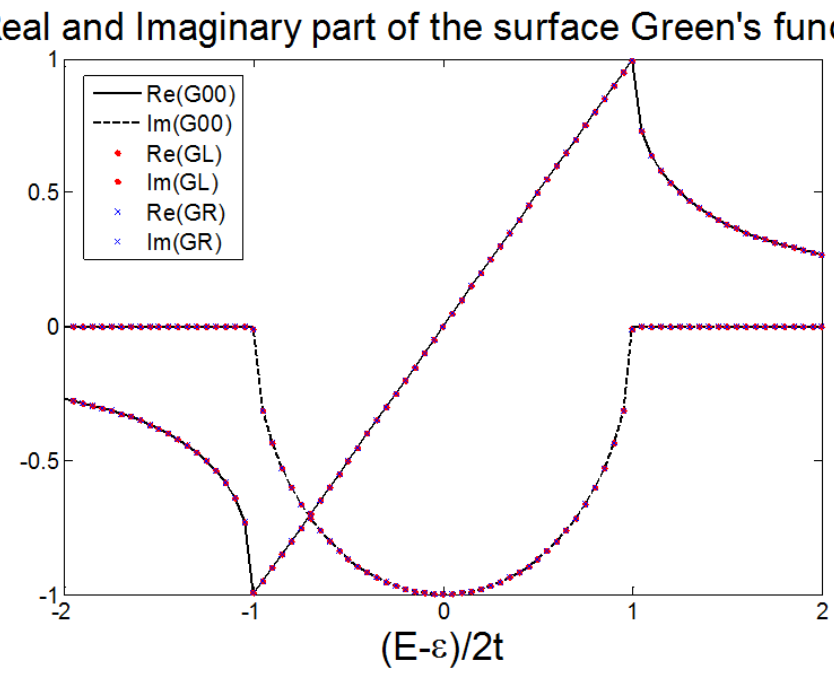

Figure 4.6. Surface Green's function for the uniform 1D atomic chain.

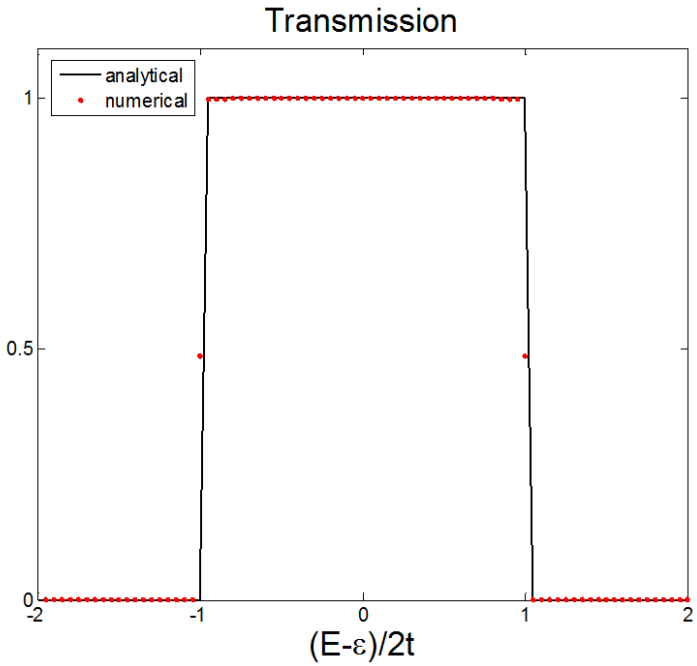

Figure 4.7.Transmission function for the uniform 1D atomic chain. The transmission is 1 within the band.

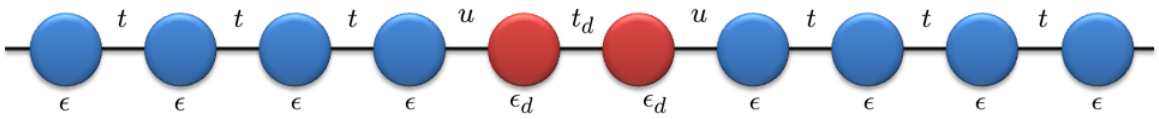

Figure 4.8.1D inhomogeneous atomic chain.

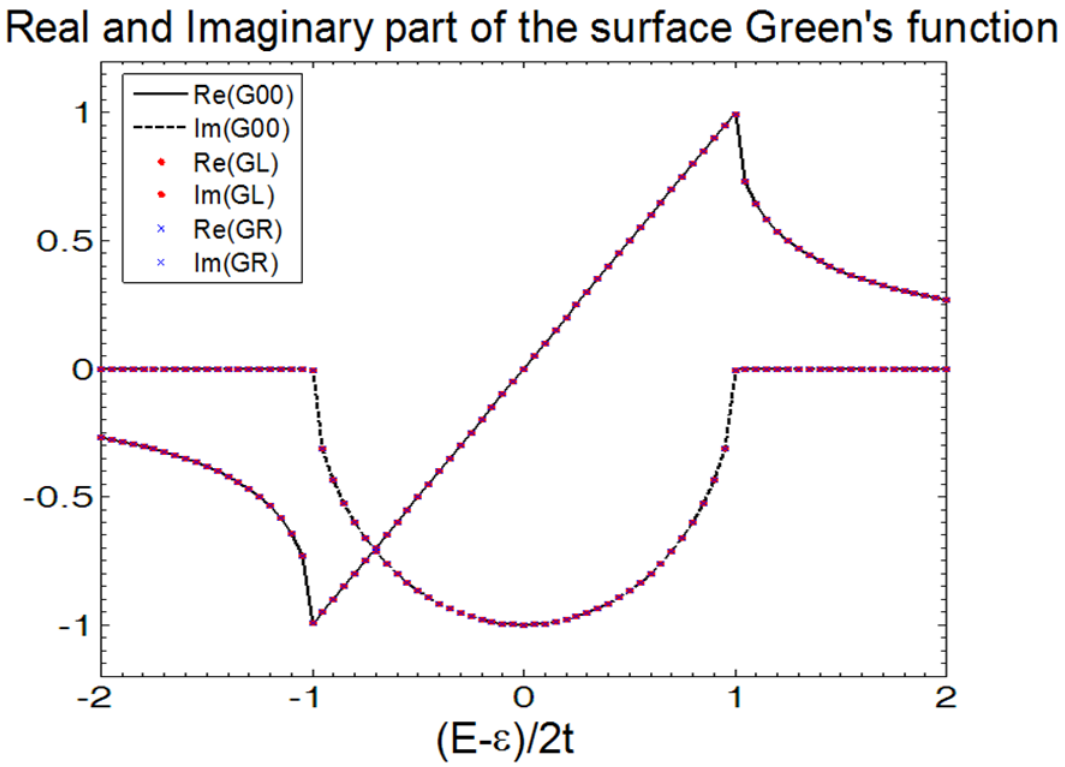

Figure 4.9. Surface Green's function calculated for the 1D inhomogeneous atomic chain.

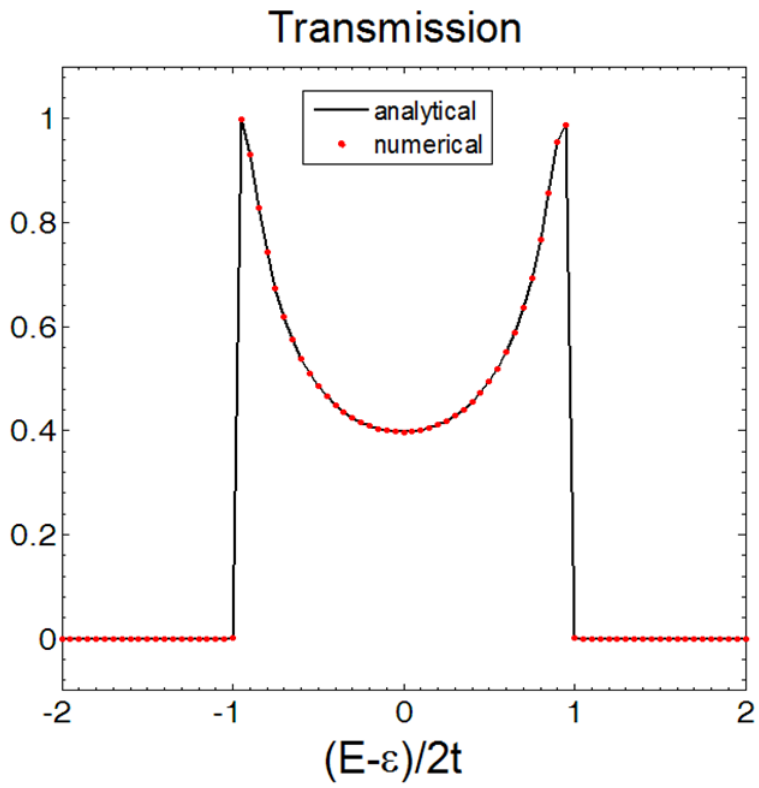

Figure 4.10. Transmission calculated for the 1D inhomogeneous atomic chain.

The calculations done above are all on orthogonal basis, i.e.unitary overlap matrix. For non-orthogonal basis, the Green's function will differ. For a system with Hamiltonian and overlap matrices as

$$H=\begin{pmatrix} \varepsilon & t & 0 & 0 & 0 & 0 \\ t & \varepsilon & t & 0 & 0 & 0 \\ 0 & t & \varepsilon & t & 0 & 0 \\ 0 & 0 & t & \varepsilon & t & 0 \\ 0 & 0 & 0 & t & \varepsilon & t \\ 0 & 0 & 0 & 0 & t & \varepsilon \end{pmatrix} \qquad S=\begin{pmatrix} 1 & w & 0 & 0 & 0 & 0 \\ w & 1 & w & 0 & 0 & 0 \\ 0 & w & 1 & w & 0 & 0 \\ 0 & 0 & w & 1 & w & 0 \\ 0 & 0 & 0 & w & 1 & w \\ 0 & 0 & 0 & 0 & w & 1 \end{pmatrix}, \tag{3.23}$$

in which $0<w<1$, the Green's function is calculated and shown in Figure 4.11.

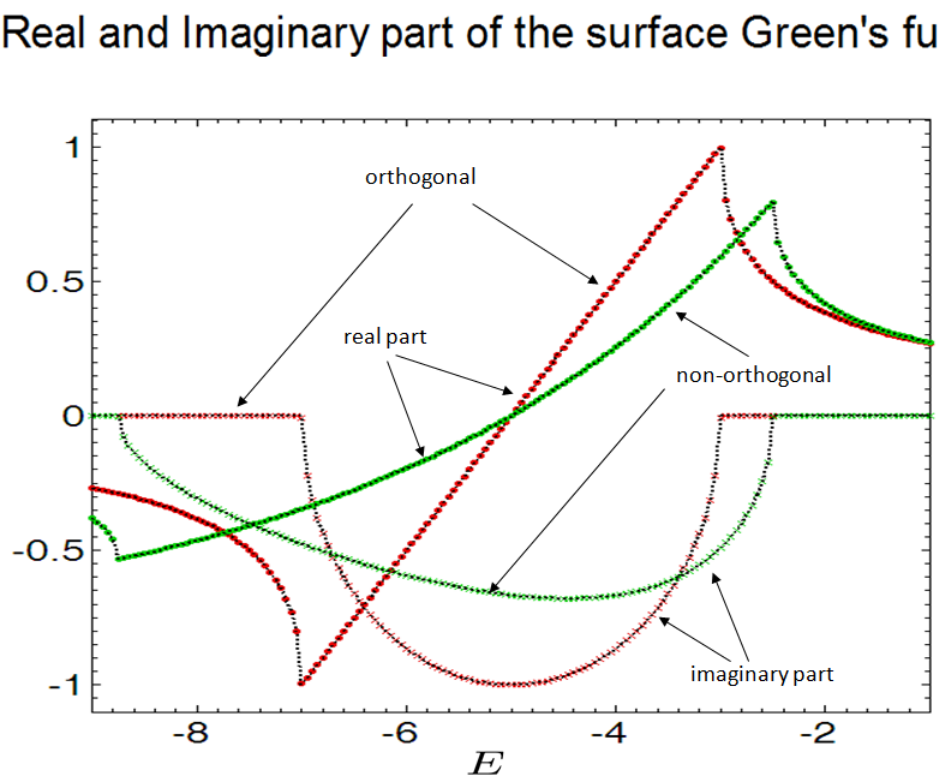

Figure 4.11. Surface Green's function for 1D homogenous atomic chain on different basis.

4.3.2 Three dimensional system: pure Fe

In order to do the calculations for pure Fe, we need to fit EHTB parameters to first principle results in order to get a good description of the system first. Using a MATLAB based EHTB bands fitting program, we get the fitting results as below. It is obtained by fixing K factor to 2.8. The K factor is correlated to the ς values hence freeing it in the fitting will increase numbers of local minimums, which would increase large amount of calculation time for slightly better fitting result. Therefore fixed K factor is a trade-off here.

We also need to put on limits for the fitting parameters, especially for the ς values. As one can see from (3.5), the two ς are actually interchangeable, which doubles the number of

local minimums and hence increase the calculation time. Therefore it is better to put on different limits on to the pair of ς values for the same orbit. For instance, if one knows that ς value should be between 1.8 and 25, one would divide the range, forcing ς_1 to change between 1.8 and an in-between number such as 5.0, and the other ς, ς_2, to change between 5.0 and 25.

The limits on onsite energies can also be analyzed from the band composition. If d orbitals contributes to bands in a certain energy range, we can use this energy range as the limits for the d orbital onsite energy. However it is a rough approximation and the range may needs to be expanded sometimes.

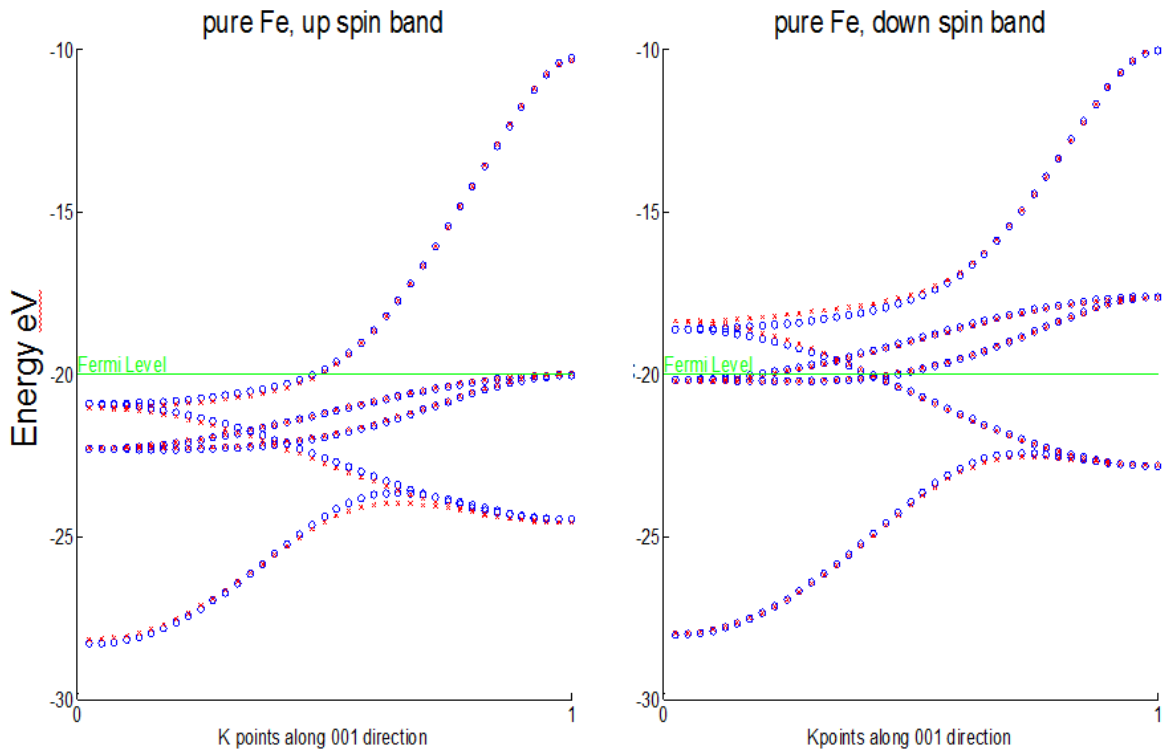

Figure 4.12.EHTB fitting for pure Body Centered Cubic (bcc) Fe (lattice constant 2.87).*Left* is for up spin and *right* is for down spin. The blue circled dots are FP results calculated by VASP. The red crossed dots are EHTB fitting results.

Table 3. EHTB parameters for pure bcc Fe

Atom	**Orbital**	ς_1	ς_2	Onsite Energy (eV)	C_1	C_2
Fe		Majority bands fitted parameters				
	4s	2.83	13.83	-18.58	0.99	0.07
	3p	1.8	21.83	-9.81	0.63	0.77
	3d	2.1	19.45	-21.76	0.38	0.92
		Minority bands fitted parameters				
	4s	2.75	7.19	-17.52	1	0
	3p	1.8	20.1	-9.45	0.75	0.69
	3d	1.8	4.24	-19.67	0.25	0.85

K factor is fixed to 2.80 in both cases. Fermi level is at -20 eV.

We calculated the transmission based on EHTB parameters shown in Table 3. The transmission for pure Fe at Γ (0, 0, 0) and at H (0, 0, 1) are shown below. The band diagram at the center tells us about the distribution of transverse modes. Comparing the bands at Γ point to the transmission at Γ points, we can see that the transmission is actually the number of transverse modes. It is the same case for the H point too. The agreement is pretty well around Fermi level (0eV in the Figure) because of the "tight binding" assumption. For higher energy levels, dispersion appears.

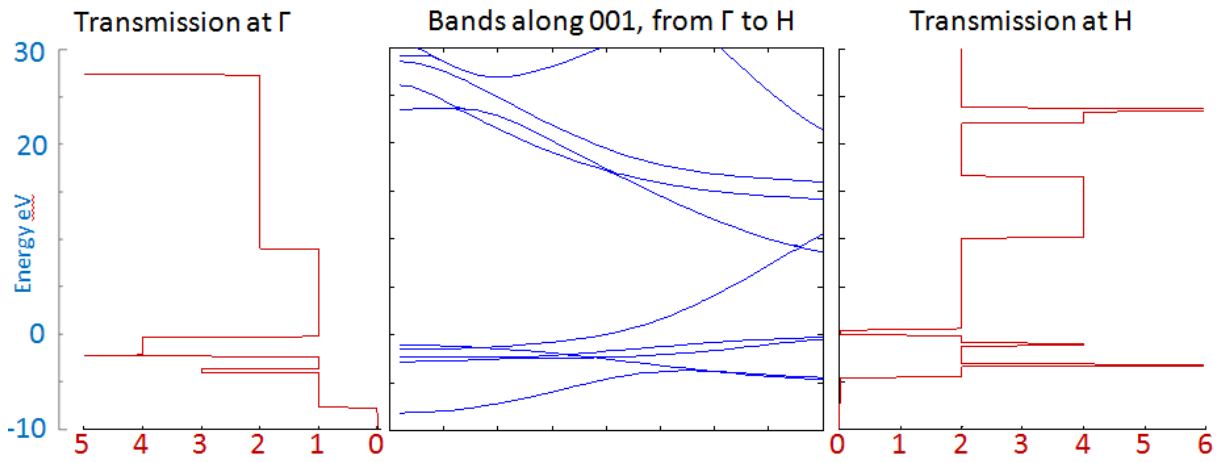

Figure 4.13.Transmission spectrums for pure Fe. Among all three figures, the y axis is for energy and the scale is kept the same.

4.3.3 Three dimensional system: Fe-MgO-Fe

The prediction of high TMR in the Fe/MgO/Fe junction based on symmetry filtering effect (see Symmetry Filtering effect) by Butleret al[39] and later on experimental proof by Bowen et al[40]in 2001 has drawn a lot of attention to the Fe/MgO/Fe systems. The next example will be the transmission spectrum for a series of Fe/MgO/Fe junctions.

Unstrained bcc Fe's lattice constant is 2.87 Å while unstrained Face Centered Cubic (fcc) MgO's lattice constant is 4.21Å. There would be a lattice mismatch if we put Fe on top of MgO, which can be resolved by "stretching" Fe to fit MgO. In other words, the Fe will not be a cubic but a tetragonal structure. The "stretched" Fe lattice constant should be $a = 4.21/\sqrt{2} = 2.98$ Å. The c/a ratio of the tetragon calculated by ab initio relaxation is 0.91.

For MgO, we did the band calculation along the symmetry line from Γ to X . However, sometimes we may need to sample the 3D first Brillouin Zone (FBZ) for band calculations

evenly to make sure we have a good representation of a certain system. For strained Fe, we use the Monkhorst-Pack scheme to generate a minimum set of evenly sampled kpoints[61-63]. The generated kpoints are plotted inFigure 4.15.

Upon the information mentioned above we obtained bands diagramsfor strained Fe in 3D FBZ and MgO for the 001 direction, to which the EHTB parameters are fitted. The fitted EHTB parameters and bands diagrams are shown in Table 4 and Figure 4.15 respectively.

Table 4. EHTB parameters for strained Fe and MgO

Atom	**Orbital**	ς_1	ς_2	Onsite Energy (eV)	C_1	C_2
Fe		Majority bands fitted parameters				
	4s	1.93	23.46	-15.34	0.56	0.83
	3p	1.6	8.71	-11.92	0.44	0.87
	3d	2.08	17.06	-21.79	0.37	0.92
		Minority bands fitted parameters				
	4s	1.93	23.5	-14	0.67	0.74
	3p	1.67	20.92	-11.4	0.51	0.86
	3d	2.03	20.42	-19.51	0.4	0.91
Mg	3s	1.94	18.51	-15.17	0.65	0.74
	3p	1.85	17.31	-13.99	0.46	0.88
O	2s	2.04	20.57	-38.02	0.29	0.94
	2p	1.85	19.39	-23.17	0.56	0.8

K factor is fixed to 2.80 in both cases. Fermi level is at -20 eV.

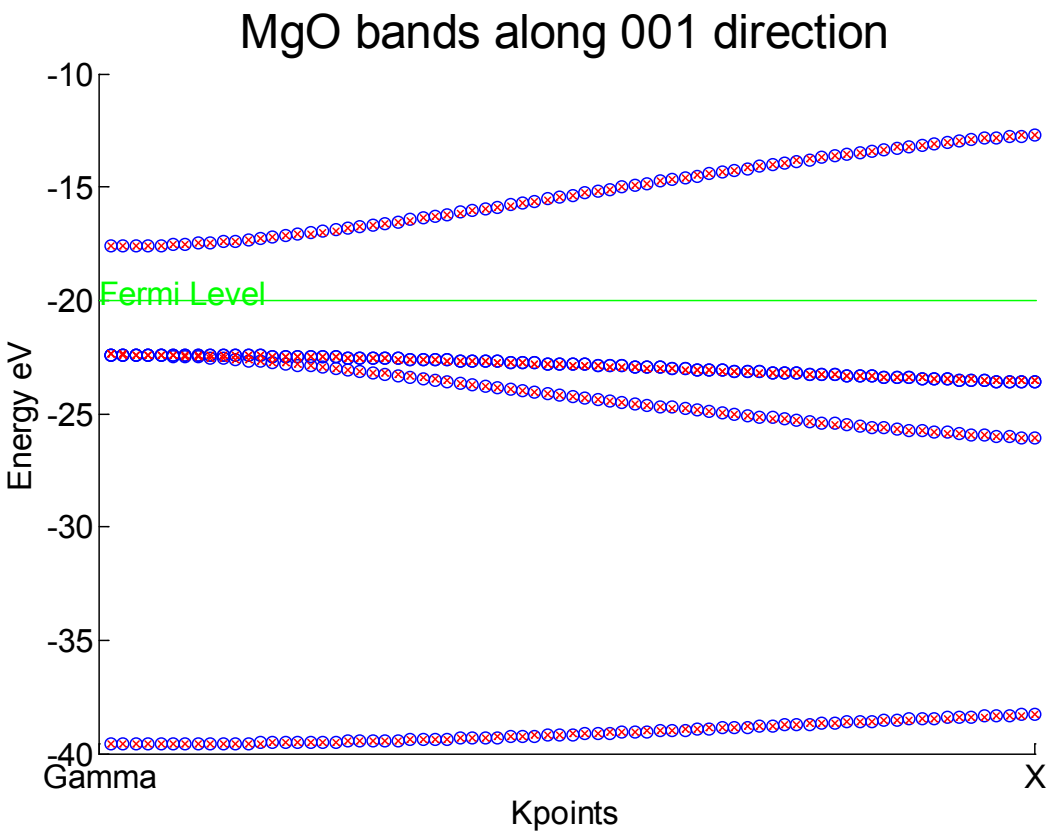

Figure 4.14. EHTB fitted bands for MgO. The blue circled dots are FP results calculated by VASP. The red crossed dots are EHTB fitting results.

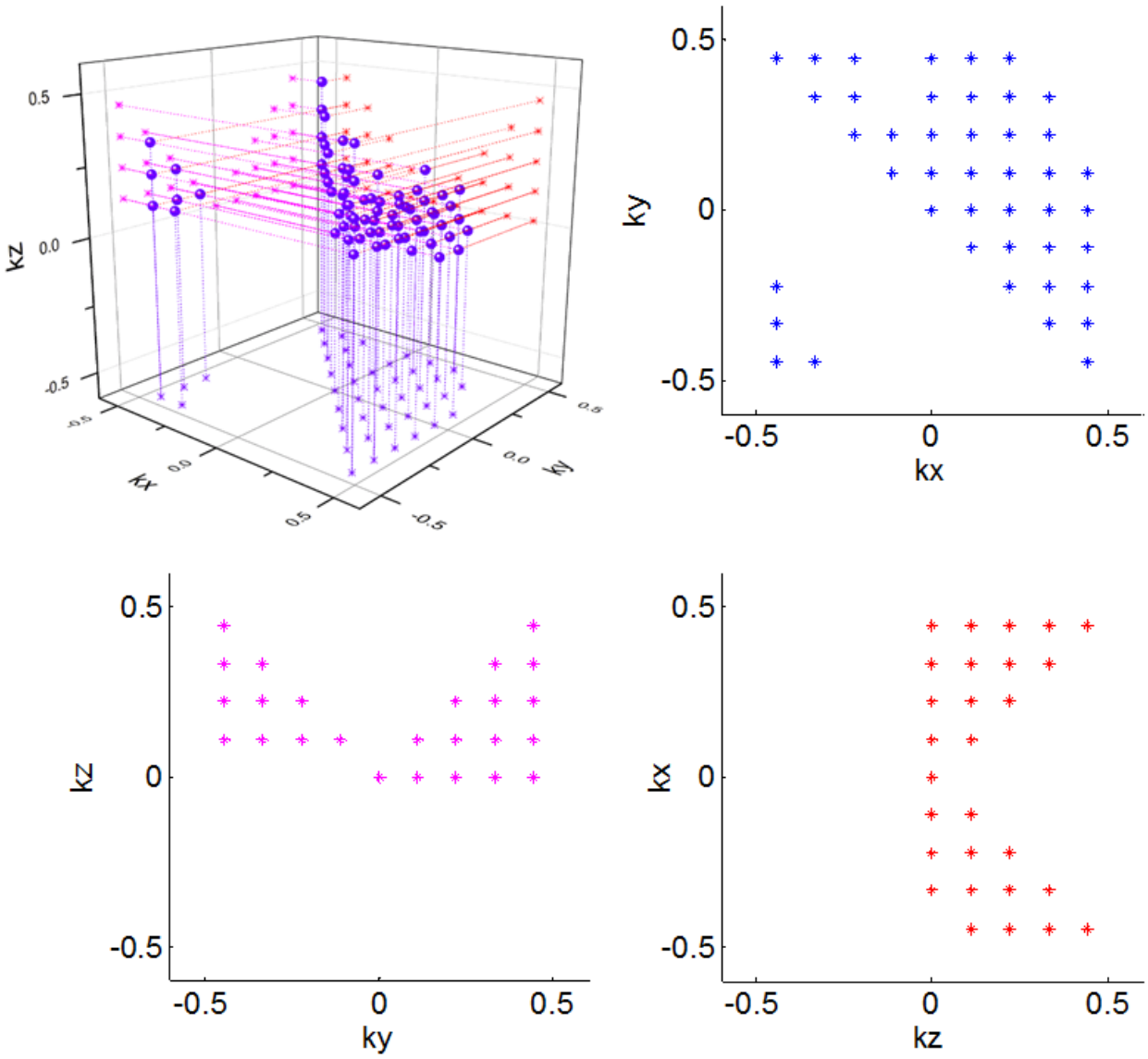

Figure 4.15. Kpoints generated based on Monkhorst-Pack. *Top left:* 3D plotting; *top right:* x-y plane projection; *bottom left:* y-z plane projection; *bottom right*: z-x plane projection.

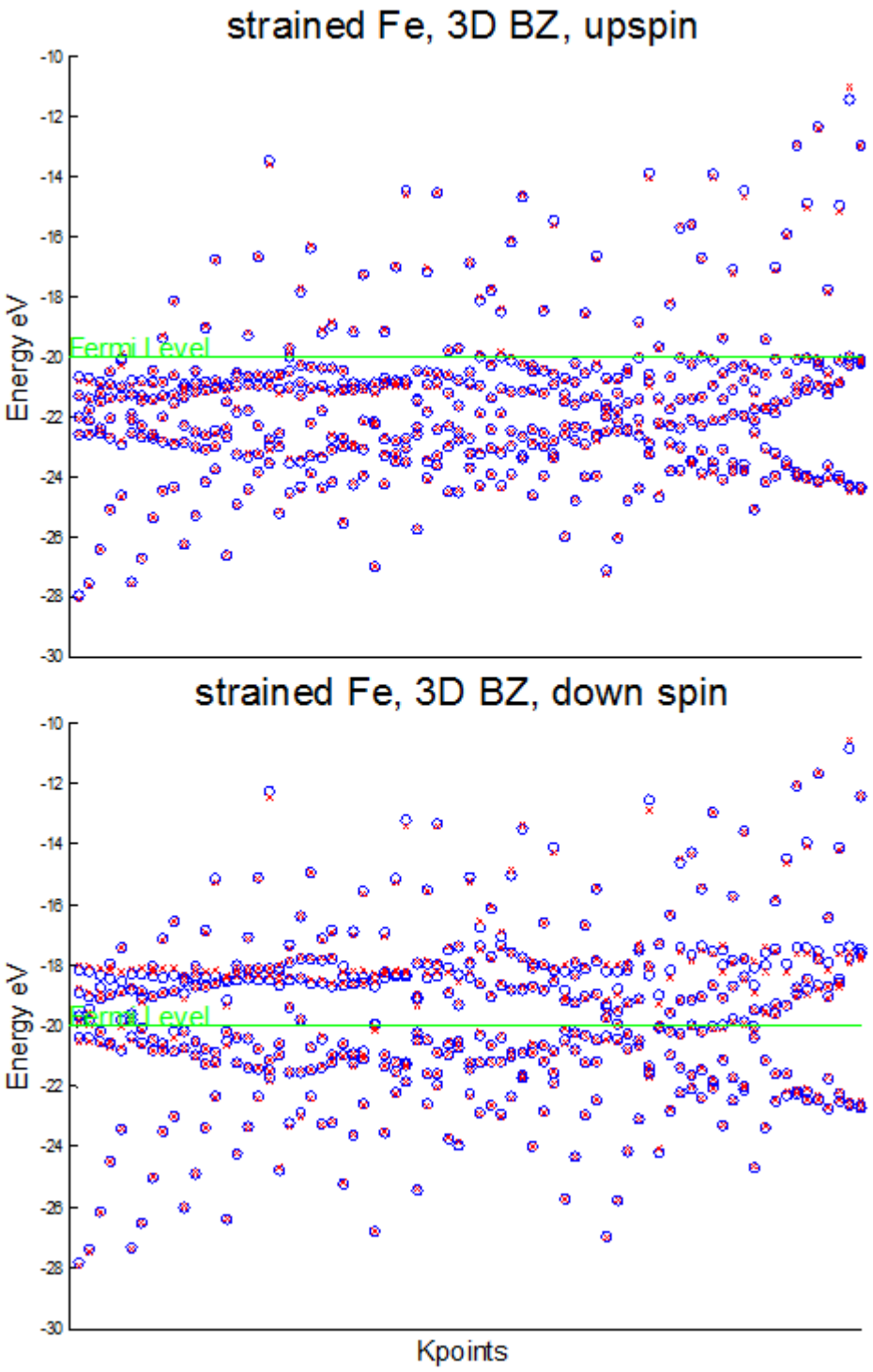

Figure 4.16. EHTB fitted bands for strained Fe (lattice constant 2.87A, c/a ratio 0.91). The blue circled dots are FP results calculated by VASP. The red crossed dots are EHTB fitting results. The kpoints are sampled in the 3D FBZ and therefore look random.

For the $k_x = k_y = 0$, the calculated Transmission spectrum is shown below. We can see that the more MgO layers the system has, the less the transmission will be at the Fermi level.

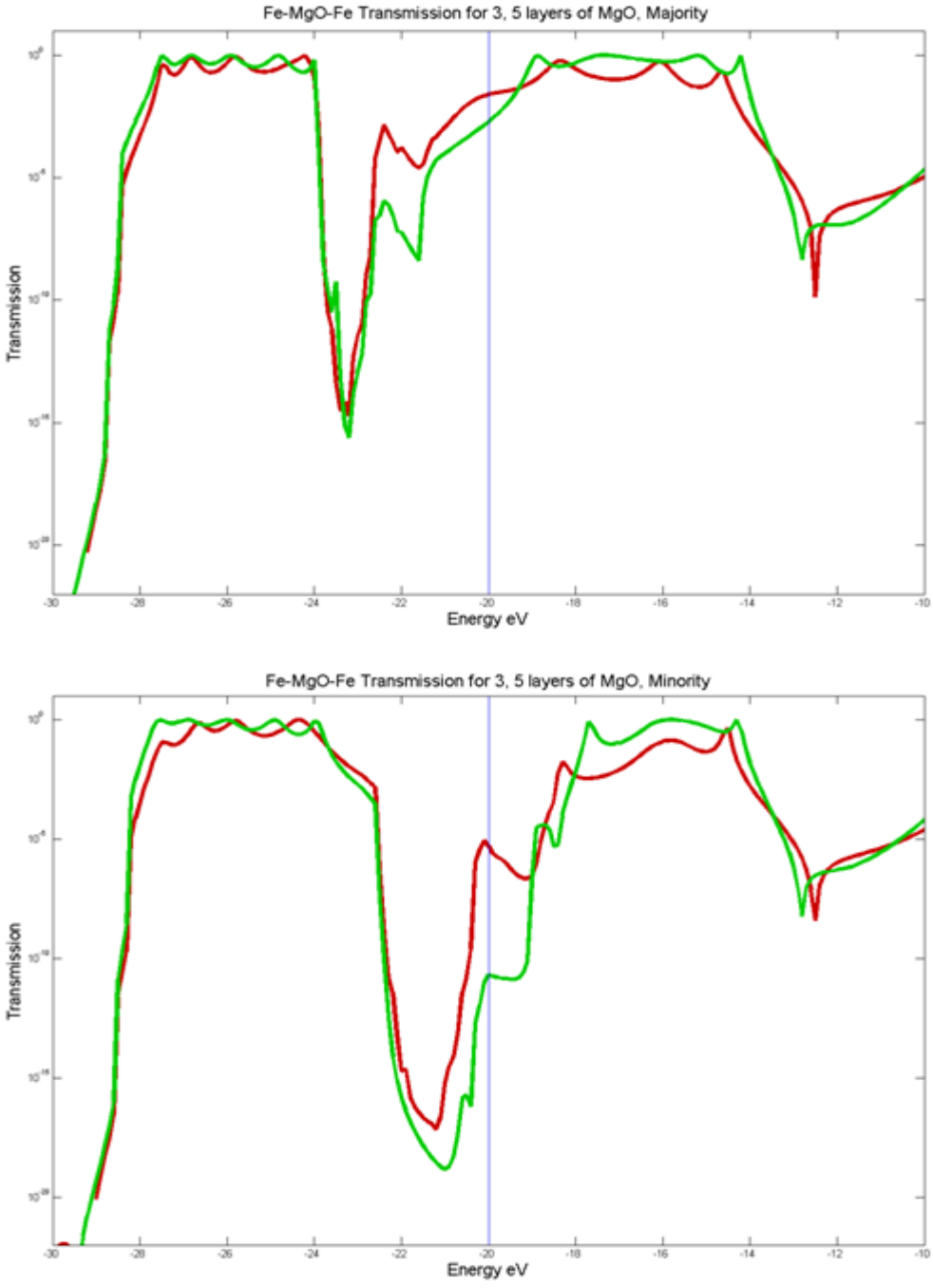

Figure 4.17. Transmission spectrum of Fe-MgO-Fe junctions at $k_{||} = 0$. The red line is for Fe/3MgO/Fe, and the green line is for Fe/5MgO/Fe. The Fermi level is at -20 eV.

The above calculations are for specific kpoint only. The real transmission spectrum $\overline{T}(E)$ should be integrated transmission over the two dimensional FBZ in the x-y plane if the transport is along z direction, which means we need to do k-points sampling in the FBZ. So another technical point needs to be covered is the two dimensional k-points sampling.

There are five types of Bravais lattices in the two dimensional case, oblique, primitive rectangular, centered rectangular, hexagonal, and square. Each of them has symmetry that we can take advantage of to reduce the number of sampled kpoints. We can reduce the number of sampled kpoints dramatically by reducing the FBZ to an irreducible one and putting weight on thekpoints that have symmetrical mates (see Figure 4.18). An example of calculated Transmission spectrum over FBZ is shown below.

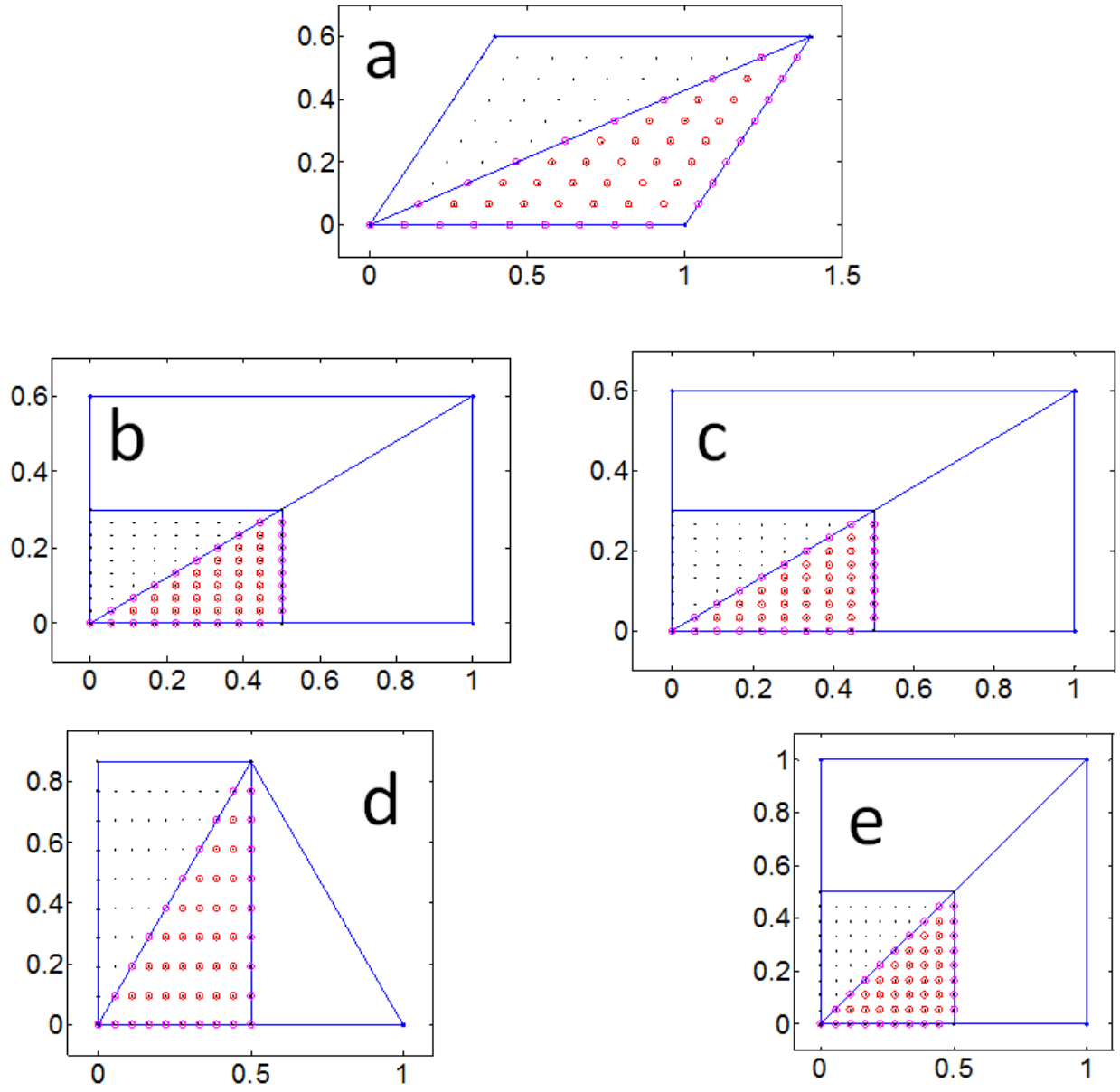

Figure 4.18. 2D lattice types, from subfigure a to e are oblique, primitive rectangular, centered rectangular, hexagonal, and square respectively. The circled points are chosen as the k-points of irreducible Brillouin Zone. Color of the circle represents weight of the circled point.

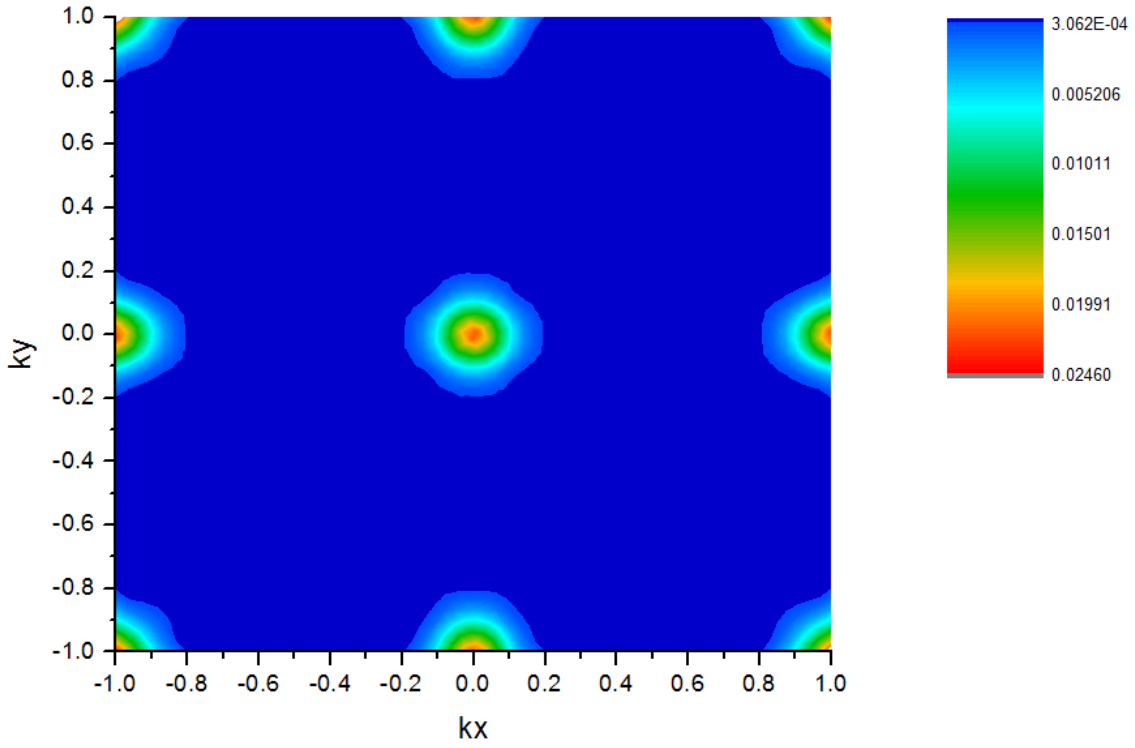

Figure 4.19. Transmission for Fe-MgO3-Fe at Fermi level in the majority channel, kpoints grid spacing is 0.1.

CHAPTER 5 MAGNETIC DAMPING

5.1 Magnetic Dynamics basics

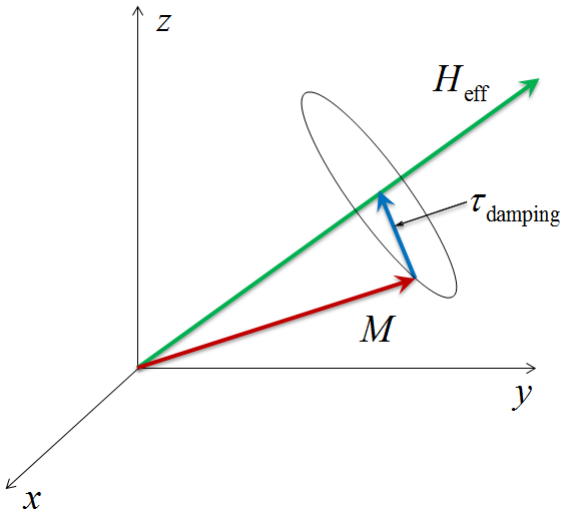

Figure 5.1. Precession of Magnetization in a magnetic field. The magnetization precesses around the effective magnetic field as magnetic damping gradually reduces the precession angle and causes the magnetization to align with the effective field.

The evolution of magnetization can be described by an equation of motion proposed by Landau and Lifshitz in 1935[64, 65], known as the Landau-Lifshitz equation (LL equation).

$$\frac{d\bar{M}}{dt} = -\gamma\mu_0 \bar{M} \times \bar{H}_{\text{eff}} - \frac{\lambda}{M_s^2} \bar{M} \times \left(\bar{M} \times \bar{H}_{\text{eff}} \right) \tag{4.1}$$

where $\gamma = \frac{g\mu_B}{\hbar}$ is the gyromagnetic ratio ($\frac{1.76\times10^{11}\,\text{radian}}{\text{Tesla}\cdot\text{second}}$ for a free electron), $\vec{M}$ is the magnetization, $\vec{H}_{\text{eff}}$ is the effective field comprised of external field, exchange field and anisotropy field, $\lambda = 1/\tau_{\text{damping}}$ is the material-dependentrelaxation ratethat measures the rate at which the precessional motion is damped.

An alternative approach was proposed by Gilbert[66, 67] in 1955. He treated the damping as a viscous torque and introduced the damping term as $\frac{\alpha}{M_s}\vec{M}\times\frac{d\vec{M}}{dt}$ where α is a dimensionless constant. The damping torque in this approach is proportional to and orthogonal to the rate of change of the magnetization. Thus Gilbert's equation is given by,

$$\frac{d\vec{M}}{dt} = -\gamma\mu_0\vec{M}\times\vec{H}_{\text{eff}} + \frac{\alpha}{M_s}\vec{M}\times\frac{d\vec{M}}{dt} \tag{4.2}$$

Gilbert's equation,(5.2), can be transformed into the form of the LL equation, (5.1), by substituting the entire right hand side of (5.2) for $\frac{d\vec{M}}{dt}$ on the right hand side,

$$\frac{d\vec{M}}{dt} = -\gamma\mu_0\vec{M}\times\vec{H}_{\text{eff}} + \frac{\alpha}{M_s}\vec{M}\times\left[-\gamma\mu_0\vec{M}\times\vec{H}_{\text{eff}} + \frac{\alpha}{M_s}\vec{M}\times\frac{d\vec{M}}{dt}\right] \tag{4.3}$$

andusing the fact that the magnetization and its rate of change are orthogonal, $\vec{M}\cdot\left(d\vec{M}/dt\right) = 0$ so thatGilbert's equation becomes the LLG equation,

$$\frac{d\vec{M}}{dt} = -\gamma^*\mu_0\vec{M}\times\vec{H}_{\text{eff}} - \frac{\alpha\gamma^*\mu_0}{M_s}\vec{M}\times\left(\vec{M}\times\vec{H}_{\text{eff}}\right) \tag{4.4}$$

Comparing the two equations of motion, (5.1)and (5.4), we have

$$\gamma^* = \frac{\gamma}{1+\alpha^2}; \quad \alpha = \frac{\lambda}{\gamma^* \mu_0 M_s} \tag{4.5}$$

Both equations of motion preserve the absolute magnetization, $\vec{M} \cdot \vec{M} = M_s^2$.

The two equations are almost identical when the damping is small ($\alpha^2 \ll 1$).But for large damping, e.g. for α or $\lambda \to \infty$, the LL equation yields an almost immediate switch since, $d\vec{M}/dt \to \infty$ while the LLG equation gives $d\vec{M}/dt \to 0$. The latter one makes more physical sense since the motion of magnetization should be slowed down as the "viscosity", i.e. damping, increases. It was also shown bythe analysis of experimental results that the LLG equation is more successful than the LL equation for analyzing the frequency dependence of the damping[68]. We will continue to use the LLG equation in the following text.

The damping parameter α is sample-dependent and comprises both intrinsic and extrinsic contributions. The intrinsic damping may include the spin-orbit coupling, dipole-dipole interactions and even phonon or magnon contributions [69, 70]. The extrinsic damping may include defects as well as other controllable geometrical effects. For experimentalists, one assumes the minimum measured damping (minimum FerroMagnetic Resonance linewidth) under well defined thermodynamic conditions to be the intrinsic damping[71].

5.2 Kamberský's torque correlation model

The magnon-phonon scattering , i.e. Phonon drag[72], is a very small effect and thus cannot explain the measured damping in magnetic metals[73]. Eddy current damping[74] can explain the damping in thick metallic samples at high frequencies[75], but for ultrathin films, the eddy current effect is negligible. We expect that spin-orbit relaxation should be the dominatedamping mechanism in smooth, homogeneous ultrathin metal films.

Kamberský proposed a method the treat the intrinsic damping by using the spin-orbit interaction Hamiltonian[76-78]. The Gilbert damping constant can be expressed as

$$\lambda = \frac{\mu_0 g^2 \mu_B^2}{\hbar} \frac{\pi^2/2}{\Omega_{atom}} \left\langle \sum_{m,n} \left| \Gamma^-_{m\vec{k},n\vec{k}} \right|^2 W_{m\vec{k},n\vec{k}} \right\rangle_{\vec{k}} \tag{4.6}$$

where g is the Landé g-factor, μ_0 is the vacuum permeability, μ_B is the Bohr magneton, m and n are band indices that represent the projected local orbitals of Bloch states, $\vec{k}$ is the electron wave vector, and $\langle\ \rangle_{\vec{k}}$ means the average over the FBZ. $\Gamma^-_{m\vec{k},n\vec{k}}$ is element of the transition matrix that describes transition between band m and band n due to the spin-orbit relaxation and can be calculated by

$$\Gamma^-_{m\vec{k},n\vec{k}} = \left\langle m,\vec{k} \left| \left[\sigma^-, H_{SO} \right] \right| n,\vec{k} \right\rangle \tag{4.7}$$

in which H_{SO} denotes the Hamiltonian with spin-orbit coupling. $W_{m\vec{k},n\vec{k}}$ is the spectral overlap function defined by

$$W_{m\vec{k},n\vec{k}} = \frac{1}{\pi} \int \eta(E) \left\langle D\left(E_{m\vec{k}}\right) \right\rangle \times \left\langle D\left(E_{n\vec{k}}\right) \right\rangle dE \tag{4.8}$$

in which $\eta(E)$ is the negative derivative of the Fermi function and $\langle D(E_{m\bar{k}})\rangle$ is the averaged spectral DOS.

$$\langle D(E_{m\bar{k}})\rangle = \frac{1}{\pi}\frac{\delta}{\left[\left(E - E_{m\bar{k}}\right)^2 + \delta^2\right]} \tag{4.9}$$

where $\delta = \hbar/(2\tau)$ is defined by the lifetime of the Bloch state.

The contribution to the Gilbert damping from the intra-band transitions ($m = n$) is proportional to the relaxation time τ and consequently scales with the conductivity while the contribution from inter-band transitions is proportional to the inverse of relaxation time $1/\tau$ and consequently scales with the resistivity. As the temperature increases, the relaxation rate also increases and eventually becomes comparable to the energy gap between bands m and n, i.e. the inter-band Gilbert damping gradually saturates as the temperature increases[76, 79].

The spin-orbit interaction can be introduced by adding a spin-orbit term, H_{SO}, to the EHTB Hamiltonian,

$$H = H_0 + H_{SO} = H_0 + \eta\sum_i L_i \cdot S_i \tag{4.10}$$

where η is the spin-orbit coupling parameter which we assume to be the same for all types of atoms in the same material[80], L_i and S_i are the angular momentum operator and spin operator at site i respectively. In the EHTB model, the basis set(3.6) now doubles since the majority and minority spins cannot be treated separately. The spin-orbit coupling is proportional to the gradient of the effective potential seen by an electron which is largest near the nucleus, hence we can assume the matrix element at site i is only related to $L_i \cdot S_i$ and ignore contributions from other sites. The detailed table of non-zero matrix element has been calculated

accordingly by Chunsheng Liu and listed in Table 2 of his dissertation [81]. Hence the Gilbert damping constantcan be calculated.

5.3 Damping calculation for MnAl system

MnAl has only one ferromagnetic phase, the metastable τ phase, withMn composition ranging from 50% to 60% according to the phase diagram (see Figure 2.1)[82, 83]. It has a tetragonal $L1_0$ structure.

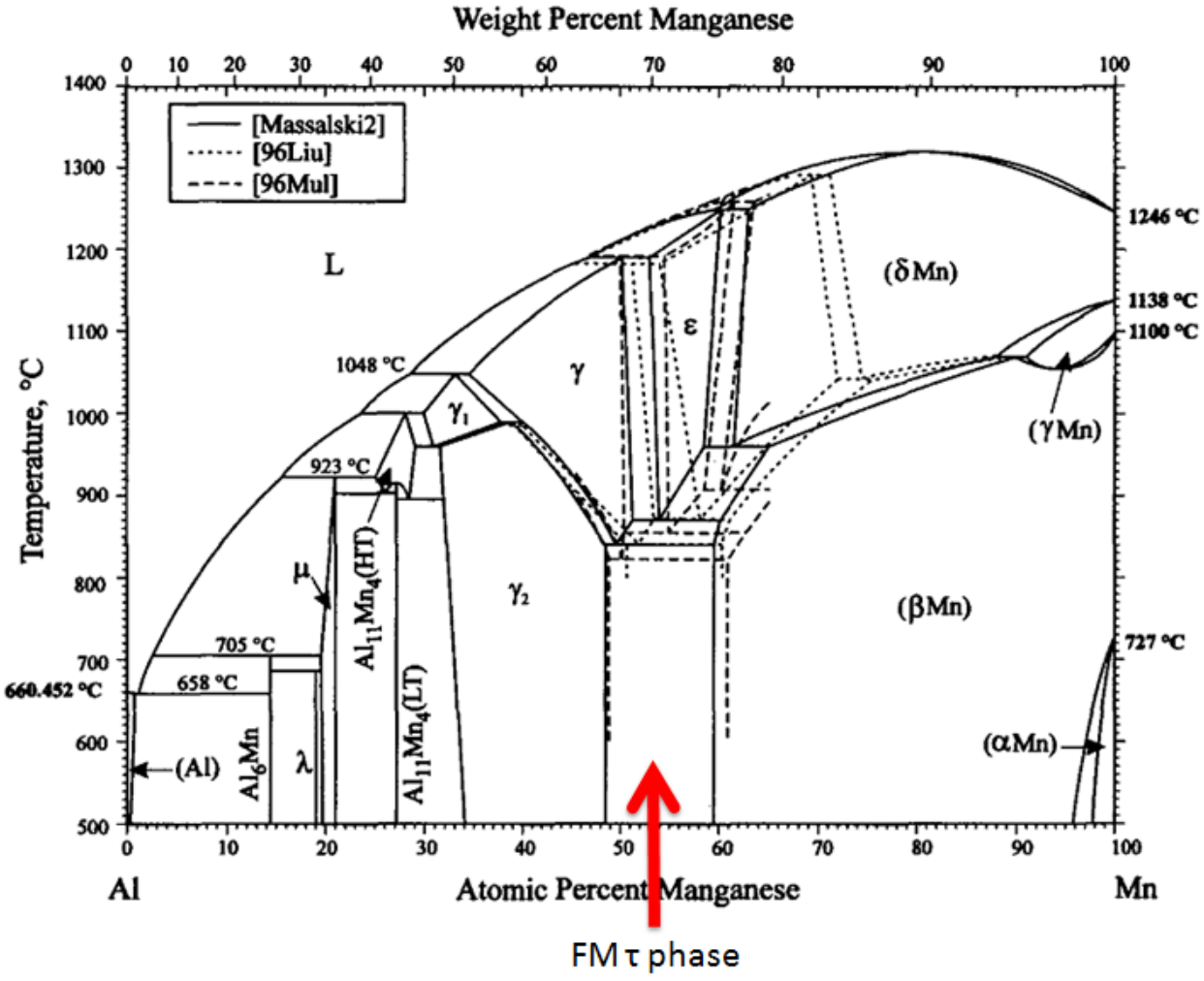

Figure 5.2. Manganese Aluminum binary phase diagram (Okamoto 1997[83]), the ferromagnetic τ phase is a metastable phase that forms in the two-phase region between γ_2 and β Mn.

By performing anab initio structure relaxation using VASP, we obtained the physical and magnetic structure of $L1_0$ MnAl. The basis vectors are $\begin{Bmatrix} 0.5 & 0.5 & 0 \\ -0.5 & 0.5 & 0 \\ 0 & 0 & 0.88 \end{Bmatrix}$;the lattice constant is 3.91Å, and the magnetization is $2.2976\mu_{Bohr}$ per unitcell. Based upon which, we did the EHTB band fitting to MnAl up and down spins separately and obtained the EHTB parameters as the starting point for the fitting with spin orbit coupling.

The corresponding EHTB parameters for the fitting in Figure 5.3 are listed in Table 5. Note the K factors are not fixed in this case for better accuracy. Then we used these parameters as the starting point for fitting with SO coupling and obtained the fitting results shown in Figure 5.4 with parameters given in Table 6.

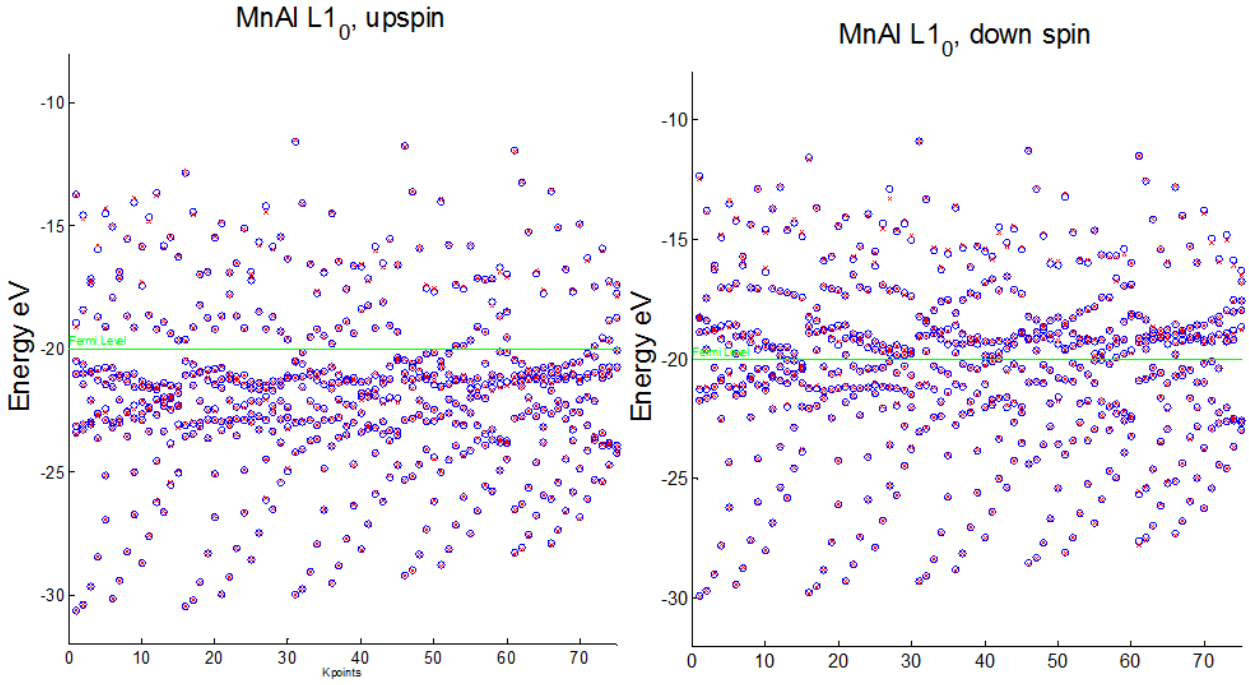

Figure 5.3. EHTB fitting for MnAl of $L1_0$ structure done in the 3D FBZ,the blue circled dots are FP results calculated by VASP;the red crossed dots are EHTB fitting results.*Left* is for majority and *right* is for minority.

Table 5.EHTB parameters for MnAl of $L1_0$ structure

Atom	**Orbital**	ς_1	ς_2	Onsite Energy (eV)	C_1	C_2
		Majority bands fitted parameters				
	4s	1.58	25	-18.15	0.47	0.88
Mn	3p	1.21	9.09	-13.91	0.57	0.8
	3d	1.83	4.05	-21.49	0.34	0.77
	3s	1.78	25	-21.92	0.73	0.68
Al	3p	1.49	5.16	-17.37	0.71	0.53
	3d	0.9	2.2	-11.92	0.5	0.65
		Minority bands fitted parameters				
	4s	1.58	25	-16.21	0.5	0.86
Mn	3p	1.15	3.56	-11.38	0.85	0.31
	3d	1.65	3.6	-19.53	0.36	0.74
	3s	1.56	25	-22.42	0.62	0.75
Al	3p	1.21	2.9	-17.61	0.47	0.67
	3d	0.9	2.32	-11.96	0.54	0.63

The K-factor for Mn-Mn, Mn-Al and Al-Al are 2.14, 2.01, and 1.89 for the majority spin channel; and 1.83, 1.89 and 1.92 for the minority spin channelrespectively. The Fermi level is at -20eV.

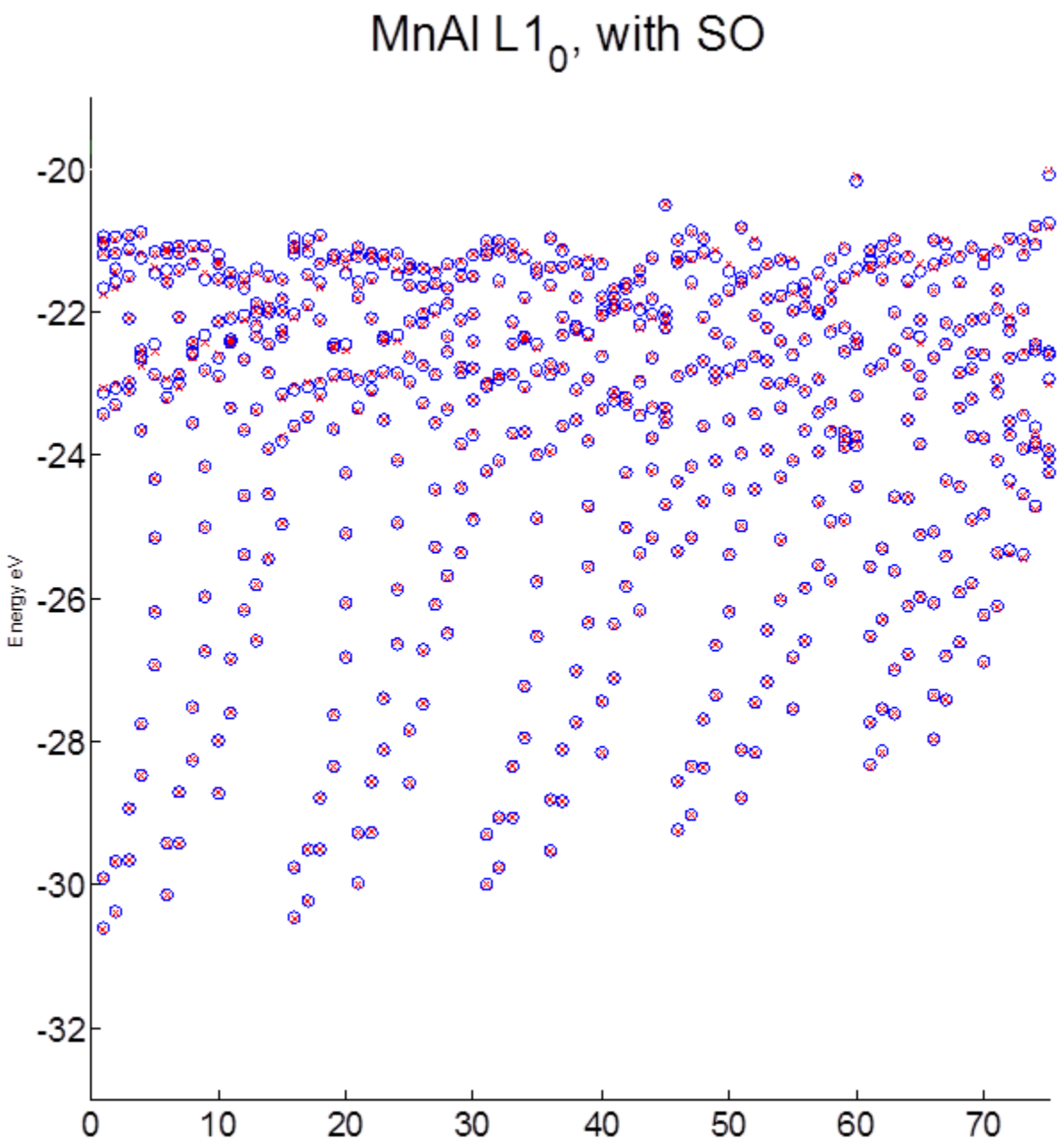

Figure 5.4.EHTB fitting with SO coupling for MnAl of $L1_0$ structure,fitting is done in the 3D FBZ. The blue circled dots are FP results calculated by VASP. The red crossed dots are EHTB fitting results.

Table 6.EHTB parameters for MnAl of $L1_0$ structure with SOcoupling

Atom	**Orbital**	ς_1	ς_2	Onsite Energy (eV)	C_1	C_2
Mn	4s	1.58	25	-18.15	0.47	0.88
	3p	1.21	9.09	-13.91	0.57	0.8
	3d	1.83	4.05	-21.49	0.34	0.77
Al	3s	1.78	25	-21.92	0.73	0.68
	3p	1.49	5.16	-17.37	0.71	0.53
	3d	0.9	2.2	-11.92	0.5	0.65

The K-factor for Mn-Mn, Mn-Al and Al-Al are 2.14, 2.01, and 1.89 respectively. SO factor $\eta\hbar^2 = 9.38\text{E}-2$.

Based on the EHTB fitting with SO results, we performed the damping calculation and obtained the corresponding intrinsic damping constant $\alpha = \frac{\lambda_{\min}}{M_s \gamma} = 0.0057$.

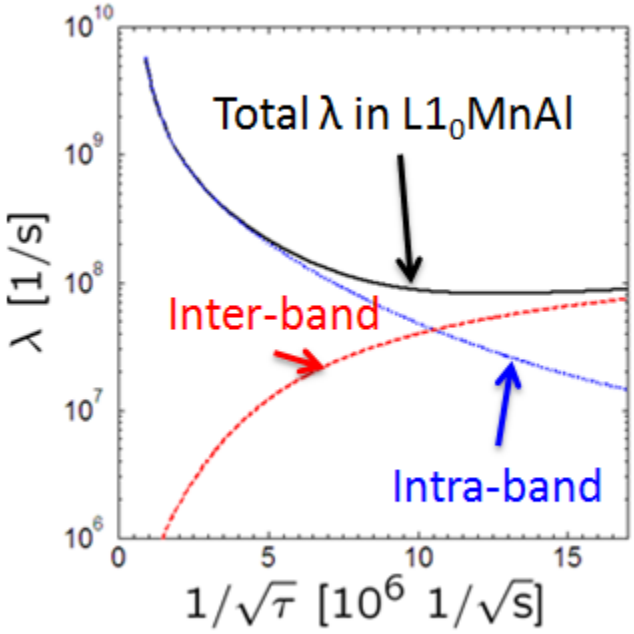

Figure 5.5. The damping for MnAl of $L1_0$ structure

CHAPTER 6 DESIGNING MATERIALS FOR MTJ BASED SPIN TRANSFER TORQUE MAGNETIC RANDOME ACCESS MEMORIES

6.1 Materials needed for STT-MRAM

Spin Transfer Torque Magnetic Random Access Memory (STT-MRAM), a novel application of Spintronics, has great potential for meeting the increasing demanding for higher speed, higher density, lower power consumption and lower cost storage devices in the information technology industry. The comparison of STT-MRAM and other memories is shown in Table 7.

Table 7.Comparison between common memories and MRAMs

		SRAM	DRAM	NOR Flash	NAND Flash	1st gen. MRAM	STT-MRAM
Time	*Write/erase*	1-100 ns	50 ns	0.1-10 ms	0.1-1 ms	3-20 ns	2-20 ns
	Read (ns)	1-100	30	10	50	3-20	2-20
Scalability	*Cell factor (F2)*	50-120	6-10	10	2-5	16-40	6-20
	Min feature(nm)	45-180	45-130	45-130	45-130	65-130	25-50
Endurance	*No. of writes*	10^16	10^16	10^5	10^5	10^15 min	10^15 min
	Volatility	Volatile	Volatile	Non-volatile	Non-volatile	Non-volatile	Non-volatile
Power	*Input voltage(V)*	None	2	6-8	16-20	3	<1.5
	Consump-tion, write	Low	Low	High	High	Moderate	Low
	Other	Leakage current	Data refresh	None	None	None	None
Architecture	*Interface*	RAM	RAM	RAM	Indirect	RAM	RAM
	Usage	CPU cache	Main memory	XIP, 2nd memory	2nd memory	Universal	Universal

Source: Nikkei Electronics [84]

The first generation of MRAM received much attention as a non-volatile memory in the first decade of this century, butis confined to niche market segments because it does not scale well to higher densities.Unlike its predecessor,who uses magnetic fields for writing, STT-MRAM has a simpler structure and operation and is expected to achieve densities competitive

with NOR flash and DRAM. Instead of using the current induced Oersted field, the switching of thestorage bit's magnetization is done by the injection of spin polarized current.

The Spin Transfer Torque effect (STT effect) was predicted independently by Slonczewski[85] and Berger[86] in 1996. Since the spin polarized current carries an angular momentum, it can interact with the magnetization in magnetic layers, i.e. the spin-polarized current exerts a spin-transfer-torque on the magnetization in the device. If the current is large enough, the torque leads to precession and finally to a reversal of the magnetization. The critical current I_{c0} to induce spin-transfer reversal at zero temperature in macro-spin approximation for the case of in-plane or perpendicular magnetization of the free layer is given by [87, 88],

$$I_{c0} = \frac{2e}{\hbar}\frac{\alpha}{\eta}\mu_0 M_s V\left(H + H_k + \frac{M_{s\text{eff}}}{2}\right) \quad \text{(in-plane)}$$

$$I_{c0} = \frac{2e}{\hbar}\frac{\alpha}{\eta}\mu_0 M_s V\left(H + H_k\right) \quad \text{(perpendicular)} \tag{5.1}$$

where H_k is the effective anisotropy field. M_s and V are the magnetization and volume of the free layer respectively, α is the damping constant, η is the spin transfer efficiency which may be a function of the current polarity. The expression for the in-plane critical current contains an additional term (M_{seff}/2) which arises from the additional damping caused by the faster precession caused by the demagnetization field.$M_{\text{seff}}$is the saturation magnetization as modified by any anisotropy perpendicular to the plane of the film.The above expression shows that high spin-transfer efficiency, low intrinsic damping, as well as the precise control of any out-of-plane anisotropy used to reduce effect of the demagnetization field are necessary to achieve the desired low critical current.

6.2 Symmetry Filteringeffect

Proposed by Jullière, the Jullière model for TMR[36] has been used widely, especially for magnetic tunnel junctions with Aluminum Oxide barriers[89, 90]. It assumes that the transmission probability is proportional to the product of the density of states (DOS) at the Fermi level,

$$\begin{aligned} I_P &\propto N_L^{\uparrow} N_R^{\uparrow} + N_L^{\downarrow} N_R^{\downarrow} \\ I_{AP} &\propto N_L^{\uparrow} N_R^{\downarrow} + N_L^{\downarrow} N_R^{\uparrow} \end{aligned} \tag{5.2}$$

in which $N_L^{\uparrow}$ and $N_R^{\uparrow}$ are the up spin Fermi level DOS for left and right leads respectively while $N_L^{\downarrow}$ and $N_R^{\downarrow}$ are for the down spin ones. Defining the polarization of the Fermi level DOS for each lead as,

$$P_L = \frac{N_L^{\uparrow} - N_L^{\downarrow}}{N_L^{\uparrow} + N_L^{\downarrow}} \qquad P_R = \frac{N_R^{\uparrow} - N_R^{\downarrow}}{N_R^{\uparrow} + N_R^{\downarrow}} \tag{5.3}$$

from which the TMR ratio would be,

$$\text{TMR} = \frac{I_P - I_A}{I_A} = \frac{2P_L P_R}{1 - P_L P_R} \tag{5.4}$$

Although it seems reasonable, the Jullière model cannot explain the experimental results that majority electrons carry most ofthe tunneling current in Co and Ni systems where it is already known that there a much larger minority DOS than majority DOS[91]. Moreover, the assumption that only the material of the leads matters did not provide an plausible answer for the observed TMR change due to the change of barrier materials[92].

For the tunneling of free electrons through a simple barrier, Slonczewski[93]showed that the Jullière model can be corrected by introducing the effective polarization defined by

$$P_{eff} = P\frac{\kappa_0^2 - k^{\uparrow}k^{\downarrow}}{\kappa_0^2 + k^{\uparrow}k^{\downarrow}} \tag{5.5}$$

where $\kappa_0^2 = \sqrt{\left(\frac{2m}{\hbar}\right)^2 \left(V_B - E_F\right)}$ describes the decay rate of the wavefunction for $k_{\|} = 0$ in the barrier region.

Quantum tunneling through an insulating barrier is enabled by evanescent states.The evanescent states, i.e.the Bloch states associated with complex wave vectors $\vec{k}$, arethe exponentially decaying (or growing) solutions toSchrödinger's equation which are unphysical for infinite systems[94].

The decay rate of an evanescent state depends on its symmetry. For the transition metal systems in period 4 and 5 that we are usually interested in wave functions that can be decomposed according to their orbital symmetry, i.e. *s (l=0), p (l=1)* and *d (l=2)*. For electrons traveling in the (001) direction in a system with cubic symmetry, the two dimensional symmetry of the planes perpendicular to the direction of propagation is that of a square. Wave functions propagating in this direction can be classified according to their symmetry in this two dimensional square lattice. The most symmetric wave functions have Δ_1 symmetry. Through *l=2*, the spherical harmonics consistent with this symmetry are those with azimuthal quantum number, m=0. That is, those proportional to *1, z,*and $3z^2$-r^2. We take *z* to be the direction of propagation so that all of these functions are invariant in the *x*-*y* plane. The next most symmetric state is called Δ_5 and is comprised of spherical harmonics with *m=+1* and *-1*, through *l=2,* these are*x, y, xz* and *yz*. These states are doubly degenerate since the state comprised of *x* and

*xz*spherical harmonics is degenerate with the state comprised of *y* and *yz*.; Δ_2 and Δ_2' states are comprised of *m=2* spherical harmonics, x^2-y^2 and *xy* respectively.

For many simple insulators, the states with Δ_1 symmetry decay more slowly than bands with higher symmetry. One reason for this is that the kinetic energy associated with a wave function, $|\psi\rangle$ is proportional to $-\langle\psi|\nabla^2|\psi\rangle = -\langle\psi|\partial_x^2+\partial_y^2+\partial_z^2|\psi\rangle$. Any curvature of the wave functions in the *x*-*y* plane requires kinetic energy that cannot be used for propagation in the *z* direction through the barrier.

The BC at the interface between lead and barrier requires the bands in the lead to matchwith the evanescent states according to their symmetry. Therefore barrier materials such as (001) oriented MgO can act as symmetry filters that pass wave functions with Δ_1 symmetry with much higher probability thanwavefunctions with lower symmetry.

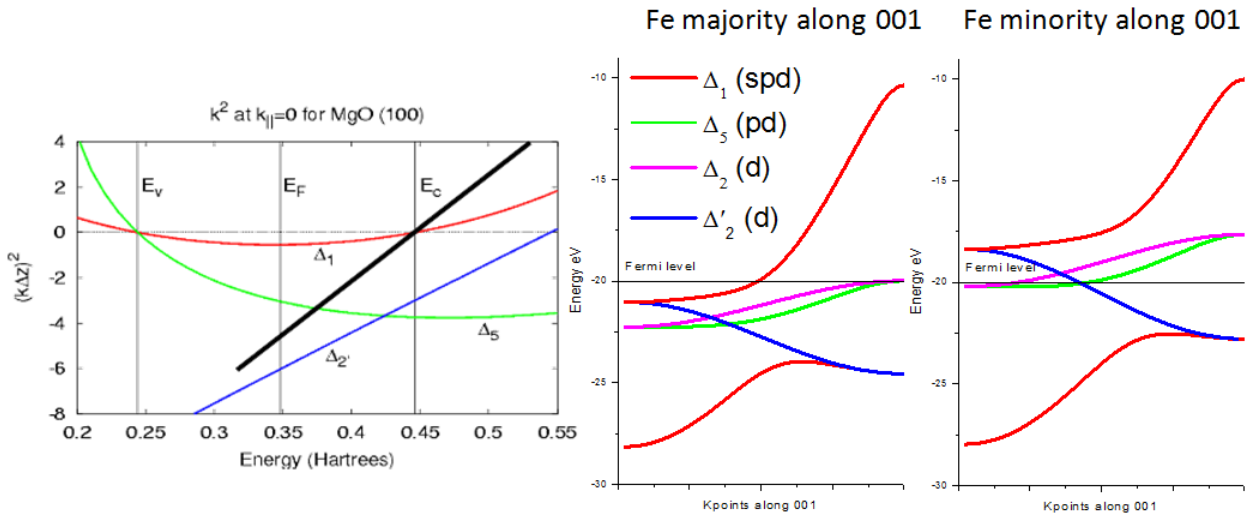

Figure 6.1.*Left*. complex bands of MgO (Butler 2008[95]). *Center* and *right*: bands of Fe along 001 direction. In MgO, the same Δ_1 state that forms the conduction band also forms one of the valence bands and is evanescent in the band gap region between the top of the valence band and the bottom of the conduction band.

For the compatible lead material to the MgO symmetry filter, we search for a material that has propagating Δ_1 states in one spin channel but not the other. According to the band structure of Fe shown above, we can see that the Fermi level crosses a Δ_1 band in the majority spin channel but not in the minority channel, which means Fe can serve as a compatible lead material with MgO as the symmetry filter. This explains why the Fe/MgO/Fe junction would yield such a high TMR ratio [39, 43, 95-97].

6.3 MnAl as a candidate electrode

As mentioned in Section5.3, MnAl has a single ferromagnetic phase called the τ phase. The τ phase has the tetragonal $L1_0$ structure and a relatively large magnetic anisotropy with easy axis parallel to the c-axis of the tetragonal cell. The relaxed structure of $L1_0$ MnAl given by ab initio studies has a lattice constant, a=3.91Å, while the basis vectors of the two atom (1 Mn-1Al) cell are $\begin{Bmatrix} 0.5a & 0.5a & 0 \\ -0.5a & 0.5a & 0 \\ 0 & 0 & 0.88a \end{Bmatrix}$. The magnetization is $2.30\mu_{Bohr}$ per unit cell and the calculated out-of-plane magneto crystallineanisotropy of 1.65×10^6 Joule/m^3 . The calculated Gilbert damping constant is 0.0027, which is relatively small.

The band structureof τ-phase MnAl indicates that it is a candidate for the electrode material in a symmetry-based spin filter TMR sandwich. The band structure along the (001) direction (Figure 6.2) shows that the Fermi level crosses a Δ_1 band in the majority spin channel but not in the minority channel. In fact, there are no states at the Fermi level in this direction for the minority channel. The local DOS calculation shows that the wave functions of only one statenear the Fermi level penetrate significantly into the MgO layer (see bottom left figure in Figure 6.2).

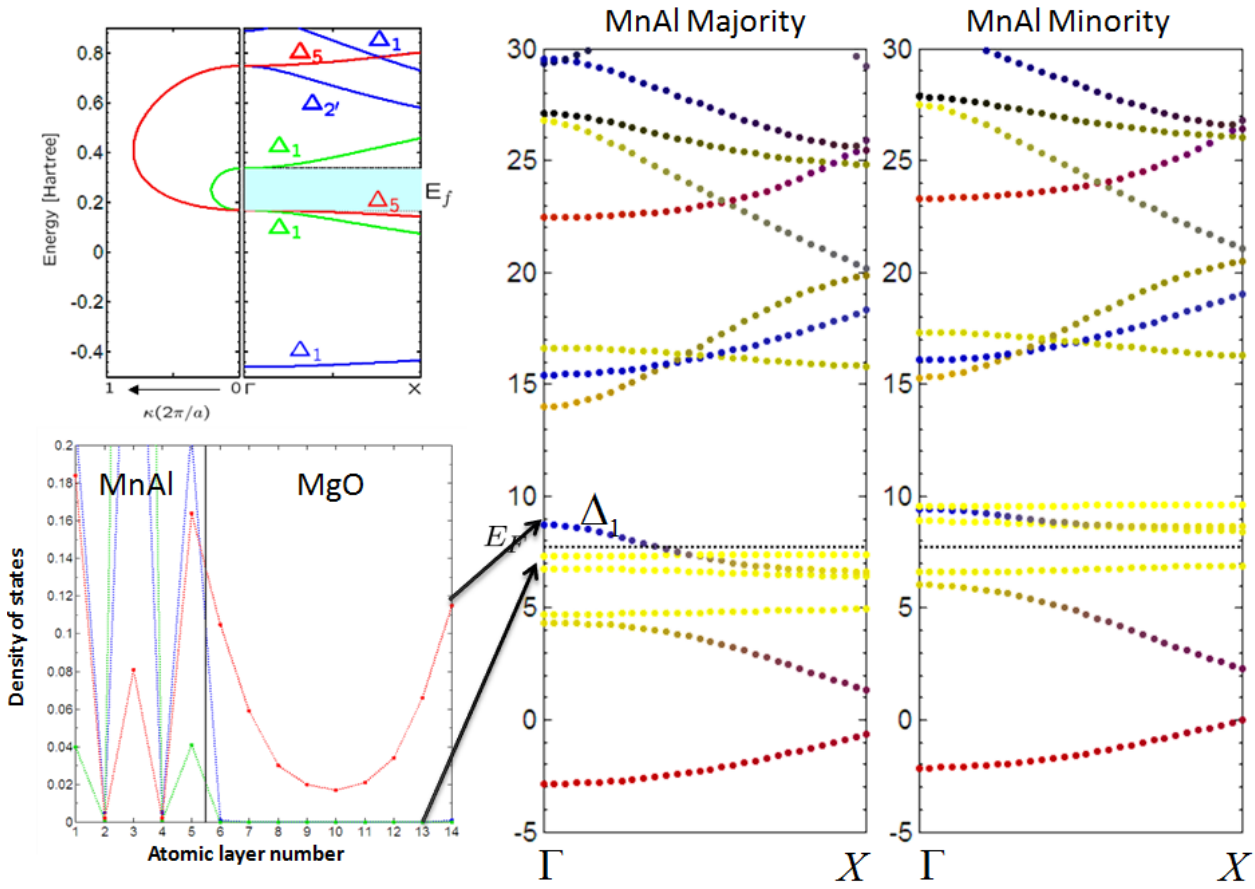

Figure 6.2.*Top left:* Complex band structure of MgO on top of MnAl. *Bottom left:* local Density of States in the majority channel of the MnAl-MgO junction. *Right:* Majority and minority banddiagram for MnAl of $L1_0$ structure along 001 direction. The Fermi level crosses a Δ_1 band in the majority spin channel (the labeled one starts with blue color near the Γ point and turns yellower as goes to the X point) but does not in the minority channel. The color code indicates the composition. Red is s character (RGB code [100]), blue is p character (RGB code [001]), and yellow is d character (RGB code[110]).

6.3.1 The strain's effect on MnAl

Although the electronic structure of MnAl in its equilibrium structure meets the requirements for a symmetry-based spin-filter electrode, the material poses challenges for spintrinics applications. For example, the high coercivity of τ phase MnAl creates difficulties

for most sensor applications. In addition, if it is not fully ordered, first-principles calculations predict that anti-site Mn atoms would have a large moment opposite to those on the correct sites. The in-plane lattice constant of MnAl is significantly smaller than that of MgO, 3.91 vs. 4.21Å causing an epitaxial structure to be strained by more than 7%. To study the strain effect, we did a series of first-princplescalculations for $L1_0$ MnAl with different lattice constants. For each lattice constant we calculated the energy as a function of and c/a ratio. Based on the minimum energy we estimate that the c/a ratio should be 0.961 for $a = 3.8$ Å; 0.912 for $a = 3.9$ Å; 0.847 for $a = 4.0$ Å; 0.752 for $a = 4.1$ Å and 0.685 for $a = 4.2$ Å. The results are shown in Table 8.

When we recalculated the bands using these new parameters we found that the Δ_1 band near Fermi level that we are interested in is sensitive to strain. For a lattice constant of 3.8Å, the Fermi level just barely touches this band. As the lattice constant increases, the Δ_1 band descends and therefore is crossed by the Fermi level in the majority channel. However the corresponding Δ_1 band in the minority channel also descends. When the lattice constant reaches 4.1Å, the Fermi level would cross the Δ_1 band in both channels and therefore complicates the symmetry filtering effect in the MnAl-MgO spin filter since there would be propagating states in both channels. If the lattice constant keeps going up to 4.2Å, the spin filter effect would be recovered with the Fermi level would crossing the Δ_1 band in the minority channel but not the majority channel. Therefore we can conclude that the strain plays an important role and the lattice constant is crucial. The MnAl-MgO spin filter does not work when the lattice constant is around 4.1Å. Since the relaxed lattice constant for τ phase MnAl is 3.91Å and for MgO is 4.21Å. The spin filter "dead zone" just falls in-between. This may increase the difficulties in the fabrication.

It should also be expected that the magnetic anisotropy will be a sensitive function of strain, for example, when the c/a ratio is equal to $1/\sqrt{2}$, the structure is cubic B2 which and would not have uniaxial anisotropy. There may still, however, be strong interfacial anisotropy.

Table 8. Total energy and magnetization of $L1_0$ MnAl with different lattice constants

		c/a ratio						
	a (Å)	0.5	0.6	0.7	0.8	0.9	1	1.1
E (eV)	3.8	-	-	-11.86	-12.77	-13.11	-13.10	-12.85
	3.9	-	-	-12.48	-13.03	-13.16	-13.01	-12.67
	4	-	-	-12.86	-13.12	-13.08	-12.82	-12.42
	4.1	-	-	-13.05	-13.09	-12.91	-12.58	-12.15
	4.2	-10.27	-12.68	-13.08	-12.96	-12.68	-12.31	-11.87
M (μ_{Bohr})	3.8	-	-	1.65	1.76	2.22	2.46	2.75
	3.9	-	-	1.73	1.95	2.33	2.63	2.92
	4	-	-	1.79	2.15	2.46	2.80	3.11
	4.1	-	-	1.85	2.29	2.61	3.02	3.45
	4.2	0.00	1.70	1.90	2.43	3.00	3.39	3.66

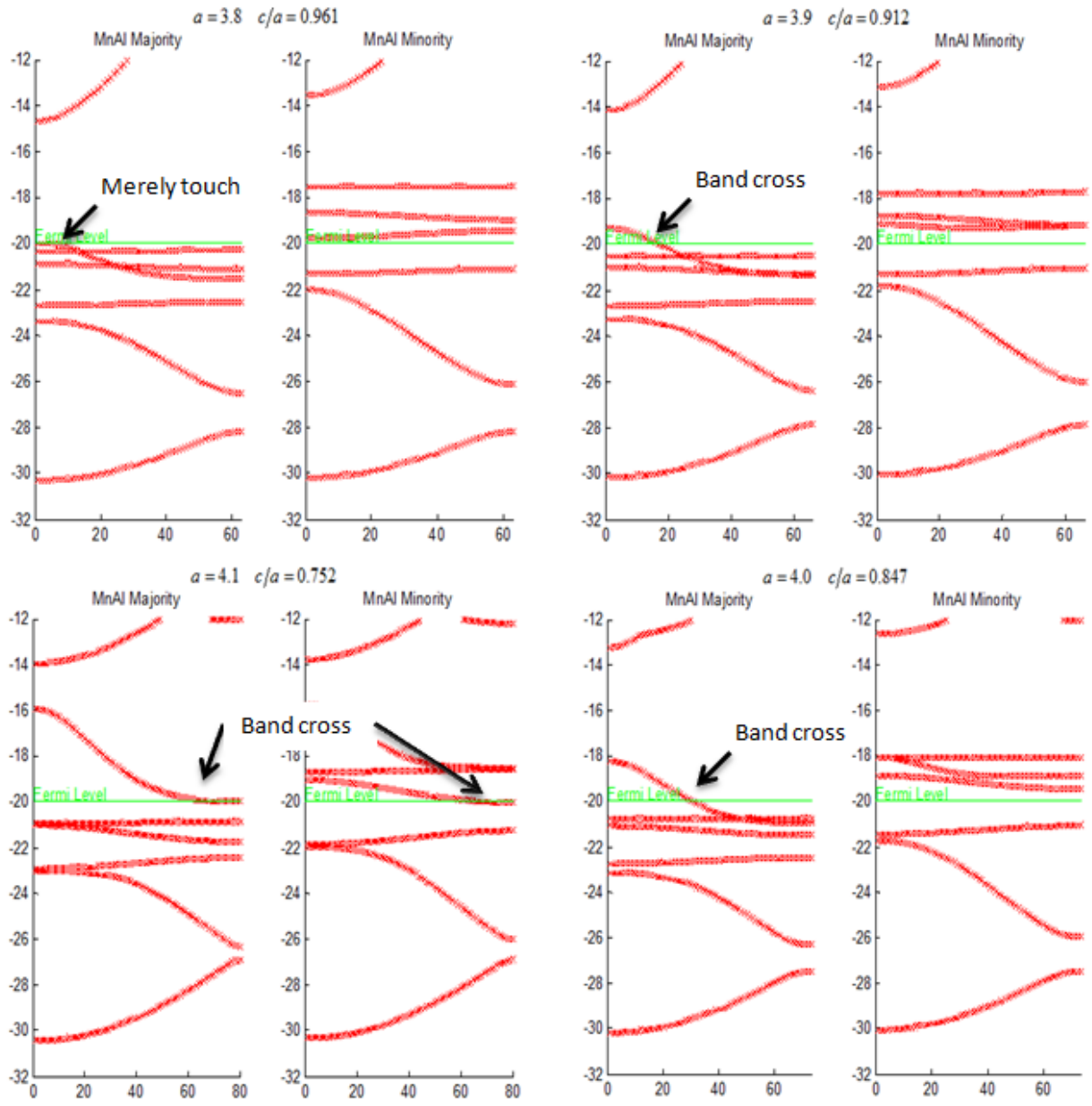

Figure 6.3. Band structure for MnAl of $L1_0$ structure along 001 direction, from *top left* , in *clockwise* are bands for a=3.8, 3.9, 4.0, 4.1Å respectively.

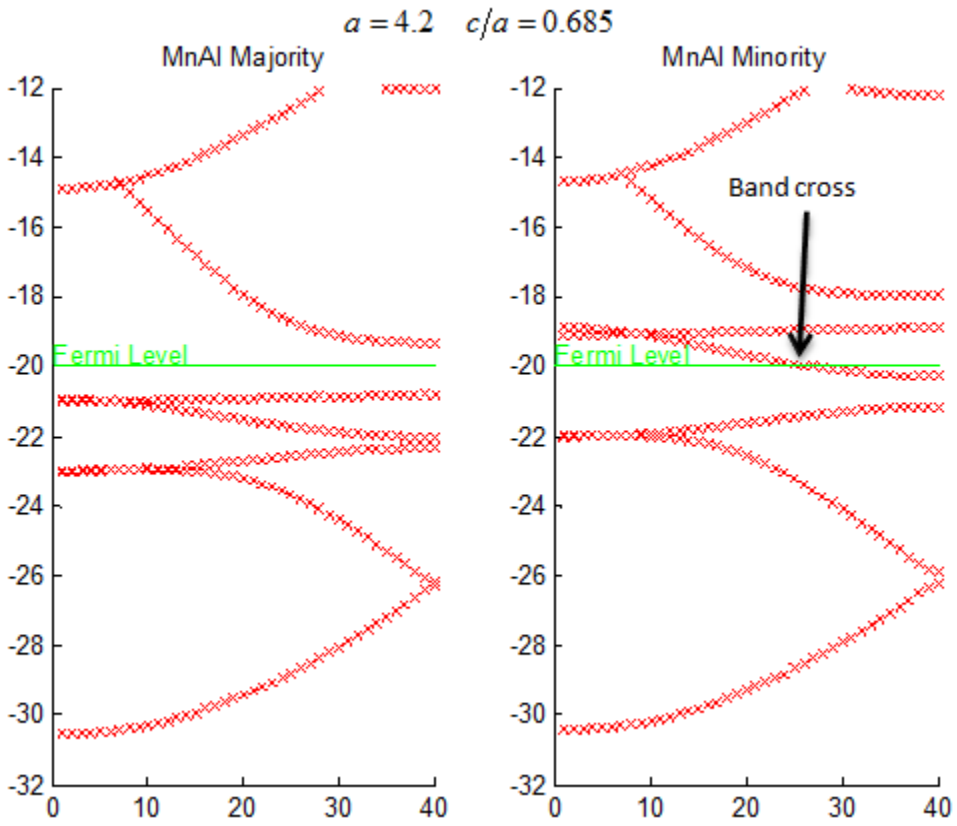

Figure 6.4.Band structure for MnAl of $L1_0$ structure along 001 direction with a=4.2Å

In conclusion, τ phase MnAl is a material that has potential for serving as the lead material in MTJs because it has low damping, perpendicular anisotropy as well as the properties of spin filtering effect though the actual fabrication requires delicate control of strain as wells as phase transition.

References

1. G. E. Moore, Proceedings of the IEEE **86** (1), 82-85 (1998).

2. C. Walter, Scientific American **293** (2), 32-33 (2005).

3. J. Åkerman, Science **308** (5721), 508-510 (2005).

4. W. Thomson, *On the Electro-Dynamic Qualities of Metals:--Effects of Magnetization on the Electric Conductivity of Nickel and of Iron*. (The Royal Society, 1856).

5. G. Binasch, P. Grünberg, F. Saurenbach and W. Zinn, Physical Review B **39** (7), 4828 (1989).

6. M. N. Baibich, J. M. Broto, A. Fert, F. N. Van Dau, F. Petroff, P. Etienne, G. Creuzet, A. Friederich and J. Chazelas, Physical Review Letters **61** (21), 2472 (1988).

7. W. P. Pratt, Jr., S. F. Lee, J. M. Slaughter, R. Loloee, P. A. Schroeder and J. Bass, Physical Review Letters **66** (23), 3060-3063 (1991).

8. S. F. Lee, W. P. Pratt, Jr., R. Loloee, P. A. Schroeder and J. Bass, Physical Review B **46** (1), 548 (1992).

9. R. E. Camley and J. Barnaś, Physical Review Letters **63** (6), 664 (1989).

10. P. M. Levy, S. Zhang and A. Fert, Physical Review Letters **65** (13), 1643 (1990).

11. S. F. Lee, W. P. Pratt Jr, Q. Yang, P. Holody, R. Loloee, P. A. Schroeder and J. Bass, Journal of Magnetism and Magnetic Materials **118** (1-2), L1-L5 (1993).

12. N. F. Mott, Proc. R. Soc. Lond. A **153** (1936).

13. J. Barnaś, O. Baksalary and A. Fert, Physical Review B **56** (10), 6079 (1997).

14. J. Chen, J. Appl. Phys. **85** (8), 4551 (1999).

15. M. D. Stiles and D. R. Penn, Physical Review B **61** (5), 3200 (2000).

16. J. Barnaś and A. Fert, Journal of Magnetism and Magnetic Materials **136** (3), 260-268 (1994).

17. A. Gonis and W. H. Butler, *Multiple Scattering in Solids*. (Springer, 2000).

18. M. Johnson, Physical Review Letters **67** (25), 3594 (1991).

19. Q. Yang, P. Holody, S. F. Lee, L. L. Henry, R. Loloee, P. A. Schroeder, W. P. Pratt, Jr. and J. Bass, Physical Review Letters **72** (20), 3274 (1994).

20. T. Valet and A. Fert, Physical Review B **48** (10), 7099 (1993).

21. COMSOL Model Gallery, Dialysis 2011, http://www.comsol.com/showroom/gallery/258/

22. R. A. de Groot, F. M. Mueller, P. G. v. Engen and K. H. J. Buschow, Physical Review Letters **50** (25), 2024 (1983).

23. C. Felser, Gerhard H. Fecher and B. Balke, Angewandte Chemie International Edition **46** (5), 668-699 (2007).

24. R. A. de Groot, F. M. Mueller, P. G. v. Engen and K. H. J. Buschow, Physical Review Letters **50** (Copyright (C) 2010 The American Physical Society), 2024 (1983).

25. K. Schwarz, Journal of Physics F: Metal Physics **16** (9), L211 (1986).

26. I. Galanakis and et al., Journal of Physics D: Applied Physics **39** (5), 765 (2006).

27. I. Galanakis and P. Mavropoulos, Journal of Physics: Condensed Matter **19** (31), 315213 (2007).

28. S. Wurmehl, Appl. Phys. Lett. **88** (3), 032503 (2006).

29. F.Bloch, Zeitschrift fur Physik **52** (jul), 555-600 (1929).

30. J. C. Slater and G. F. Koster, Physical Review **94** (6), 1498 (1954).

31. J. Cerdá and F. Soria, Physical Review B **61** (12), 7965-7971 (2000).

32. R. Mulliken, J. Chem. Phys. **17** (12), 1248 (1949).

33. K. E. H. M. Hanssen and P. E. Mijnarends, Physical Review B **34** (8), 5009-5016 (1986).

34. K. E. H. M. Hanssen, P. E. Mijnarends, L. P. L. M. Rabou and K. H. J. Buschow, Physical Review B **42** (3), 1533-1540 (1990).

35. W. H. Butler, C. K. A. Mewes, C. Liu and T. Xu, *Rational Design of Half-Metallic Heterostructures (arXiv:1103.3855v1 [cond-mat.mtrl-sci]),* Unpublished Work,

36. M. Julliere, Physics Letters A **54** (3), 225-226 (1975).

37. T. Miyazaki, Journal of Magnetism and Magnetic Materials **139** (3), L231-L234 (1995).

38. J. S. Moodera, L. R. Kinder, T. M. Wong and R. Meservey, Physical Review Letters **74** (16), 3273-3276 (1995).

39. W. H. Butler, X. G. Zhang, T. C. Schulthess and J. M. MacLaren, Physical Review B **63** (5), 054416 (2001).

40. M. Bowen, V. Cros, F. Petroff, A. Fert, C. M. Boubeta, J. L. Costa-Krämer, J. V. Anguita, A. Cebollada, F. Briones, J. M. d. Teresa, L. Morellón, M. R. Ibarra, F. Güell, F. Peiró and A. Cornet, **79** (11), 1655-1657 (2001).

41. S. Yuasa, T. Nagahama, A. Fukushima, Y. Suzuki and K. Ando, Nat Mater **3** (12), 868-871 (2004).

42. S. Ikeda, J. Hayakawa, Y. Ashizawa, Y. M. Lee, K. Miura, H. Hasegawa, M. Tsunoda, F. Matsukura and H. Ohno, **93** (8), 082508 (2008).

43. X. G. Zhang and W. H. Butler, Physical Review B **70** (17), 172407 (2004).

44. R. Landauer, Philosophical Magazine **21** (172), 863-867 (1970).

45. R. Landauer, IBM Journal of Research and Development **1** (3), 9 (1957).

46. M. Büttiker, Physical Review Letters **57** (14), 1761-1764 (1986).

47. V. I. Puller and Y. Meir, Physical Review Letters **104** (25), 256801 (2010).

48. M. L. Polianski and M. Büttiker, Physical Review Letters **96** (15), 156804 (2006).

49. S. Heusler, S. Müller, P. Braun and F. Haake, Physical Review Letters **96** (6), 066804 (2006).

50. R. Landauer, Physica Scripta **1992** (T42), 110 (1992).

51. R. Landauer, Journal of Physics: Condensed Matter **1** (43), 8099 (1989).

52. R. Landauer, IBM Journal of Research and Development **32** (3), 306-316 (1988).

53. M. Büttiker, IBM J. Res. Dev. **32** (317) (1988).

54. S. Datta, *Electronic transport in mesoscopic systems*. (Cambridge University Press, 1997).

55. I. Snyman and C. W. J. Beenakker, Physical Review B **75** (4), 045322 (2007).

56. Y. Meir, N. S. Wingreen and P. A. Lee, Physical Review Letters **66** (23), 3048-3051 (1991).

57. D. H. Lee and J. D. Joannopoulos, Physical Review B **23** (10), 4988-4996 (1981).

58. F. Guinea, C. Tejedor, F. Flores and E. Louis, Physical Review B **28** (8), 4397-4402 (1983).

59. M. P. L. Sancho, J. M. L. Sancho, J. M. L. Sancho and J. Rubio, Journal of Physics F: Metal Physics **15** (4), 851 (1985).

60. K. W. McVoy, L. Heller and M. Bolsterli, Reviews of Modern Physics **39** (1), 245-258 (1967).

61. H. J. Monkhorst and J. D. Pack, Physical Review B **13** (Copyright (C) 2010 The American Physical Society), 5188 (1976).

62. J. D. Pack and H. J. Monkhorst, Physical Review B **16** (4), 1748 (1977).

63. M. Marsman, Automatic k-mesh generation 2011,11-03 http://cms.mpi.univie.ac.at/vasp/vasp/Automatic_k_mesh_generation.html

64. L. Landau and E. Lifshitz, Phys. Zeitsch. der Sow **8**, 153 (1935).

65. S. Lida, Journal of Physics and Chemistry of Solids **24** (5), 625-630 (1963).

66. T. L. Gilbert, Physical Review **100** (1243) (1955).

67. T. L. Gilbert, Magnetics, IEEE Transactions on **40** (6), 3443-3449 (2004).

68. T. L. Gilbert and J. M. Kelly, in *Conference on magnetism and magnetic materials* (American Institute of Electrical Engineers, Pittsburgh, PA, 1955), pp. 253.

69. B. Heinrich, R. Urban and G. Woltersdorf, *Magnetic relaxation in metallic films: Single and multilayer structures*. (AIP, 2002).

70. B. Heinrich, R. Urban and G. Woltersdorf, Magnetics, IEEE Transactions on **38** (5), 2496-2501 (2002).

71. J. A. C. Bland and B. Heinrich, *Ultrathin Magnetic Structures III: Fundamentals of Nanomagnetism*. (Springer, 2010).

72. H. Suhl, Magnetics, IEEE Transactions on **34** (4), 1834-1838 (1998).

73. T. Kobayashi, R. C. Barker and A. Yelon, Physical Review B **7** (7), 3286-3297 (1973).

74. W. S. Ament and G. T. Rado, Physical Review **97** (6), 1558-1566 (1955).

75. Z. Frait and H. MacFaden, Physical Review **139** (4A), A1173-A1181 (1965).

76. V. Kamberský, Czechoslovak Journal of Physics **26** (12), 1366-1383 (1976).

77. V. Kamberský, Canadian Journal of Physics **48** (24), 2906-2911 (1970).

78. V. Kamberský, Physical Review B **76** (13), 134416 (2007).

79. C. Liu, C. K. A. Mewes, M. Chshiev, T. Mewes and W. H. Butler, Applied Physics Letters **95** (2), 022509-022503 (2009).

80. M. D. Jaffe and J. Singh, Solid State Communications **62** (6), 399-402 (1987).

81. C. Liu, *Theoretical investigation of the intrinsic Gilbert damping parameter using first-principles and tight-binding models*, THE UNIVERSITY OF ALABAMA, 2009.

82. T. B. Massalski, H. Okamoto and A. S. M. International, *Binary alloy phase diagrams*. (ASM International, Materials Park, Ohio, 1990).

83. H. Okamoto, Journal of Phase Equilibria **18** (4), 398-399 (1997).

84. M. Oishi, *Spin Injection MRAM Main Focus at MMM*, Tech On!, Feb 26, 2008, Nikkei Electronics Asia.

85. J. C. Slonczewski, Journal of Magnetism and Magnetic Materials **159** (1-2), L1-L7 (1996).

86. L. Berger, Physical Review B **54** (13), 9353-9358 (1996).

87. J. A. Katine and E. E. Fullerton, Journal of Magnetism and Magnetic Materials **320** (7), 1217-1226 (2008).

88. R. H. Koch, J. A. Katine and J. Z. Sun, Physical Review Letters **92** (8), 088302 (2004).

89. D. J. Monsma and S. S. P. Parkin, Applied Physics Letters **77** (5), 720-722 (2000).

90. Y. H. Huang, J. H. Hsu and J. W. Chen, Magnetics, IEEE Transactions on **33** (5), 3556-3558 (1997).

91. P. M. Tedrow and R. Meservey, Physical Review B **7** (1), 318-326 (1973).

92. J. M. De Teresa, A. Barthélémy, A. Fert, J. P. Contour, R. Lyonnet, F. Montaigne, P. Seneor and A. Vaurès, Physical Review Letters **82** (21), 4288-4291 (1999).

93. J. C. Slonczewski, Physical Review B **39** (10), 6995-7002 (1989).

94. C. Cohen-Tannoudji, B. Diu and F. Laloë, *Quantum mechanics*. (Wiley, 1977).

95. W. H. Butler, Science and Technology of Advanced Materials **9** (1), 014106 (2008).

96. W. H. Butler, X. G. Zhang, T. C. Schulthess and J. M. MacLaren, Physical Review B **63** (9), 092402 (2001).

97. X. G. Zhang and W. H. Butler, Journal of Physics: Condensed Matter **15** (41), R1603 (2003).